Metastability of Magnetic Nanoparticles in Magnetization Relaxation with Different Dynamics and Distributions of Magnetic Anisotropy

Yoh Yamamoto

Dissertation submitted to the Faculty of the
Virginia Polytechnic Institute and State University
in partial fulfillment of the requirements for the degree of

Doctor of Philosophy
in
Physics

Kyungwha Park, Chair
Jean J. Heremans
Michel J. Pleimling
Uwe C. Täuber

May 7, 2013
Blacksburg, Virginia

Keywords: Magnetic Anisotropy, Magnetization Relaxation, Blume-Capel Model, Magnetic Nanoparticle, Phonon-Assisted Transition Rate

Metastability of Magnetic Nanoparticles in Magnetization Relaxation with Different Dynamics and Distributions of Magnetic Anisotropy

Yoh Yamamoto

(ABSTRACT)

We study the metastability of magnetic nanoparticles with size distributions. We simulate an array of magnetic nanoparticles with a spin $S = 1$ ferromagnetic Blume-Capel model on a square lattice. Studying decays of the metastable state in the Blume-Capel model at low temperatures requires an extremely long computational time in kinetic Monte Carlo simulations. Therefore, we use an advanced algorithm adapted from the Monte Carlo with absorbing Markov chain algorithm for the Ising model in order to study the Blume-Capel model with size distributions. We modeled the particle size distributions as distributions of magnetic anisotropy. We compute the low-temperature average lifetime of the magnetization relaxation using kinetic Monte Carlo simulations with the advanced algorithms. We also calculate the lifetime using the absorbing Markov chains method for analytical results. Our results show that the lifetime of the metastable state follows a modified-Arrhenius law where the energy barrier has a dependency on temperature and standard deviation of the distributions in addition to magnetic field and magnetic anisotropy. The magnetic anisotropy barrier is determined by the smallest particle within a given distribution. We also study magnetization relaxation in different single critical droplet regions using different dynamics: Glauber and phonon-assisted dynamics. We find that the lifetime follows the modified-Arrhenius law for both dynamics, and an explicit form of the lifetime differs in different regions for different dynamics. For the Glauber dynamics, the Arrhenius prefactor does not depend on the standard deviation of the distribution of the magnetic anisotropy. For the phonon-assisted dynamics, however, even the prefactor of the lifetime depends on the standard deviation and is significantly reduced for a wide distribution of magnetic anisotropy. Furthermore, the phonon-assisted dynamics forbids transitions between degenerate energy states and results in an increase of the energy barrier at the single critical droplet region boundary compared to

that for the Glauber dynamics. We find that the spin system with a distribution of magnetic anisotropy finds lower-energy relaxation pathways to avoid degenerate state, and the energy barrier becomes the same for both dynamics.

Acknowledgments

During the time I spent at Virginia Tech, I have received support and encouragement from many people. I would like to thank my advisor, Professor Kyungwha Park, for her extreme patience and faith in me. Her guidance made me through my graduate studies. I would like to thank my dissertation committee of Professor Jean Heremans, Professor Michel Pleimling, and Professor Uwe Täuber for their patience, encouragement, and valuable discussions. I am thankful to Per Arne Rikvold for discussions about my dissertation research. I would like to thank my fellow doctoral students for their support and friendship. I would also like to thank my friends, especially Erin Cleary, Tom Gordon, and Matt Carlson for their friendship and for correcting my English in various writings. Finally, I am grateful to my parents for being always supportive about my graduate studies.

Contents

List of Figures

List of Tables

Chapter 1

Introduction

Ferromagnetism is characterized by spontaneous magnetization as seen in permanent magnets. For bulk ferromagnetic material, atoms with spin magnetic moments interact dominantly via isotropic exchange interactions which originate from the overlap of the charge distributions, and the exchange interaction energy is a thousand times greater than the magnetic dipole-dipole interaction energy. Ferromagnetic materials have two phases separated by the Curie temperature, T_c. Above T_c, a paramagnetic phase is stable, and the orientations of magnetic moments are disordered. Below T_c ferromagnetic phase is more stable, and magnetic moments align parallel to each other. The orientation to which all of the moments point can be any direction. However, electronic orbital motion can be anisotropically coupled to spin degrees of freedom, and this spin-orbit coupling results in a preferential (crystalline) direction along which magnetic moments align with a smaller energy cost or lower external magnetic field. This orientation is referred to as magnetic easy axis or direction and the energy associated with the spin-orbit coupling is magnetic anisotropy energy.

In bulk ferromagnets (below T_c), the magnetic moments are aligned one another in the same orientation and form magnetic domains. A magnetic domain is a region where magnetic moments inside point in the same direction due to the exchange interactions. The dipole-dipole interaction is normally weak within a domain. A large domain is unstable because of the

magnetostatic energy. When all of moments point in the same direction and form a large domain, it produces magnetic fields outside of the material and has a high magnetostatic energy. Thus, formation of multiple domains reduces a magnetostatic energy. Between adjacent domains there is a region called domain wall, where orientations of moments gradually change from one to another. This gradual change in the direction of magnetization lowers the exchange energy compared to an abrupt change of magnetization between adjacent domains. Coercivity is the applied reverse magnetic field needed to bring the magnetization to zero starting from saturated magnetization, and it measures the resistance to demagnetize a permanent magnet. Magnetic anisotropy and coercivity are related, and magnets with high coercivity are referred to as hard magnets, and those with low coercivity are called soft magnets. When a magnetic particle size becomes smaller than a domain wall, the particle can have a single domain. Magnetic nanoparticles can have single domains.

For bulk ferromagnets, the magnetic moments are separated with atomic distances, and the exchange interaction dominates in this short range. In our simulation of an array of magnetic nanoparticles, the exchange interaction appears as a nearest neighbor interaction. For a collection of magnetic nanoparticles, typically, a magnetic anisotropy energy dominates over an exchange or magnetic dipole-dipole energy. When the distances between magnetic nanoparticles are significantly larger than atomic distances, a magnetic dipole-dipole energy is greater than an exchange energy. Inclusion of the dipole-dipole energy requires consideration of all pairs of magnetic moments in a given array of magnetic nanoparticles. This would be challenging in our simulation of a collection of magnetic nanoparticles with size distribution. Thus, in our simulation, the dipole-dipole energy is neglected, and we consider only the exchange energy and the anisotropy energy.

Single domain magnetic nanoparticles have great commercial and intellectual values and have various applications. The most apparent application is use of magnetic nanoparticles as information storage devices [1, 2, 3]. For data storage applications, magnetic nanoparticles are desirable because of their high coercivity such that data are not easily lost over a time period. Also, nanoparticles are significantly smaller in size for storing binary digits than

magnetic grains found in traditional devices, therefore the physical size of these devices can be dramatically reduced by using magnetic nanoparticles as bits. Magnetic nanoparticles can be also used in electronics for their unique density of states. In addition to usage in high density data storage, soft magnetic nanoparticles have applications in medicine such as in medical diagnostics, drug targeting, and cancer therapies [4] as well as controlled drug delivery. These nanoparticles may be used for magnetic resonant imaging (MRI) enhancement as sensors or contrast agents [5, 6, 7]. One anticipated application is the use of these nanoparticles to transport anticancer drugs to a targeted tumor within the human body [8]. A magnetic field could be used to control the particles. Magnetic responses on injected nanoparticles due to an applied external field requires testing and modeling to be understood comprehensively.

Ideal magnetic nanoparticles have identical particle sizes and shapes. Recent studies show, however, that chemically synthesized nanoparticles are known to have a particle size distribution as well as a shape distribution [9, 10, 11, 12, 13, 14]. It is also found that the distribution of particle size results in a distribution of magnetic anisotropy energy [15]. Because size and shape distributions arise from current nanoparticle synthesis techniques, it is essential to understand how the distribution affects the magnetic properties. The magnetic anisotropy energy or barrier changes with particle size and it equals a magnetic anisotropy parameter multiplied by the square of spin S^2 of a nanoparticle. One method of implementation of the size distribution is to consider a distribution of the magnetic anisotropy parameter with a fixed spin S. We consider the case that the magnetic anisotropy parameter has a Gaussian distribution. This distribution appears as a distribution of magnetic anisotropy barriers and affect coercivity and magnetization relaxation significantly. We study magnetization relaxation at low temperature as a function of magnetic field, magnetic anisotropy, and distribution of magnetic anisotropy barrier. In this study, we use a spin $S = 1$ ferromagnetic Blume-Capel model on a square lattice with periodic boundary conditions at low temperature, using kinetic Monte Carlo (KMC) simulations and the absorbing Markov chains (AMC) method [16, 17]. We are mainly interested in the single-droplet regime where a critical droplet consists of a single droplet of the stable phase. We consider the case where

exchange interactions are significant over dipole-dipole interactions. For magnetic particles with constant magnetic anisotropy, the average lifetime of the magnetization upon reversal of field in the single-droplet regime follows the Arrhenius law:

$$\langle \tau \rangle = A e^{\beta \Gamma} \tag{1.1}$$

where A is a nontrivial prefactor, $\beta = 1/k_B T$ with the Boltzmann constant k_B and temperature T, and Γ is an energy required for nucleation (energy barrier) of the stable phase.

Using the Glauber transition rate, we study the effect of particle size effect and compare three case: (i) a fixed particle size, (ii) uniformly distributed particle sizes, and (iii) normally distributed particle sizes. Our results indicate the inclusion of particle size distribution decreases the lifetime of the metastable state. We quantify the changes in lifetime as a function of a standard deviation or a width of distributions, finding that the lifetime follows the modified Arrhenius law. We also consider the Blume-Capel model weakly coupled to a phonon heat bath, and perform kinetic Monte Carlo simulations, using the derived transition rates from a microscopic spin-phonon coupling Hamiltonian [18]. This transition rate gives a more physically accurate description of a thermal heat bath than the conventionally used transition rates such as Glauber dynamics. Using this transition rate, we study an effect of different transition rates and an effect of different dynamic regions where the size of single critical droplet differs. We also study the boundary between the regions. We find that for both transition rates (dynamics), the energy barrier Γ depends on temperature and standard deviation of the distribution of magnetic anisotropy for a given field and magnetic anisotropy, and that for the phonon-assisted (PA) dynamics, the prefactor A depends on standard deviation of the distribution of magnetic anisotropy as well as field and magnetic anisotropy for a given region. At the region boundary, without distributions of magnetic anisotropy, the energy barrier Γ for the phonon-assisted dynamics is much higher than that for the Glauber dynamics due to forbidden transitions between degenerate states. However, with distributions of magnetic anisotropy, the metastable state or magnetization can relax via low-energy pathways guided by the lowest magnetic anisotropy within the distribution.

Thus, the energy barrier becomes the same for both dynamics at the boundary.

This work is organized as follows. In Chapter 2, we discuss the simulation model. We consider the $S = 1$ Blume-Capel model and perform kinetic Monte Carlo simulations using the Glauber transition rate. In Chapter 3, we present background in metastability that appears in magnetization relaxation. We calculate the lifetime of the metastable state and study nucleation and metastability as a function of the external magnetic field and the magnetic anisotropy parameter. In Chapter 4, we discuss the computational methods. Because the system stays in a metastabe state for a long time at low temperature, the simulation of magnetization relaxation takes a long simulation time. We describe an advanced algorithm for dynamic Monte Carlo simulations for a two-state system, and discuss how to apply it to the spin $S = 1$ Blume-Capel model (three-state system). In Chapter 5, we present an effect of distributions of D on the lifetime of the metastable state, using the Glauber transition rate from our simulation data and analytic calculations. We discuss the average lifetime of the metastable state for a constant value of the magnetic anisotropy parameter and for the distributions of the parameter. In Chapter 6, we discuss differences arising from use of different transition rates. We explore this by applying the Glauber transition rate and the three-dimensional phonon-assisted transition rate to the $S = 1$ Blume-Capel model. We study an effect of different dynamics with a constant anisotropy within the single-droplet regime. Using both kinetic Monte Carlo simulations and AMC method, we obtain the average lifetime in the zero-temperature limit. In Chapter 7, we examine magnetization relaxation across a dynamic region boundary for both Glauber transition rate and phonon-assisted transition rate. In Chapter 8, we discuss a special region where a distribution of D does not affect the energy barrier.

Chapter 2

Model

2.1 Blume-Capel model

The model we use is a special case of Blume-Emery-Griffith (BEG) model [19] and was introduced by Blume and Capel in different contexts. Blume proposed a model to explain the first-order magnetic phase transition in UO_2 [20]. Capel also studied magnetic phase transitions using Ising systems with triplet ions ($S = 1$) [21]. The model became known as the Blume-Capel model. We consider the following spin $S = 1$ Blume-Capel model which is adapted from Refs. [20, 21] on a square lattice with periodic boundary conditions. A spin Hamiltonian is given as

$$\mathcal{H} = -2J \sum_{\langle i,j \rangle} S_{iz} S_{jz} - H \sum_i S_{iz} - D \sum_i S_{iz}^2, \tag{2.1}$$

where S_{iz} is the z component of spin at a site i and the magnetic easy axis is along the z axis. If the eigenvalue of S_{iz} is denoted as M_{iz}, there are three possible values of M_{iz}, $+1$, 0, and -1, for a quantum spin $S = 1$ (in the case of $\hbar = 1$). We assume that a classical spin is assigned at each site with three possible states of $M_{iz} = +1, 0$, and -1. The first term of Eq. (2.1) represents exchange interactions between nearest-neighboring spins at sites i and j with an exchange coupling constant J (> 0). We set $J = 1$ such that H and D have units

of J. All spins are counted only once in the summation over nearest neighbors. The second term corresponds to the Zeeman energy with a magnetic field H. The last term indicates a magnetic anisotropy energy with a uniaxial magnetic anisotropy parameter D (> 0). Here DS^2 equals a magnetic anisotropy barrier that is an energy cost to reverse a spin orientation in zero magnetic field, which originates from spin-orbit coupling. Since the magnetic easy axis is aligned along the z axis, the sites with $M_z = \pm 1$ have lower magnetic anisotropy energies than the sites with $M_z = 0$. We choose a spin $S = 1$ in the Blume-Capel model because this is the simplest case in which the magnetic anisotropy, or the third term, plays a nontrivial role. (For the Ising model, the third term does not contribute to the total energy.)

Figure 2.1 shows the ground state phase diagram for the $S = 1$ Blume-Capel model at zero-temperature (modified from Ref. [22]). There are three phases where the ground state spin configuration differs: all spins having $M_z = +1$ for $H > 0$ and $H > -D - 4$, $M_z = -1$ for $H < 0$ and $H < D + 4$, and $M_z = 0$ for $H < -D - 4$ and $H > D + 4$. Two different phases coexist on the phrase boundaries, and a tricritical point can be found at the intersection of the three boundary lines. The critical temperature for the Blume-Capel model changes with D: $T_c = 1.6950J/k_B$ for $H = 0$ and $D = 0$ and $T_c = 2.1855J/k_B$ for $H = 0$ and $D = 5J$ [23]. Note that the Hamiltonian we used has an exchange interaction twice as large as the Hamiltonian in Ref. [23].

In the case of size distributions, larger particles may have higher magnetic anisotropy barriers than smaller particles. The size distribution in a collection of magnetic nanoparticles may also induce a shape distribution. Both size and shape distributions lead to a distribution of magnetic anisotropy barrier. Thus, for simplicity, we model the size distribution as a distribution of magnetic anisotropy parameter for a given spin or magnetic moment; i.e. larger particles having larger magnetic anisotropy parameters D with a fixed spin or magnetic moment per particle (Fig. 2.2(a)). The size distribution can be also modeled as a distribution of spin for a fixed magnetic anisotropy parameter; i.e. larger particles having larger magnetic moments with the parameter D fixed (Fig. 2.2(b)). When distributions of particle sizes are implemented as distributions of D, the third term of Eq. (2.1) is replaced by $-\sum_i D_i S_{iz}^2$,

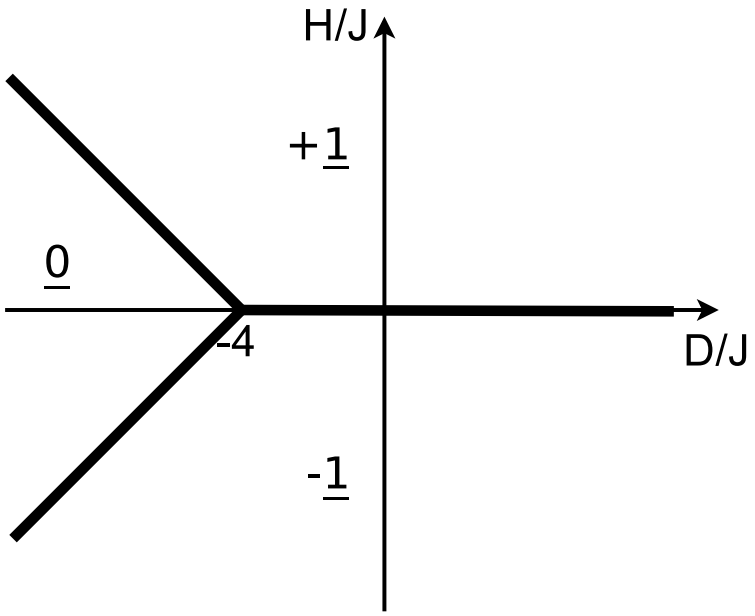

Figure 2.1: The phase diagram for the $S = 1$ Blume-Capel model. There are three phases. $\underline{0}$ ($\pm\,\underline{1}$) denotes that all spins have $m_z = 0$ (± 1) in the ground state. On the phase boundaries, two different phases coexist, and a tricritical point is at the intersection of the three boundary lines. Modified from Ref. [22].

where D_i is selected from distributions of D, in other words, different values of D are assigned to different sites.

2.2 Transition Rates

To study dynamic properties of an array of quantum dots, magnetic nanoparticles, or single-molecule magnets, interactions between such a system and its surrounding need to be considered. A heat bath is typically used and has a much shorter relaxation time than the system. A phonon bath was considered to study magnetization relaxation of arrays of magnetic nanoparticles and single-molecule magnets [18]. It is important to use an appropriate transition rate since it represents a surrounding of the system. We briefly discuss three different transition rates. In this study we use two different transition rates: Glauber and phonon-assisted transition rates (Sec. 2.2.2, 2.2.3).

2.2.1 Metropolis Transition Rate

The Metropolis transition rate is a widely used dynamics in a Monte Carlo method [24]. A transition rate and a transition probability are related with an arbitrary factor τ_s (dimension of time) which is taken as $\tau_s = 1$. The Metropolis transition probability is defined as follows

$$p = \begin{cases} 1, & \text{if } \Delta E < 0 \\ e^{-\beta \Delta E}, & \text{if } \Delta E > 0 \end{cases} \tag{2.2}$$

where $\Delta E = E_{new} - E_{old}$. Here E_{old} (E_{new}) denotes an energy of the spin system before (after) a single spin flip.

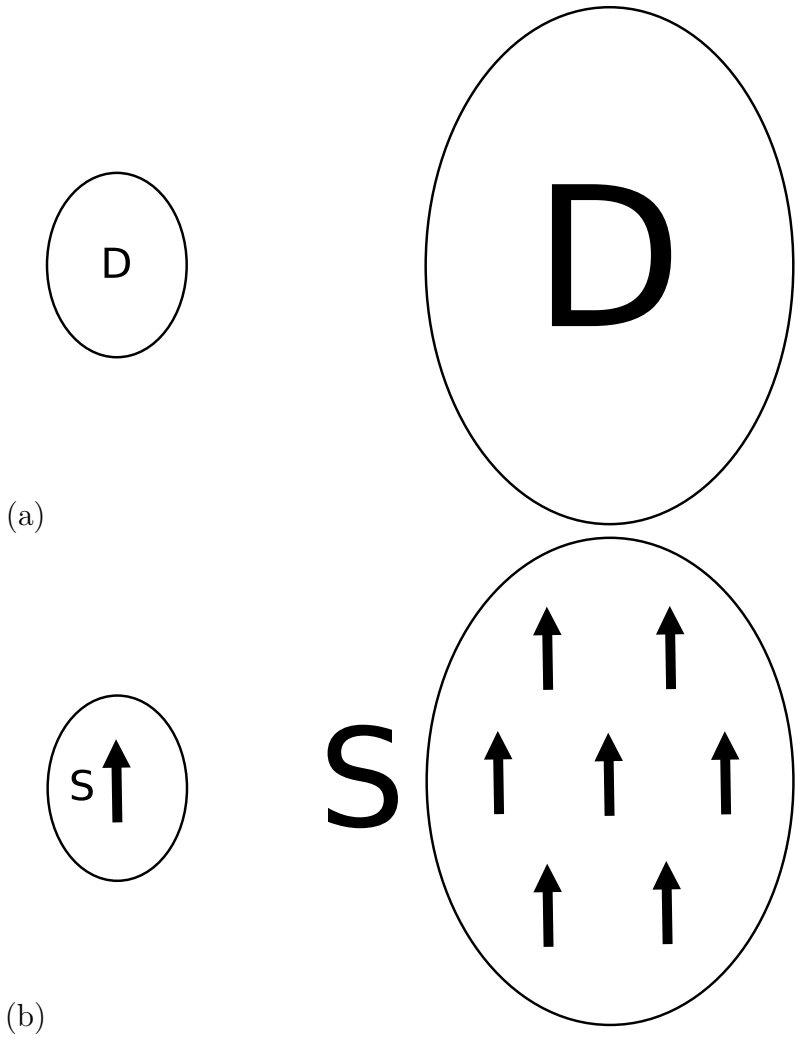

Figure 2.2: In typical magnetic nanoparticles, the magnetic anisotropy barrier is defined to be the magnetic anisotropy parameter K multiplied by the volume of the nanoparticle. In the Blume-Capel model, we model the magnetic anisotropy barrier as DS^2, where S is the total spin of the magnetic nanoparticle. As a particle size increases, we can say that (a) D increases with fixed S or (b) that D is fixed but S increases for a given value of the magnetic anisotropy barrier.

2.2.2 Glauber Transition Rate

The Glauber transition rate is derived from a coupling of a spin system to a fermionic bath [25]. The transition rate [26] (the spin-flip transition probability p) is given by

$$p = \frac{1}{1 + e^{\beta \Delta E}} \tag{2.3}$$

where $\Delta E = E_{new} - E_{old}$. Similarly to the Metropolis transition rate, E_{old} (E_{new}) denotes an energy of the spin system before (after) a single spin flip. At $T \to 0$ limit, the Glauber transition rate becomes the Metropolis transition rate.

2.2.3 Phonon-Assisted Transition Rate

The phonon-assisted transition rate was derived from consideration of transitions of states driven by lattice vibrations. In this case, it was assumed that a spin system is weakly coupled to a phonon bath, and the spin relaxation from a state $|m\rangle$ to a state $|k\rangle$ occurs via consecutive emission or absorption of a single phonon that corresponds to a change m_z by ± 1 as illustrated in Fig. 2.3. The only difference between the two states $|m\rangle$ and $|k\rangle$ is the magnetic moment at a single site by ± 1. There are two cases for the transition rate: one corresponds to the phonon absorption and the other corresponds to the phonon emission. Because a spin transition is driven by either absorption or emission of a phonon, transitions between degenerate states are not allowed with the phonon transition rate (with an exception of 1-dimensional phonon bath case).

Considering the spin-phonon coupling is a small perturbation, Ref. [18] showed that the transition rate for the phonon emission is

$$p_{km} = \frac{\lambda^2 \widetilde{N}}{\gamma \eta \hbar^{d+1} c^{d+2}} \frac{(E_m - E_k)^d}{1 - e^{-\beta(E_m - E_k)}} \tag{2.4}$$

$$\widetilde{N} = (S + m_l)(S - m_l + 1)\delta_{k_l, m_l - 1} + (S - m_l)(S + m_l + 1)\delta_{k_l, m_l + 1} \tag{2.5}$$

where λ is a spin-phonon coupling constant. d is a dimension of the phonon bath. $\gamma = 2\pi$ for the $d = 3$ phonon case and $\gamma = 2$ for the $d = 1, 2$ phonon cases. η is a mass density

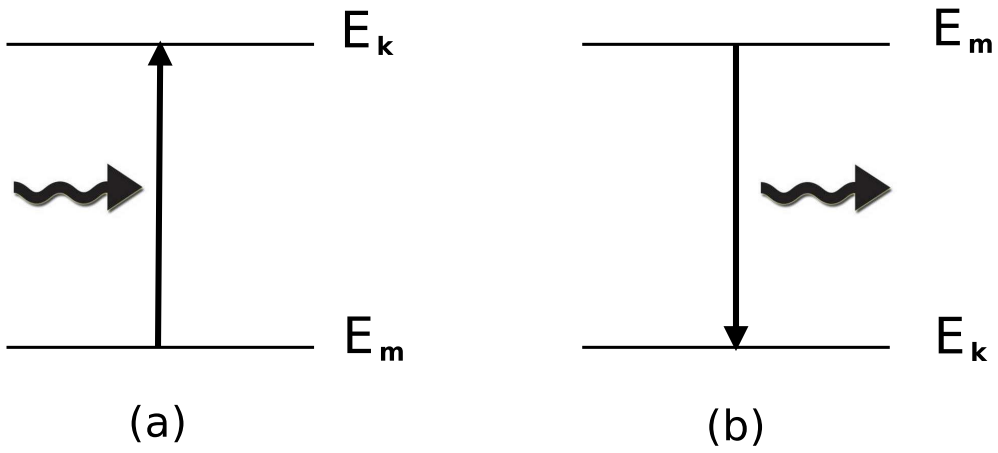

Figure 2.3: Schematic diagram of (a) a phonon absorption and (b) a phonon emission. The wavy arrows denote either emitted or absorbed phonons.

associated with the phonon bath. k_l is the quantum number of the l-th spin of the state $|k\rangle$. d is the dimension of the phonon bath. c is a speed of sound in the lattice. E_m (E_k) is the energy at state $|m\rangle$ ($|k\rangle$). When an emission of phonon occurs, the system loses energy from E_m to E_k. In case of an absorption of phonon, the transition rate is

$$p_{km} = \frac{\lambda^2 \widetilde{N}}{\gamma \eta \hbar^{d+1} c^{d+2}} \frac{(E_k - E_m)^d}{e^{\beta(E_k - E_m)} - 1}. \tag{2.6}$$

Figure 2.4 shows the $d = 1, 2$ and 3 phonon-assisted transition rate as a function of the energy difference at $\beta = 1$. Since we use $3d$ phonon-assisted transition rate exclusively in this study, Eq. (2.4) and Eq. (2.6) become

$$p_{km} = \alpha \frac{|E_m - E_k|^3}{1 - e^{-\beta(|E_m - E_k|)}}. \tag{2.7}$$

The value, $\alpha = \lambda^2 \widetilde{N} / \gamma \eta \hbar^{d+1} c^{d+2}$ is material dependent. For instance, $\alpha = 0.00041 s^{-1}$ for the single-molecule magnet Mn_{12} [18]. In the simulation, α is set to 1 for simplicity. The actual value of α can be used to associate a simulation time with a physical time. At $T \to 0$ limit, the $3d$ phonon-assisted transition rate can be approximated as follows

$$p_{km} = \begin{cases} \alpha |\Delta E|^3, & \text{if } \Delta E \leq 0 \\ \alpha \Delta E^3 e^{-\beta \Delta E}, & \text{if } \Delta E > 0 \end{cases} \tag{2.8}$$

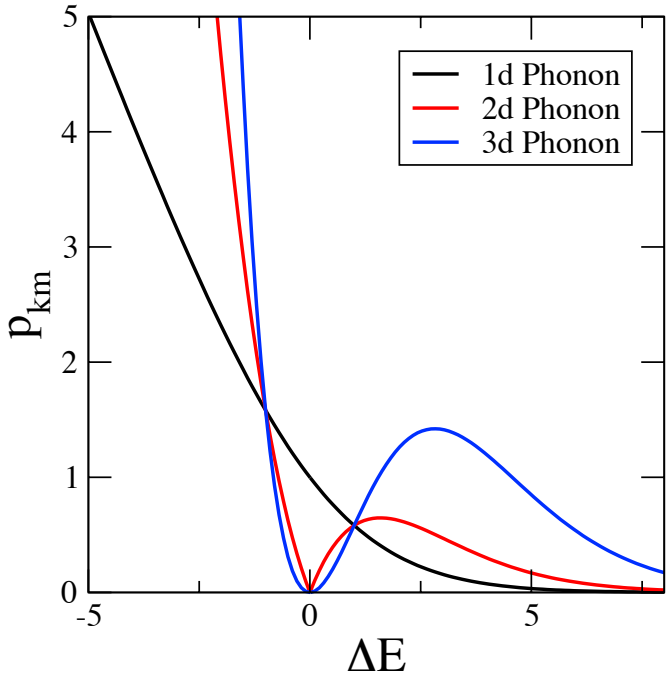

Figure 2.4: The $d = 1, 2$, and 3 phonon-assisted transition rates as functions of an energy difference at $\beta = 1$. $p_{km} = 0$ when $\Delta E = 0$ for $d = 2, 3$

where $\Delta E = E_k - E_m$. The approximated rate satisfies the detailed balance condition.

Chapter 3

Metastability in Magnetization Relaxation

Let a spin system be initially (time $t < 0$) prepared with magnetization saturated along the positive z direction. This can be realized by applying a strong magnetic field along the positive z direction. Suppose that at $t = 0$, the magnetic field is reversed. Then at $t > 0$, the initial state with all spins along the positive z direction becomes a metastable state. The state with all spins along the negative z direction becomes the ground state. Given that a thermal energy is much lower than an energy barrier Γ against nucleation (Fig. 3.1), the system remains in the metastable state for a while. Eventually, the system will overcome the energy barrier to transit to the ground state. The time where the system remains in the metastable state is referred to as the lifetime of the metastable state. The relaxation rate of magnetization increases as T or $|H|$ increase. Hence, the lifetime of the metastable state depends on T, $|H|$, and D.

The decay mechanisms of the metastable state for the Ising model apply to the Blume-Capel model. The decay mechanisms for Ising model with periodic boundary conditions were studied with the droplet theory [27] and Monte Carlo simulations [28, 29]. Here, we first briefly describe the decay mechanisms for the Ising model. In the Ising model, three

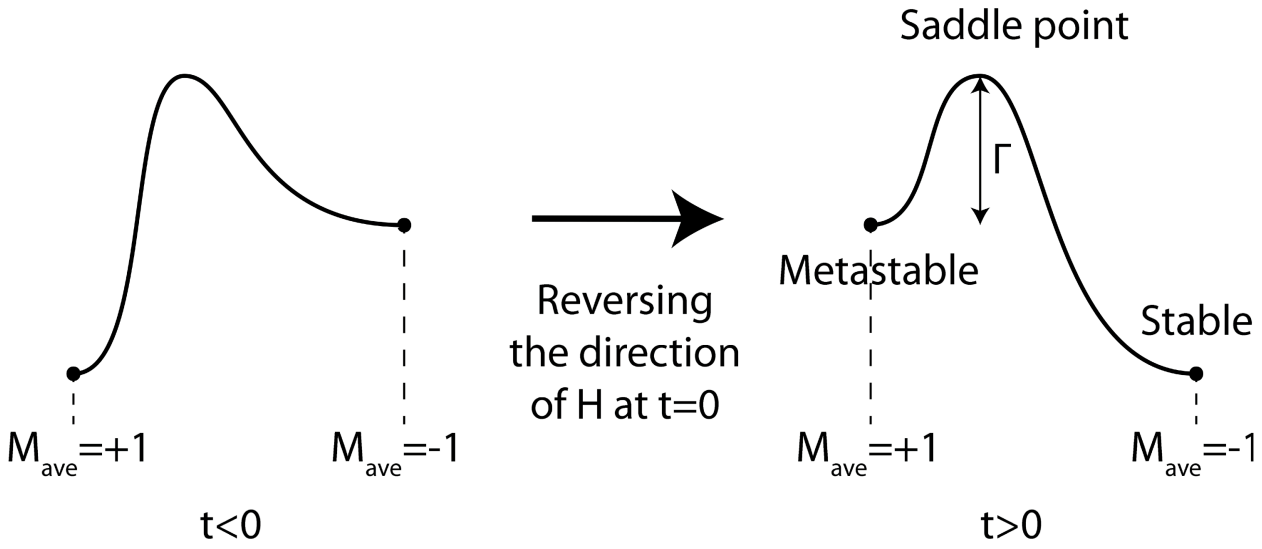

Figure 3.1: A schematic of the energy as a function of the average magnetic moment M_{ave}. The metastable well, the stable well, and the energy barrier Γ are shown. Changing the direction of magnetic field from $+z$ to $-z$ at $t = 0$ causes the system to change the stable (metastable) state to a metastable (stable) state.

decay regimes were proposed [16, 28, 29] and the schematic diagram is shown in Fig. 3.2. In a strong-field (SF) regime, the strong magnetic field causes the short metastable state ($R_c < a$) where a is the lattice spacing and R_c is the critical droplet radius (Fig. 3.3). In the SF regime, there is no metastable state in the energy landscape, and the magnetization relaxation time is short regardless of temperature. In a multi-droplet (MD) regime, multiple supercritical droplets form and grow during the decay ($a \ll R_c < R_0 \ll L$) where R_0 is the mean droplet separation and L is the system size (Fig. 3.4). The number of critical droplets depends on the system size and temperature. For a larger system, there is a more space to form additional critical droplets. In the high temperature limit, there are many critical droplets formations. As the temperature decreases, the number of the critical droplets decreases, and eventually, the system crosses over from the MD regime to a single-droplet (SD) regime at certain temperature for a given system size. The MD regime appears in the weak-field and high-temperature limit. In a single-droplet regime, the decay is driven by a

single critical droplet ($a < R_c \ll L \ll R_0$) (Fig. 3.5). In the SD regime, the system stays in a metastable state for a long period of time, and the magnetization relaxation happens instantly after the super critical droplet formation. The SD regime appears in the weak-field and low-temperature limit. The cross-overs between different decay regimes for the Ising model are shown in Fig. 3.2. Under a given lattice size L, at low temperatures, the Ising model is in the SD regime for $|H| < 4$.

For a given lattice size L in the low-temperature limit, the SD regime for the Blume-Capel model can be realized for $|H| < (D + 4)$. We calculate energy differences between different spin configurations for several initial relaxation paths. Considering these energy differences, we locate energetically favorable paths for magnetization relaxation. We find the critical droplet size and type by locating where energetically favorable paths change the sign of the energy differences. We can also find the energy barrier Γ, which is the energy difference between the initial spin configuration and the critical droplet spin configuration.

For the Ising model on a square lattice, decays of the metastable state and nucleation of droplets of the stable phase have been extensively studied as a function of $|H|$, T, and L [16, 28, 29, 30, 31]. For the BC model on a square lattice, nucleation and metastability were studied at low fields in the multi-droplet regime using the Metropolis transition rate by Ref. [22]. Here we are interested in low-temperature decays of the metastable state within the single-droplet regime for the BC model for a fixed lattice size L, where the size of the critical droplet of the stable phase is much smaller than the lattice size. For a fixed lattice size and constant D, when we take a zero-temperature limit, the single-droplet regime falls within the region defined by $|H| < (D + 4)$ [32]. We divide the single-droplet regime into different regions according to critical droplet sizes. For example, for $0 < D < 1$, at not too low fields, three regions labeled as I, II, and III are identified as a function of $|H|$ and D (Fig. 3.6). (Regions I-A, I-B, and I-C are considered as region I.) The critical droplet for the region I is a single site of spin projection $M_z = 0$. The region I has three sub-regions where the prefactor A in $\langle\tau\rangle$ for the Glauber dynamics (for constant D) changes: $A = 9/8$ for region I-A ($3 + D < |H| < 4 - D$ for $D > 0$), $A = 10/9$ for region I-B

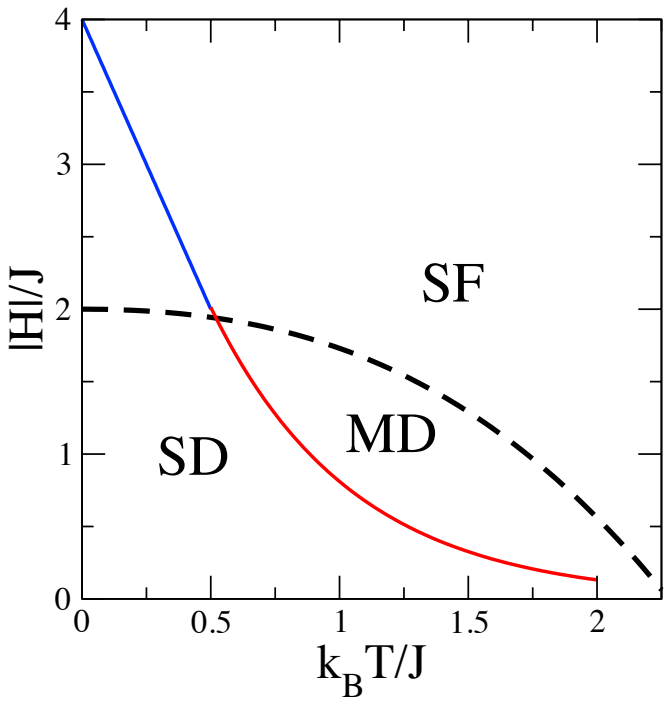

Figure 3.2: The cross-over phase diagram showing the three metastable decay regimes for the Ising model with a square lattice modified from Ref. [16]. The three metastable decay regimes are the strong-field (SF) regime, the multi-droplet (MD) regime, and the single-droplet (SD) regimes. The dashed line shows the boundary of the SF and MD regimes. The solid red curve shows the cross-over between the SD and MD regimes and depends on the system size. The solid blue line shows the cross-over between the SD and SF regimes and depends on the system size as well.

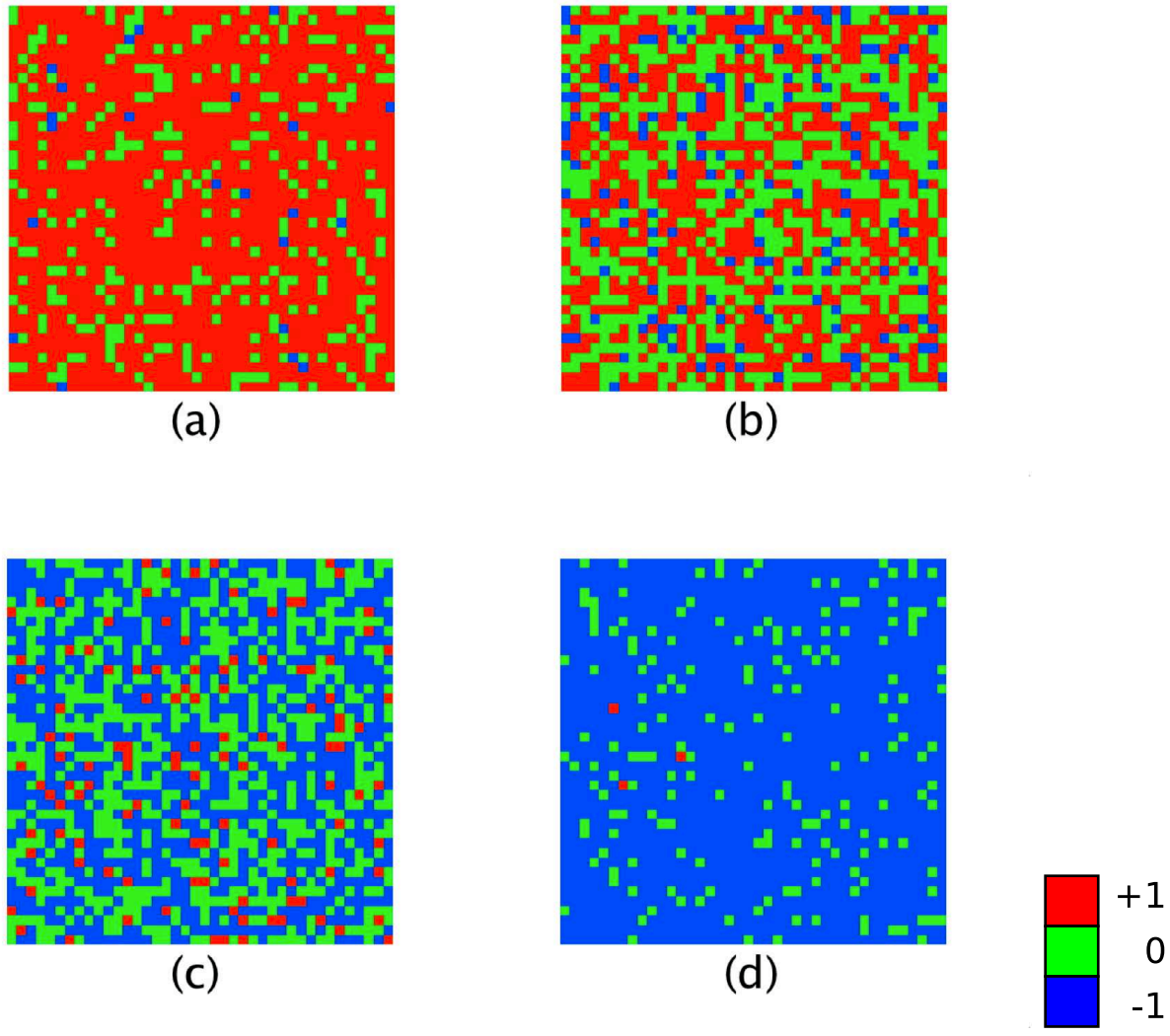

Figure 3.3: Time lapse pictures of the Blume-Capel model. Times t for (a)-(d) are 400, 1200, 4100, and 9200 Monte Carlo steps (mcs) respectively. In a strong-field regime, magnetic moments change from $+1$ to -1 in a short period of time.

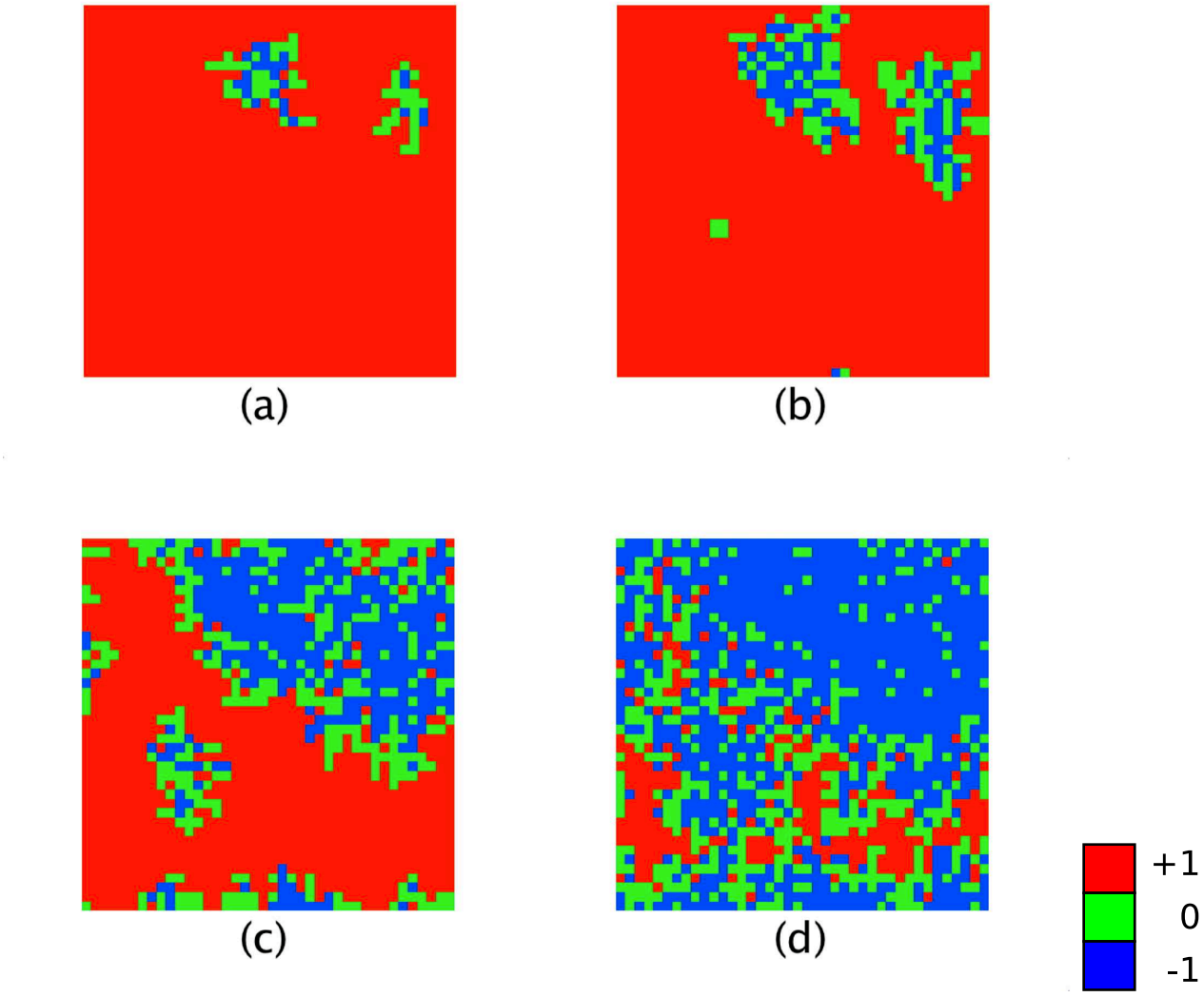

Figure 3.4: Time evolution of magnetization in a multi-droplet regime. Times t for (a)-(d) are 14700, 16840, 21030, and 25000 mcs respectively. (a) In a multi-droplet regime, there are formations of multiple supercritical droplets.

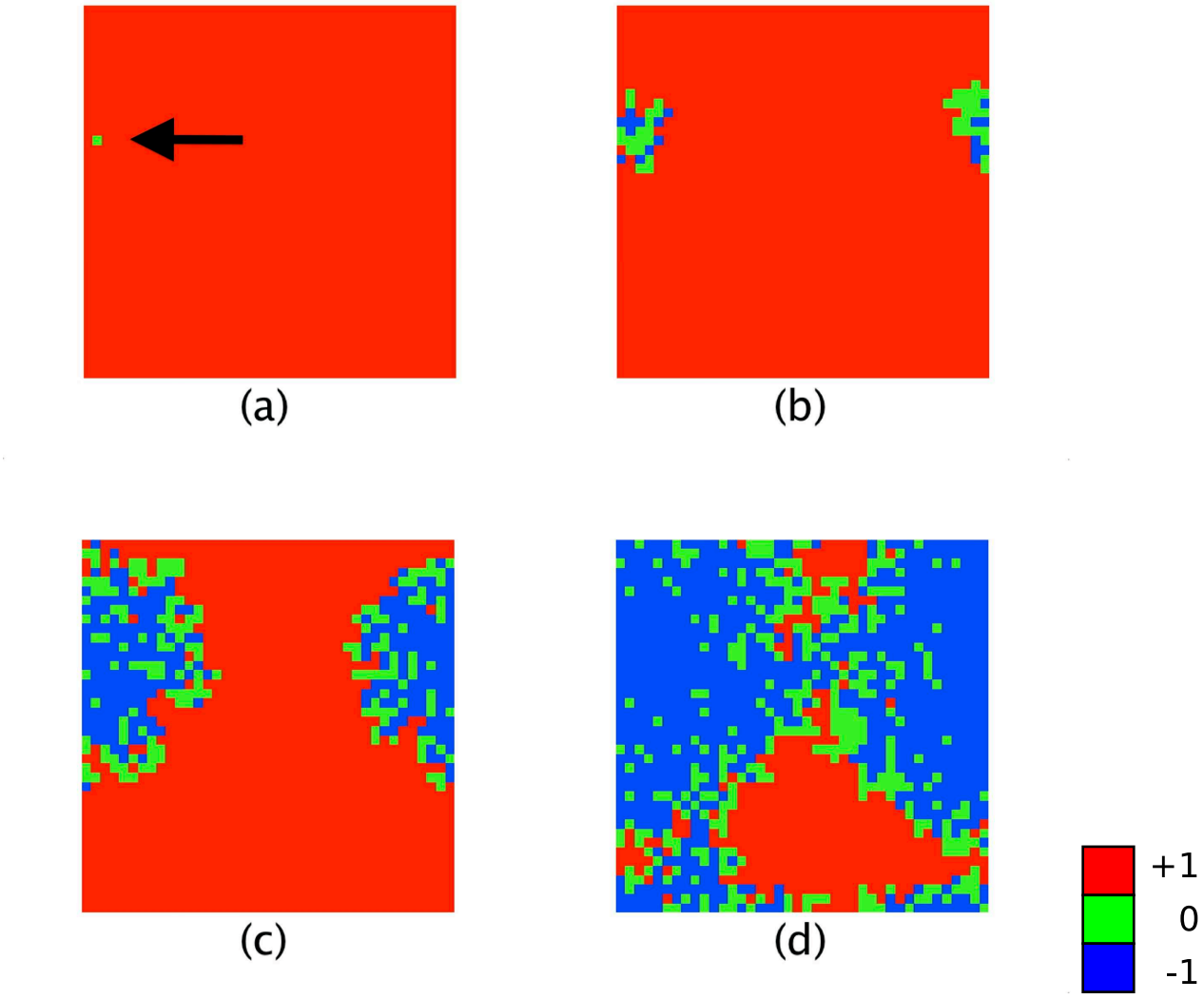

Figure 3.5: Time evolution of magnetization in a single-droplet regime. Times t for (a)-(d) are 464000, 468050, 475320, and 482400 mcs respectively. In a single-droplet regime, a single critical droplet forms after long metastability as indicated with an arrow in (a), and the supercritical droplet size grows afterward.

($4 - D < |H| < 4 + D$ for $0 < D < 0.5$ and $3 + D < |H| < 4 + D$ for $D > 0.5$), and $A = 2$ for region I-C ($4 - D < |H| < 3 + D$ for $D > 0.5$). Those prefactors are different due to the difference in attempt frequencies for the sub-regions. Figure 3.7 illustrates the differences in the energetically favorable paths at the points `b, a, e` in Fig. 3.6 where each point represents the sub-region I-A, I-B, and I-C respectively. The critical droplet for the region II ($3 - D < |H| < 3 + D$ for $D < 0.5$) consists of two nearest neighbor sites with each spin projection $M_z = 0$. The critical droplet for the region III ($2 + D < |H| < 4 - D$ for $D > 0.5$) is a single site of spin projection $M_z = -1$. For the regions II and III, there are no such sub-regions as in the region I. In Chapter 5, we investigate the case with $|H| = 4$ and $D = 0.25$ (marked as `a` in the region I-B in Fig. 3.6), using the Glauber dynamics [32]. In Chapter 6 and 7, we focus on metastability in the regions I-A and II and the boundary ($|H| = D + 3$ and $0 < D < 0.5$) between the regions I-A and II. More specifically, we vary D with H fixed as -3.25: $D = 0.125$ for the region I-A, $D = 0.375$ for the region II, and $D = 0.25$ for the boundary as marked as `b, c, d` in Fig. 3.6. Furthermore, we show calculations for the region III in Chapter 8.

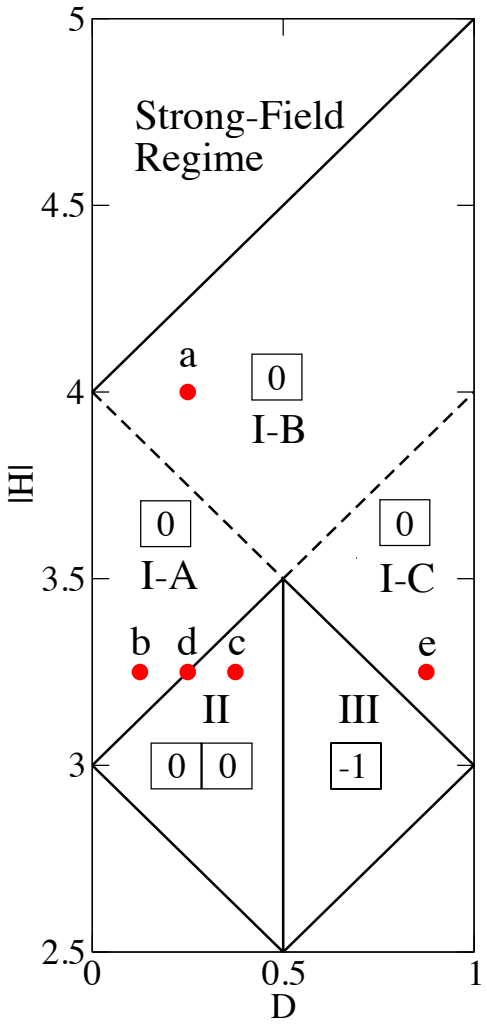

Figure 3.6: A diagram showing different single-droplet regions as a function of $|H|$ and D within the single-droplet regime in the zero-temperature limit for the BC model with $0 < D < 1$. Three regions I, II, and III are specified. The thick solid lines divide different regions, and the dashed lines divide subregions in the region I such as I-A, I-B, and I-C. For each region, critical droplets are illustrated. The point `a` is studied in Chapter 5 while the three points marked as `b`, `c`, `d` are investigated in Chapter 6 and 7. We show the calculations for the region III in Chapter 8

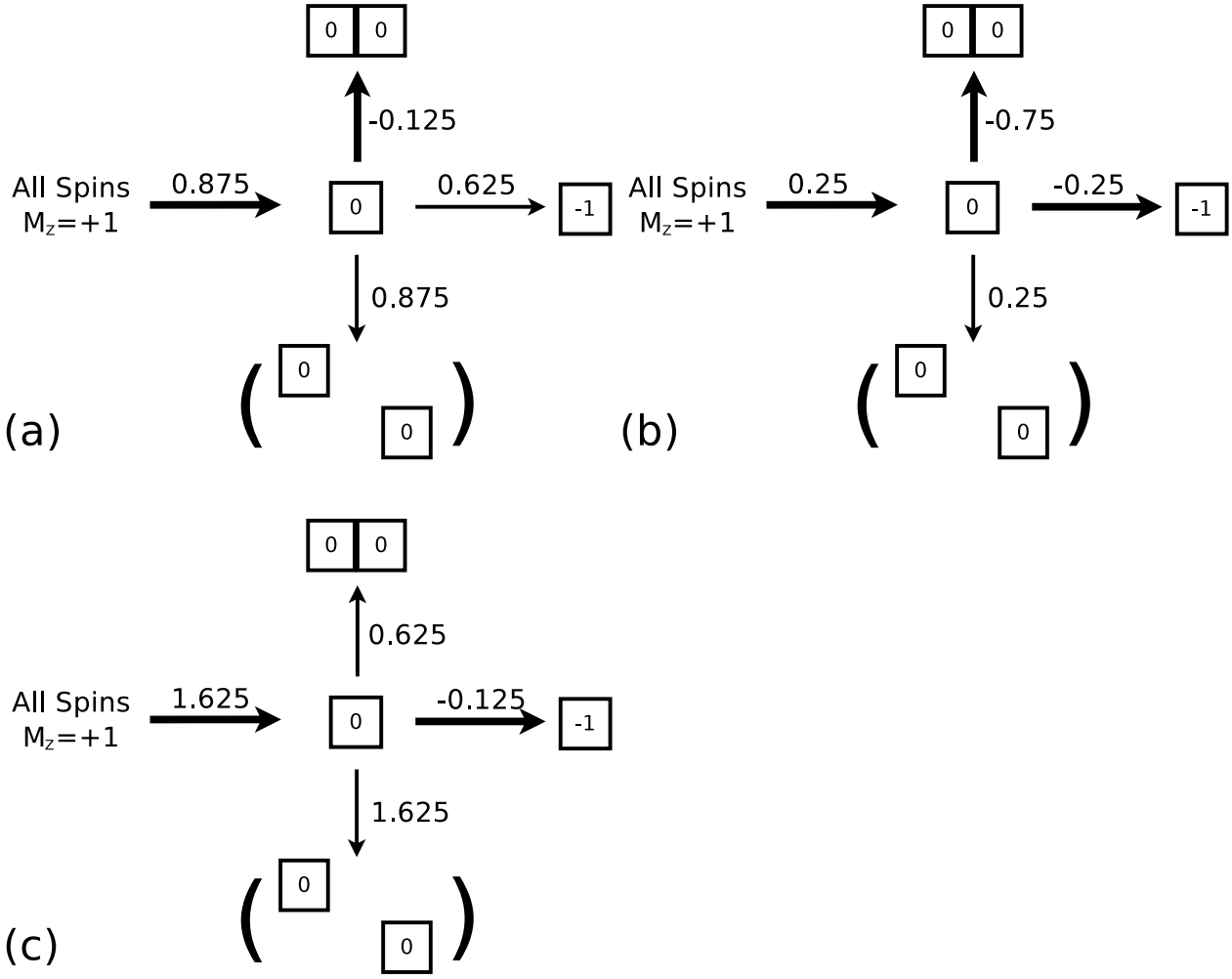

Figure 3.7: The spin paths for sub-regions of the region I: (a) region I-A at the point `b` in Fig. 3.6, (b) region I-B at the point `a`, and (c) region I-C at the point `e`. A box represents an overturned spin in a sea of spins with $M_z = +1$, and the numbers next to the arrows represent the energy differences in direction of the arrows. The difference in attempt frequencies results in different prefactors, and a high attempt frequency implies a small prefactor.

Chapter 4

Computational Methods

In this section, we discuss computational methods we used in our simulations. The computational methods for the Ising model using kinetic Monte Carlo (KMC) simulations is outlined by Novotny [16]. To study the $S = 1$ Blume-Capel model, we follow the computational methods for the Ising model and make several modifications to make them appropriate for the three-state model. Furthermore, we discuss the computational methods for the distribution cases later in this chapter.

4.1 Computational Method for Constant Magnetic Anisotropy

4.1.1 Standard Monte Carlo Method

First, we discuss the standard dynamic Monte Carlo method. The advanced algorithms we mention later are methods to reduce the computational time while keeping the physical dynamic of the standard dynamic Monte Carlo methods. Hence, the standard dynamic Monte Carlo method is the reference and also a way to validate the accuracies of the rest of

the computational methods we use. The algorithm is outlined as follows:

- Start the lattice with all N spins with $m_z = +1$. Set time t to zero.
- Perform the following steps until the magnetization M reaches zero.
  - Increment t to $t + 1$.
  - Calculate two random numbers r_1 and r_2.
  - Randomly choose a spin out of the N spins using r_1.
  - Calculate the energy E_{old} of the current spin configuration and E_{new} of the spin configuration where the magnetic moment of the chosen spin is changed by $+1$ (-1). The energy of a given spin configuration is given by the Eq. (2.1).
  - Calculate the probability to change the magnetic moment using the Glauber transition rate or the phonon-assisted transition rate.
  - Use r_2 and the transition rate to determine whether to update the spin configuration to the new configuration or to retain the old spin configuration. If $r_2 \leq p(E_{\text{new}} - E_{\text{old}})$, then the spin configuration is updated. Otherwise, reject the new configuration. $p(E_{\text{new}} - E_{\text{old}})$ is a transition rate.

It is crucial to use a good pseudorandom generator for Monte Carlo simulations. We use the random number generator proposed by George Marsaglia at Florida State University [33] and modified by F. James [34] to produce an array of pseudorandom numbers. Note that instead of randomly choosing a spin out of the N spins, it is also possible to choose a spin by going through the rows in order, and taking this approach may lead to different results. For our simulations, we exclusively choose spins randomly.

A Monte Carlo step (mcs) is a simulation time scale. To obtain the time scale that can be associated to a physical time, we need Monte Carlo step per spin (MCSS) obtained from dividing the Monte Carlo step by the system size. Since the time scale for a spin-flip trial

is set by the heat reservoir, MCSS correspond to an inverse phonon frequency (in order of 10^{-13} second) for the spins interacting with phonons [16].

4.1.2 Absorbing Markov Chains

The advanced algorithms discussed later incorporate absorbing Markov chains (AMC). We consider an absorbing Markov chain with s transient states and r absorbing states. The system is initially in one of the s transient states and remains in the transient subspace until absorbed into one of the r absorbing states. The absorbing Markov chain transition matrix (Markov matrix) is defined as

$$\mathbf{M}_{(r+s)\times(r+s)} = \begin{pmatrix} \mathbf{I}_{r\times r} & \mathbf{0}_{r\times s} \\ \mathbf{R}_{s\times r} & \mathbf{T}_{s\times s} \end{pmatrix}, \tag{4.1}$$

where matrix $\mathbf{I}$ is an identity matrix, the matrix $\mathbf{0}$ is a matrix consisting of all zero elements, the matrix $\mathbf{T}$ is the transient matrix which contains transition probabilities between the s transient states, and the matrix $\mathbf{R}$ is the recurrent matrix which contains transition probabilities from the transient subspace to the r absorbing states. The probability of remaining in one of the s transient states after m time step is given in Ref. [16] as

$$p_{\text{remain in transient subspace}} = \vec{v}_{\mathrm{I}}^{\mathrm{T}} \mathbf{T}^m \vec{e}, \tag{4.2}$$

and the average lifetime to exit from the transient subspace is

$$\langle \tau \rangle = \vec{v}_{\mathrm{I}}^{\mathrm{T}} (\mathbf{I} - \mathbf{T})^{-1} \vec{e} \tag{4.3}$$

where $\vec{v}_{\mathrm{I}}^{\mathrm{T}}$ is the s-state initial vector, and $\vec{e}$ is a unit vector. After exiting from the transient subspace, the system is absorbed into one of r absorbing states. We used Eq. (4.2) to calculate an exit time from the current spin configuration in the n-fold way and the MCAMC algorithms, and simulation time (in units of Monte Carlo step) is set to this time. We also used Eq. (4.3) to calculate the average lifetime in the AMC method calculations.

4.1.3 n-fold way algorithm for three-state systems with constant magnetic anisotropy

In a standard Monte Carlo algorithm, computational time is proportional to simulated physical time. In the case of weak magnetic field and low temperature, the system of interest spends long CPU time in the initial or metastable states, so that KMC simulations using a standard MC algorithm are not practical. There exist, however, several advanced algorithms to circumvent this when D is constant. One such algorithm is the n-fold way algorithm [16]. The n-fold way algorithm is an event-driven algorithm where the state of the system is changed in one algorithmic step, and simulation time is incremented by the time required to make the transition. When the spin system is in a metastable state in the low-temperature, the probability of the transition to be out of the metastable well is very small. Using the n-fold way algorithm, we can save the computational time for the mostly unsuccessful spin-flip attempts.

In the n-fold way algorithm, each spin is classified into a spin class with its spin orientation and the sum of its nearest-neighbor spin orientations. This algorithm works well for the Ising model where a given spin has only one possible spin flip. A modification is necessary for a three-state model because a spin with $m_z = 0$ has two possibilities in spin flip (either $m_z = +1$ or $m_z = -1$) as shown in Figure 4.1. Depending on the spin flip, the energy change differs, and one must accommodate this into the algorithm. In case of $S = 1$ BC model (a three-state model), each spin is classified into one of $n = 27$ spin classes according to the spin orientation $(+1, 0, -1)$ and the sum of the nearest-neighbor spin orientations $(0, \pm1, \pm2, \pm3, \pm4)$. The 27 spin classes are listed in Table 4.1. n_i is the number of spins in class i, and p_i is the spin-flip probability of the given spin in class i. For spin classes $1 - 18$, p_i is simply the probability from the Glauber dynamics or the phonon dynamics since there are only one possible spin flip (Fig. 4.1(a)). For spin classes $19 - 27$, we make an adjustment to accommodate the n-fold way to the three-state model by introducing $p_i = (p_i^+ + p_i^-)/2$, where $p_i^+ = p_i(m_z = 0 \to 1)$ is the spin flip from $m_z = 0$ to 1, and $p_i^- = p_i(m_z = 0 \to -1)$

is the spin flip from $m_z = 0$ to -1 (Fig. 4.1(b)). Then, we follow the discrete-time version of the n-fold way algorithm. The probability of randomly choosing a spin in class i is n_i/N, and that of flipping the spin is p_i. Hence, the probability of flipping any spin in class i is $n_i p_i/N$. We use a quantity

$$Q_i = \frac{1}{N}\sum_{j=1}^{i} n_j p_j, \quad 1 \leq i \leq n = 27 \tag{4.4}$$

and $Q_0 = 0$ by definition. Q_i is the probability of flipping a spin in class 1 through class i. This quantity is used to determine the exit time from a current spin configuration. The absorbing Markov matrix in this case is

$$\mathbf{M} = \frac{1}{N}\begin{pmatrix} N & 0 & 0 & \cdots & 0 & 0 \\ 0 & N & 0 & \cdots & 0 & 0 \\ 0 & 0 & N & \cdots & 0 & 0 \\ \vdots & \vdots & \vdots & \ddots & \vdots & \vdots \\ 0 & 0 & 0 & \cdots & N & 0 \\ n_1 p_1 & n_2 p_2 & n_3 p_3 & \cdots & n_{27} p_{27} & \mathbf{T_{1,1}} \end{pmatrix}$$

where $\mathbf{T_{1,1}} = N(1-Q_{27})$ is the 1×1 transient matrix. Using Eq. (4.2) and a random number $\bar{r}$, the time m to exit from the current state must satisfy

$$\vec{v}_{\mathrm{I}}^{\mathrm{T}}\mathbf{T}^m\vec{e} < \bar{r} \leq \vec{v}_{\mathrm{I}}^{\mathrm{T}}\mathbf{T}^{m-1}\vec{e}. \tag{4.5}$$

Hence, the exit time m can be written as

$$m = \left\lfloor \frac{\ln(\bar{r})}{\ln(1-Q_{27})} \right\rfloor + 1 \tag{4.6}$$

where $\bar{r}$ is a random number and $\lfloor x \rfloor$ is the integer part of x. The exit time is given in terms of Monte Carlo spin-flip attempts.

Table 4.1: The 27 classes of $S = 1$ Blume-Capel model spins on a square lattice.

Class Number	Spin Orientation	Sum of Nearest-Neighbor Spin Orientations	$\Delta E = E_{new} - E_{old}$
1	$+1$	$+4$	$4 - \|H\| + D$
2	$+1$	$+3$	$3 - \|H\| + D$
3	$+1$	$+2$	$2 - \|H\| + D$
4	$+1$	$+1$	$1 - \|H\| + D$
5	$+1$	0	$-\|H\| + D$
6	$+1$	-1	$-1 - \|H\| + D$
7	$+1$	-2	$-2 - \|H\| + D$
8	$+1$	-3	$-3 - \|H\| + D$
9	$+1$	-4	$-4 - \|H\| + D$
10	-1	$+4$	$-4 + \|H\| + D$
11	-1	$+3$	$-3 + \|H\| + D$
12	-1	$+2$	$-2 + \|H\| + D$
13	-1	$+1$	$-1 + \|H\| + D$
14	-1	0	$\|H\| + D$
15	-1	-1	$1 + \|H\| + D$
16	-1	-2	$2 + \|H\| + D$
17	-1	-3	$3 + \|H\| + D$
18	-1	-4	$4 + \|H\| + D$
19	0	$+4$	$-4 + \|H\| - D$ or $4 - \|H\| - D$
20	0	$+3$	$-3 + \|H\| - D$ or $3 - \|H\| - D$
21	0	$+2$	$-2 + \|H\| - D$ or $2 - \|H\| - D$
22	0	$+1$	$-1 + \|H\| - D$ or $1 - \|H\| - D$
23	0	0	$\|H\| - D$ or $-\|H\| - D$
24	0	-1	$1 + \|H\| - D$ or $-1 - \|H\| - D$
25	0	-2	$2 + \|H\| - D$ or $-2 - \|H\| - D$
26	0	-3	$3 + \|H\| - D$ or $-3 - \|H\| - D$
27	0	-4	$4 + \|H\| - D$ or $-4 - \|H\| - D$

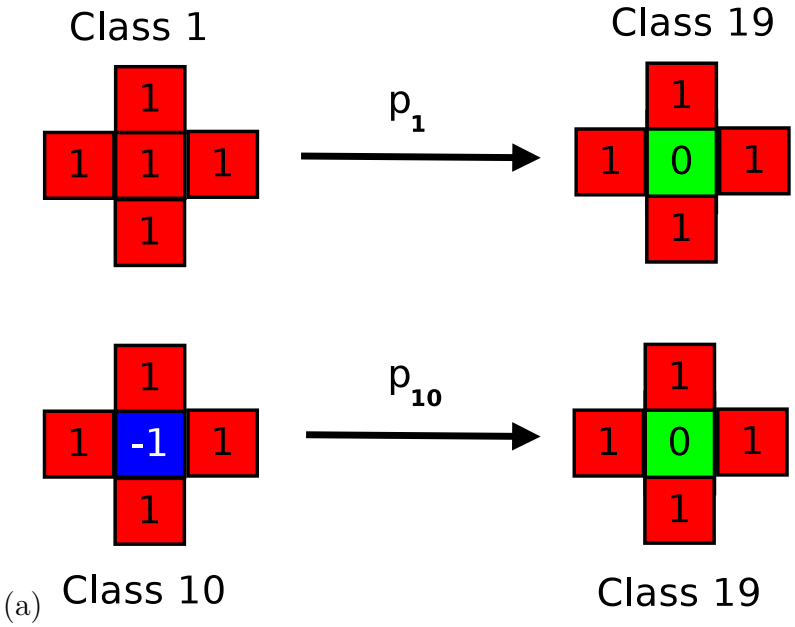

(a)

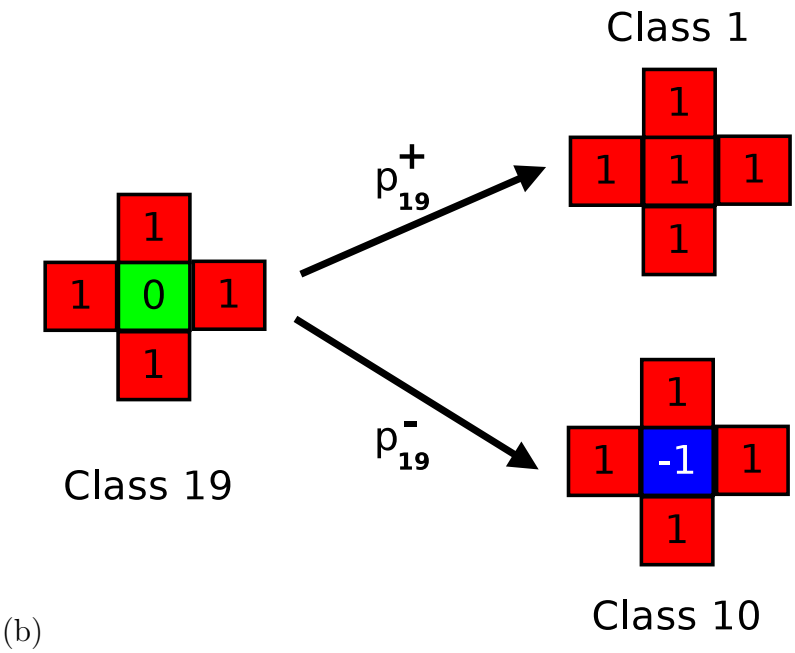

(b)

Figure 4.1: (a) Spin classes 1-18 have single transition upon change in magnetic moment. (b) Spin classes 19-27 have two possible transitions. Spin class 19 have p_{19}^{+} and p_{19}^{-}.

4.1.4 $s = 2$ MCAMC Algorithm for the $S = 1$ Blume-Capel Model with a Constant Magnetic Anisotropy

In the weak field limit, the size of the metastable well becomes large, and the system requires multiple steps from the initial state to overcome the energy barrier. In this case, even the n-fold way may require a large amount of computational time. One can further reduce the amount of computational time by using more states in the transient subspace. Monte Carlo with absorbing Markov chains (MCAMC) is such a method that uses s states in the transient subspace (two states are used in $s = 2$ MCAMC). In a simulation, we use MCAMC whenever the system is in the initial state, and use n-fold way algorithm afterward to speed up the computational time. This method is useful for studying the region II in Fig. 3.6 ($3 - D < |H| < 3 + D$ for $D < 0.5$). The transient matrix and the recurrent matrix for $s = 2$ MCAMC are as follows

$$\mathbf{T}_{s=2} = \begin{pmatrix} 1 - \frac{N-5}{p_1} - \frac{4p_2}{N} - \frac{p_{19}^- + p_{19}^+}{2N} & \frac{p_{19}^+}{2N} \\ p_1 & 1 - p_1 \end{pmatrix}, \tag{4.7}$$

$$\mathbf{R}_{s=2} = \frac{1}{N} \begin{pmatrix} 4p_2 & \frac{p_{19}^-}{2} & (N-5)p_1 \\ 0 & 0 & 0 \end{pmatrix}. \tag{4.8}$$

The transient states and absorbing states are shown in Figure 4.2. The transient states are (a) the initial state where all $m_z = +1$ and (b) N spin configurations with one spin with $m_z = 0$. The absorbing states are (c) $2N$ configurations with two nearest-neighbor spins with $m_z = 0$, (d) N spin configurations with one spin overturned to $m_z = -1$, and (e) $N(N-5)/2$ configurations with two non-nearest neighbor overturned spins with both $m_z = 0$. In the MCAMC algorithm, if the system is in the initial state where all spins have $m_z = +1$ or returns to the initial state, the absorbing Markov chain portion of the algorithm is used while incorporating Eqs. (4.7) and (4.8). If the system has a total magnetization $M < N - 2$, then the normal n-fold way ($s = 1$ MCAMC) algorithm is used.

The time m to exit the absorbing Markov chain can be obtained using Eq. (4.5). For $s \geq 2$, however, Eq. (4.5) does not have a closed form while it can be solved with a bracketing

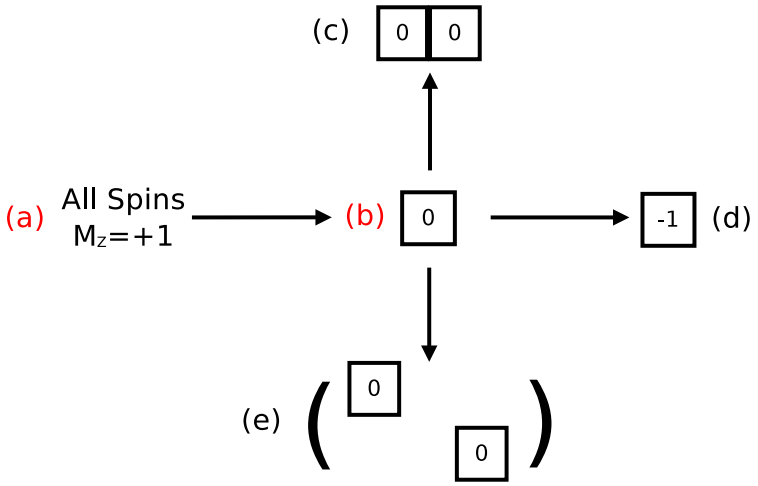

Figure 4.2: The transient and absorbing states used in the $s = 2$ AMC method. Two transient states (a) and (b) and three absorbing states (c)-(e) are used. In the region II and III, the energy differences between the configurations shown are all positive (in the direction of the arrow).

and bisection method [35]. The bracketing and bisection method, however, is not efficient method and results in spending a substantial amount of computational time. Instead of using bracketing and bisection method, we used eigenvalues of the transient matrix to approximate the time to exit from the transient subspace. In case of $s = 2$ AMC case, by diagonalizing the transient matrix with $\mathbf{T} = V\Lambda\tilde{V}$, Eq. (4.2) becomes

$$\vec{v}_{\rm I}^{\rm T}\mathbf{T}^m_{s=2}\vec{e} = (0,1)V\Lambda^m\tilde{V}\begin{pmatrix}1\\1\end{pmatrix} \tag{4.9}$$

$$= (0,1)\begin{pmatrix}V_{11} & V_{12}\\ V_{21} & V_{22}\end{pmatrix}\begin{pmatrix}\lambda_1^m & 0\\ 0 & \lambda_2^m\end{pmatrix}\begin{pmatrix}\tilde{V}_{11} & \tilde{V}_{12}\\ \tilde{V}_{21} & \tilde{V}_{22}\end{pmatrix}\begin{pmatrix}1\\1\end{pmatrix} \tag{4.10}$$

$$= V_{21}\lambda_1^m(\tilde{V}_{11}+\tilde{V}_{12}) + V_{22}\lambda_2^m(\tilde{V}_{21}+\tilde{V}_{22}) \tag{4.11}$$

where λ_1 and λ_2 are two eigenvalues of the transient matrix. They are

$$\lambda_{1,2} = 1 + \frac{1}{2}\left[-(a_1+a_2+b+p_1) \pm \sqrt{(a_1+a_2+b+p_1)^2 - 4(a_1+a_2)p_1}\right], \tag{4.12}$$

$$a_1 = \frac{4p_2}{N} + \frac{p_{19}^-}{2N} \tag{4.13}$$

$$a_2 = \frac{N-5}{N} p_1 \tag{4.14}$$

$$b = \frac{p_{19}^+}{2N}. \tag{4.15}$$

In zero temperature limit, a_1, a_2, and p_1 become small, and it follows that

$$\lambda_{1,2} = 1 + \frac{1}{2}\left[-(a_1+a_2+b+p_1) \pm (a_1+a_2+b+p_1)\left(1 - \frac{2(a_1+a_2)p_1}{(a_1+a_2+b+p_1)^2} + \dots\right)\right]. \tag{4.16}$$

Hence, the eigenvalues λ_1 and λ_2 of the transient matrix are as follows:

$$\lambda_1 = 1 - a_1 + a_2 + b + p_1 + \frac{(a_1+a_2)p_1}{a_1+a_2+b+p_1}, \tag{4.17}$$

$$\lambda_2 = 1 - \frac{(a_1+a_2)p_1}{a_1+a_2+b+p_1}. \tag{4.18}$$

At low temperature λ_2 approaches unity while λ_1 approaches $1 - (8p_2 + p_{19}^- + p_{19}^+)/2N$. Typically, time m at low temperature in SD regime is quite large, and $\lambda_2^m \gg \lambda_1^m$. Combining Eq. (4.5) and Eq. (4.11), the time m to exit from the transient subspace in this case is, hence,

$$m = 1 + \frac{\ln\left[\frac{\bar{r}}{V_{22}(\tilde{V}_{21}+\tilde{V}_{22})}\right]}{\ln \lambda_2}. \tag{4.19}$$

λ_2 approaches unity in the low-temperature limit, and computing λ_2 in a simulation normally requires a multiprecision software. Alternatively, one can perform a series expansion of $\ln \lambda_2$ in Eq. (4.19) and keep several terms to bypass a need for a multiprecision software.

4.1.5 $s = 3$ MCAMC for the Spin $S = 1$ Blume-Capel Model

It is also possible to use the higher s MCAMC. The higher s MCAMC is useful for studying a large critical droplet size in the SD regime. For $s = 3$ MCAMC, there are more than one possible way of selecting the transient and recurrent states. The MCAMC works effectively when the critical droplet spin configuration is included in the transient subspace. In the

region I, II, and their region boundary for the Glauber dynamics, one can use the following transient and recurrent matrices.

$$\mathbf{T}_{s=3} = \begin{pmatrix} 1-\frac{N-8}{N}p_1 - \frac{2p_{20}^-}{2N} - \frac{6p_2}{N} - \frac{p_{20}^+}{N} & \frac{p_{20}^+}{N} & 0 \\ \frac{4p_2}{N} & 1-\frac{N-5}{p_1} - \frac{4p_2}{N} - \frac{p_{19}^- + p_{19}^+}{2N} & \frac{p_{19}^+}{2N} \\ 0 & p_1 & 1-p_1 \end{pmatrix}, \quad (4.20)$$

$$\mathbf{R}_{s=3} = \frac{1}{N}\begin{pmatrix} 0 & 2p_{20}^- & 0 & (N-8)p_1 & 6p_2 \\ p_{19}^- & 0 & (N-5)p_1 & 0 & 0 \\ 0 & 0 & 0 & 0 & 0 \end{pmatrix}. \quad (4.21)$$

The additional transient state to the $s = 2$ MCAMC is all $2N$ spin configurations with two nearest-neighbor spins with spin projection $m_z = 0$ for both spins. The additional absorbing states to the $s = 2$ MCAMC are (i) two nearest-neighbor spins with spin projection $m_z = 0$ for one of the spin and $m_z = -1$ for another, (ii) three-nearest-neighbor spins with spin projection $m_z = 0$, and (iii) two nearest-neighbor spins with $m_z = 0$ and one non-nearest-neighbor single spin with $m_z = 0$ (Fig. 4.3).

In the region III and at the boundary between the region I and II using the phonon dynamics, one must use the following transient and recurrent matrices.

$$\mathbf{T}_{s=3} = \begin{pmatrix} 1-\frac{N-5}{N}p_1 - \frac{4p_3}{N} - \frac{p_{10}}{N} & \frac{p_{10}}{N} & 0 \\ \frac{p_{19}^-}{2N} & 1-\frac{N-5}{p_1} - \frac{4p_2}{N} - \frac{p_{19}^- + p_{19}^+}{2N} & \frac{p_{19}^+}{2N} \\ 0 & p_1 & 1-p_1 \end{pmatrix}, \quad (4.22)$$

$$\mathbf{R}_{s=3} = \frac{1}{N}\begin{pmatrix} 0 & 4p_3 & 0 & (N-5)p_1 \\ p_2 & 0 & (N-5)p_1 & 0 \\ 0 & 0 & 0 & 0 \end{pmatrix}. \quad (4.23)$$

The additional transient state to the $s = 2$ MCAMC is all the N spin configurations with one spin having a spin projection of $m_z = -1$. The additional absorbing states to the $s = 2$ MCAMC are (i) two nearest-neighbor spins with spin projection $m_z = 0$ for one of the spin and $m_z = -1$ for another and (ii) two non-nearest-neighbor single spins where one spin having a spin projection of $m_z = -1$ and another spin with $m_z = 0$ (Fig. 4.4). We applied the $s = 3$ AMC method for analytical calculations of the average lifetime (Sec. 4.3).

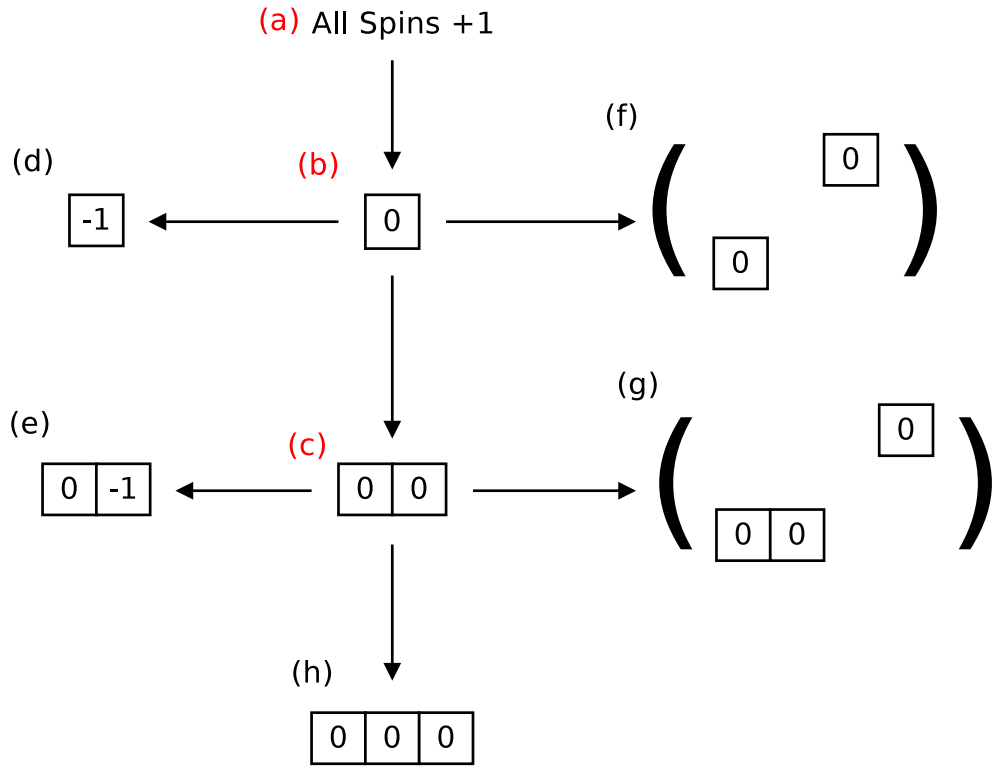

Figure 4.3: The transient and absorbing states used in the $s = 3$ AMC. Three transient states (a)-(c) and five absorbing states (d)-(h) are selected.

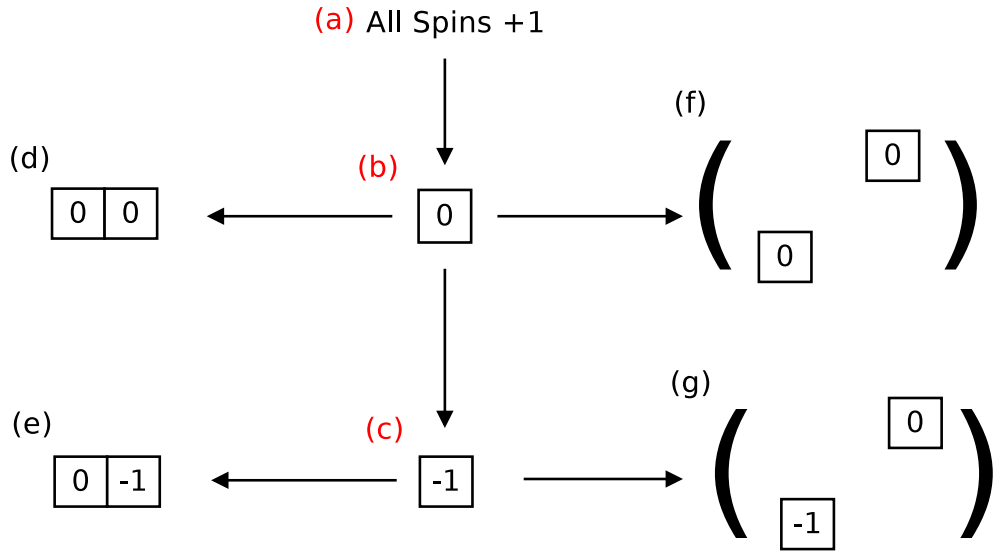

Figure 4.4: The alternative choice of the transient and absorbing states used in the $s = 3$ AMC. Three transient states (a)-(c) and four absorbing states (d)-(g) are used.

4.2 Computational Method for Distribution of Magnetic Anisotropy

To study the system with a distribution of D, we used a random number to generate and assign the values of D to each lattice site. For Gaussian distributions of D, a Box-Muller transformation [36] in a polar form is used to generate normally distributed random numbers. Figure 4.5 shows samples of normally distributed parameter Ds used in the MC simulations. The spin systems with a distribution of magnetic anisotropy can be studied using a standard MC algorithm without a significant modification. Although the advanced algorithms such as the n-fold way algorithm [37] or the MCAMC [16, 17] algorithms are successfully implemented to the Blume-Capel model with the constant value of D, the advanced algorithms require modifications when the system has a distribution of D. The reason is that the value of D differs at different sites (determined by distributions of D), which prevents setting spin classes with identical energies.

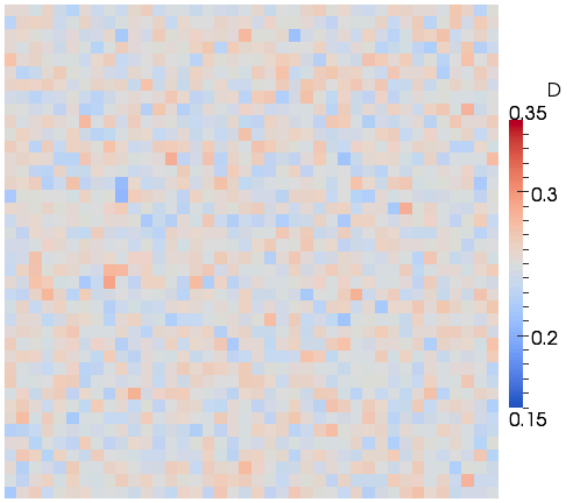

(a)

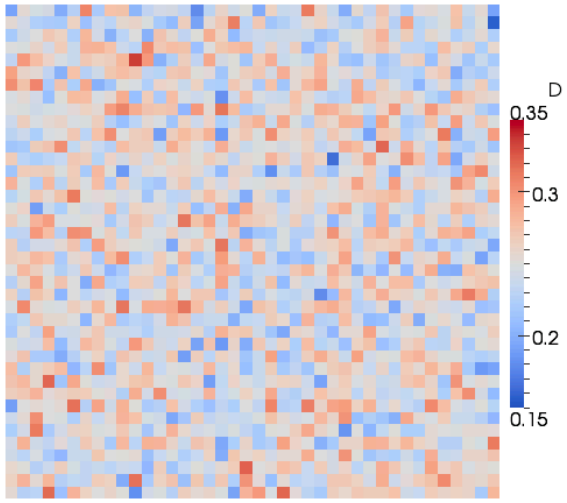

(b)

Figure 4.5: Two of the distributions of D used in the MC simulations with the mean value $D_0 = 0.25$. These distributions are generated with a Box-Muller transformation in a polar form with different values in σ_D: (a) $\sigma_D = 0.0125$ and (b) $\sigma_D = 0.025$.

4.2.1 n-fold Way Algorithm for Systems with a Distribution of Magnetic Anisotropy

When a distribution of D is introduced, one must treat every lattice site individually to reflect randomness of the D values of the lattice sites. Hence, we partition the probability of flipping a spin not according to a spin class but according to a lattice site. Then, the probability is p_i/N, considering $1/N$ is the probability of randomly choosing a lattice site and that p_i is the probability of flipping the particular site. This leads to N absorbing states and one transient state. We label each spin with a number 1 through N and modify Eq. (4.4) as

$$Q_i = \frac{1}{N}\sum_{j=1}^{i} p_j \quad 1 \leq i \leq N \tag{4.24}$$

where $Q_0 = 0$. This time Q_i is a probability of flipping a spin with label 1 through i. It incorporates lattice sites instead of spin classes. The absorbing Markov matrix for exiting from the current spin configuration is given as

$$\mathbf{M} = \frac{1}{N}\begin{pmatrix} N & 0 & 0 & \cdots & 0 & 0 \\ 0 & N & 0 & \cdots & 0 & 0 \\ 0 & 0 & N & \cdots & 0 & 0 \\ \vdots & \vdots & \vdots & \ddots & \vdots & \vdots \\ 0 & 0 & 0 & \cdots & N & 0 \\ p_1 & p_2 & p_3 & \cdots & p_N & \mathbf{T_{1,1}} \end{pmatrix}$$

with the transient matrix of $\mathbf{T_{1,1}} = N(1 - Q_N)$. Notice that this absorbing Markov matrix has almost a size of system size $(N + 1 \times N + 1)$ while the previous matrix has almost a size of number of spin classes (28×28) (Fig. 4.6). For constant D, it is sufficient to update n_i's in the Markov matrix. But for distribution of D one needs to update p_i's due to randomness in D. Then, we follow the standard n-fold way algorithm to determine spin flips and Monte Carlo time updates. The exit time from the transient subspace in this case is

$$m = \left\lfloor \frac{\ln(\bar{r})}{\ln(1 - Q_N)} \right\rfloor + 1. \tag{4.25}$$

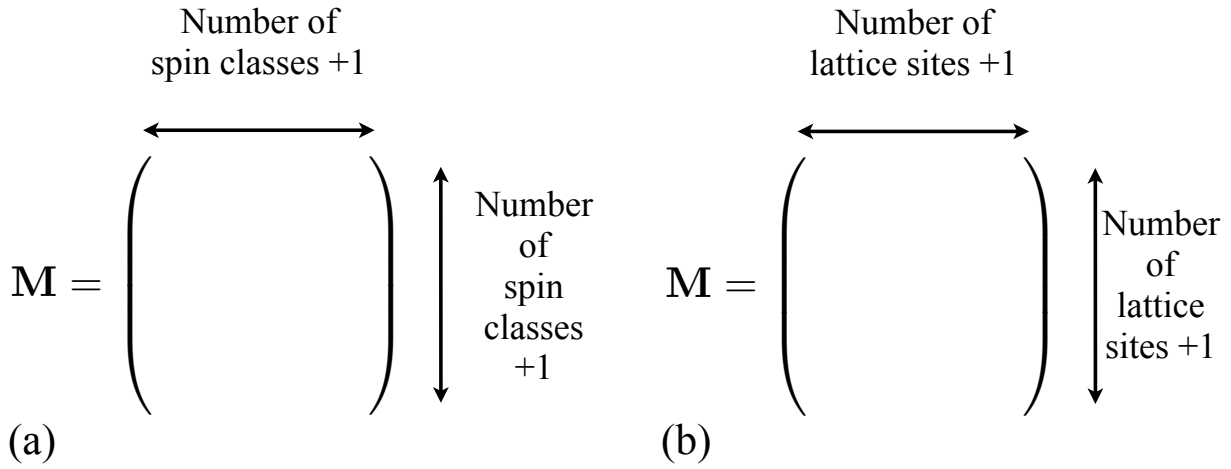

Figure 4.6: A diagram showing the difference in the size of the absorbing Markov matrix for (a) the standard n-fold way algorithm and (b) the modified n-fold way algorithm used in the case of distribution of D.

Because the absorbing Markov matrix must be updated for every Monte Carlo loop and a large Markov matrix requires a longer time for the update, this method is not always computationally efficient. Hence, we switch from this method to the standard Monte Carlo method once the system exits from the initial state where the modified n-fold way algorithm is most effective.

4.3 AMC Method

To analytically calculate the average lifetime for constant D, we used the $s = 2$ AMC method with two transient states and $s = 3$ AMC method with three transient states. For the region I the $s = 2$ AMC method is used, but for the regions II and III, we must use the $s = 3$ AMC method. The magnetization of the spin system reaches to zero shortly after a critical droplet is formed in the single-droplet regime. Hence, the average lifetime is approximately the time to exit from the transient subspace in the AMC. Using the transient states and

several absorbing states, we create a transition matrix for the AMC and find an analytic form for the exit time. For details of the AMC method, see Ref. [16]. In the $T \to 0$ limit, we expect that the analytic form should be a good approximation to the average lifetime from our KMCS. For Gaussian distributions of D, we first calculate an average of each relevant spin-flip probability by integrating the probability over D, and use the averages in the analytic form of the exit time for constant D [32]. In this case, we assume that N is so large that a summation over the lattice sites approximates an integral. Thus, we expect that the finite size effect is more prominent for larger σ_D [32].

Chapter 5

Effect of the Size Distribution on Magnetization Relaxation

Recent experiments showed that magnetic nanoparticles possess either Gaussian distributions f_G (Refs. [3, 11, 12]) or log-normal distributions f_{LN} of sizes [9, 13, 14]. For small variances, log-normal distributions look similar to Gaussian distributions. In this study, we consider only square and Gaussian distributions of D. Square distributions of D (centered at D_0 with fixed widths where the values of D are uniformly distributed in the range) are chosen for their simplicity in analysis, which provides insight into the analysis for Gaussian distributions of D. Compared to log-normal distributions, Gaussian distributions are easier to implement in KMC simulations and to find closed analytical forms. In this chapter, we discuss the effect of the particle size distribution on metastability in magnetization relaxation [32]. For simplicity, we focus henceforth on the SD regime that can be realized for $|H| < (D + 4)$ in the low-temperature limit for a given lattice size L. More specifically, we study the region I-B using the parameter values of $H = -4$ and $D = 0.25$ throughout this Chapter. As illustrated in Fig. 5.1, we first calculate energy differences between different spin configurations for several initial relaxation paths. Considering those energy differences, we conjecture energetically favorable paths for relaxation of magnetization, which are indi-

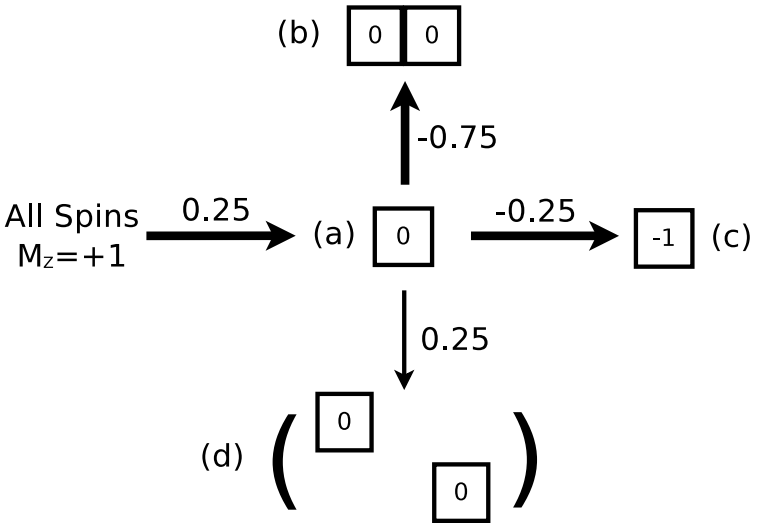

Figure 5.1: A schematic diagram of a few initial paths and corresponding spin configurations for the magnetization relaxation for the Blume-Capel model at $H = -4$ and $D = 0.25$. In the initial configuration, all sites have $M_z = +1$. A square containing a number M_0 represents a single flipped spin with $M_z = M_0$ from the initial configuration. The critical droplet is formed in the configuration (a). For the configuration (b), the two sites with $M_z = 0$ are nearest neighbors, while for the configuration (d), they are not nearest neighbors. The energy differences ΔE between two configurations are shown right next to the arrows. The bold arrows represent energetically favorable paths in the limit of $T \to 0$. Modified from Fig. 4 of Ref. [18].

cated by the bold arrows in Fig. 5.1. We find that the critical droplet consists of a single site with $M_z = 0$ [in the configuration (a) in Fig. 5.1]. The energy barrier Γ is found to equal $(4 + D - |H|)$, which corresponds to the energy difference between the initial configuration and the configuration (a).

5.1 Uniform Sizes: Constant Magnetic Anisotropy D

At the region I-B where the critical droplet is a single spin with $M_z = 0$, the exit time from the transient subspace is, using the $s = 2$ AMC method [16, 17] discussed earlier, given by

$$\langle \tau \rangle = \frac{8p_2 + p_{19}^- + p_{19}^+ + (4L^2 - 10)p_1}{8p_2 + p_{19}^- + (2L^2 - 10)p_1} \frac{1}{p_1}, \tag{5.1}$$

$$p_1 = \frac{1}{1 + e^{(4+D-|H|)1/T}}, \quad p_2 = \frac{1}{1 + e^{(3+D-|H|)1/T}}, \tag{5.2}$$

$$p_{19}^+ = \frac{1}{1 + e^{(-4-D+|H|)1/T}}, \quad p_{19}^- = \frac{1}{1 + e^{(4-D-|H|)1/T}}, \tag{5.3}$$

where p_1 is the Gaussian spin-flip probability from $M_z = 1$ to 0 when all four nearest neighbors have $M_z = 1$. Here p_2 is the spin-flip probability from $M_z = 1$ to 0 when the sum of the four nearest-neighboring moments equals $M_z = 3$. p_{19}^+ is the spin-flip probability from $M_z = 0$ to 1 when the sum of the four nearest-neighboring moments equals $M_z = 4$. Similarly, p_{19}^- is the spin-flip probability from $M_z = 0$ to -1 when the sum of the four nearest-neighboring moments equals $M_z = 4$. Let us consider $0 < D < 1/2$. For $(4 - D) < |H| < (4 + D)$, in the limit of $T \to 0$, p_1 is approximated as $\exp[-(4 + D - |H|)1/T]$, while p_2, p_{19}^+, and p_{19}^- approach unity where the approximated probabilities satisfy the detailed balance condition. Thus, in the low-temperature limit, Eq. (5.1) becomes

$$\langle \tau \rangle = A/p_1 = Ae^{\Gamma(D,H)/T} \tag{5.4}$$

$$\Gamma(D, H) = 4 + D - |H|, \tag{5.5}$$

where the prefactor A is 10/9 for $(4 - D) < |H| < (4 + D)$ and $|H| > D + 3$ (region I-B) while it is 9/8 for $(3 + D) < |H| < (4 - D)$ (region I-A). This exit time obeys the Arrhenius law where the activation energy barrier Γ depends on D and H. Equation (5.4) can be understood as follows. In the SD regime, at low temperatures, the exit time (or the lifetime of the metastable state) must be, approximately, inversely proportional to the probability of forming a critical droplet, p_{eq}. The probability p_{eq} equals p_1 when the critical droplet consists of a single spin with $M_z = 0$. Thus, $\langle \tau \rangle = A/p_{eq} = A/p_1$.

We perform KMC simulations using the n-fold way algorithm [37] for the parameter values of interest at $1/T = 41 - 90$ [Fig. 5.2(a)] for $L = 40$. At a given $1/T$, we take a thermal average over 2000 escapes. We fit the simulation data at $1/T = 55 - 90$ to a linear function, $\ln\langle\tau\rangle = \ln A + \Gamma 1/T$ (Fig. 5.2). As a result, we find that $\Gamma = 0.2497 \pm 0.0004$ and $A = 1.147 \pm 0.037$. Within the uncertainty, the simulated $\langle\tau\rangle$ agrees well with the exit time, Eq. (5.4), at $1/T \geq 55$. The simulation data below $1/T = 50$ with $L = 40$ are deviated from the linear function [Fig. 5.2(b)] because the system has not yet completely reached the SD regime. The temperature where the simulation data agree with the linear function (or the crossover between the SD and MD regimes) depends on L. The larger the lattice size is, the lower the temperature needed for the agreement, which was shown for the Ising model [16]. Comparison between our simulation data with $L = 20$ and 40 at $1/T = 40 - 50$ [Fig. 5.2(b)] corroborates this statement for the $S = 1$ Blume-Capel model.

5.2 Square Distribution of D

We consider square distributions centered at $D_0 = 0.25$ with three values of width 2ε ($\varepsilon = 0.0125, 0.025$, and 0.0375). For a distribution of D, different values of D are assigned at different sites. As a result, a rate of transition between the initial configuration and the configuration (a) differs at different sites. Note that for the constant D, in the AMC, $p_{eq} = p_1$ when $(3 + D) < |H| < (4 + D)$ (for $0 < D < 1/2$). With a distribution of D, we predict that the probability p_{eq} can be written as the summation of the product of $p_{1,i}$ and $f(D_i)$ over all sites. $p_{1,i}$ defined to be p_1 for the site i becomes $e^{-D_i/T}$ at $H = -4$ (in the limit of $T \to 0$). $f(D_i)$ is a probability density of selecting D_i from the distribution of D. After converting the summation into the integral over D, we obtain the probability p_{eq} as

$$p_{eq} = \int f(D) e^{D/T} dD. \tag{5.6}$$

For the square distributions of concern, it can be written as

$$p_{eq} = \frac{1}{2\varepsilon} \int_{D_0-\varepsilon}^{D_0+\varepsilon} e^{D/T} dD. \tag{5.7}$$

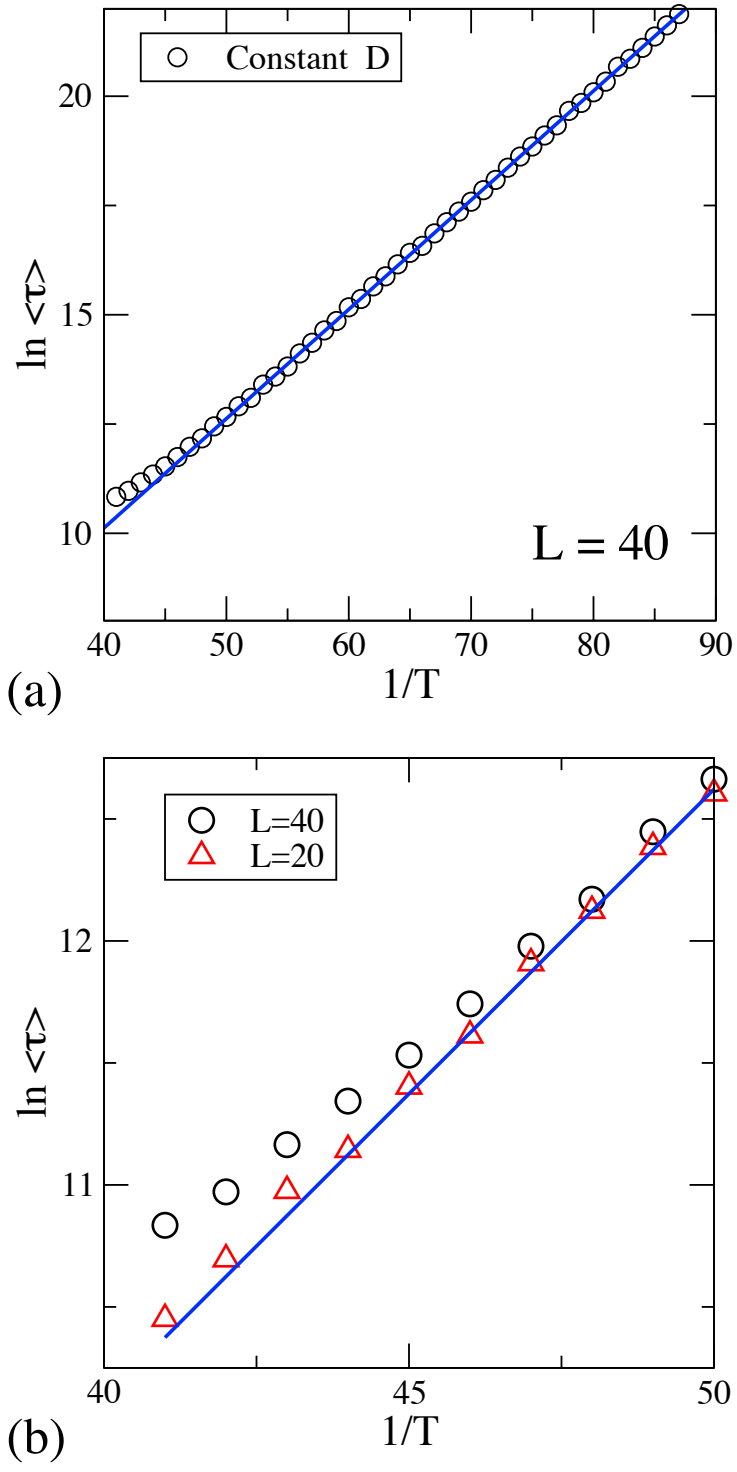

Figure 5.2: (a) The average lifetime $\langle\tau\rangle$ vs $1/T$ for the constant value of $D = 0.25$ for $L = 40$ [32]. The circles represent our simulation data, while the solid lines denote the fitting to Eq. (5.4). (b) Zoom-in of (a) at $1/T = 40 - 50$ with $L = 20$ and $L = 40$.

Finally, the average lifetime has the form

$$\langle \tau \rangle = \frac{A}{p_{eq}} = A \frac{\varepsilon/T}{\sinh \varepsilon/T} e^{D_0/T} \tag{5.8}$$

$$= \tilde{A}(T, \varepsilon) e^{\Gamma/T}, \tag{5.9}$$

where $A = 10/9$ from Sec. IV A. In the low-temperature limit, $\Gamma = D_0 - \varepsilon$ and $\tilde{A}(T, \varepsilon) = 2A\varepsilon/T$. Therefore, the energy barrier decreases linearly with increasing width, and the prefactor $\tilde{A}$ now depends on both T and the width.

We perform KMC simulations for the square distributions of D with three values of width in the temperature range of $1/T = 55 - 80$ (Fig. 5.3). For computation of $\langle \tau \rangle$ at a given T and ε, we take a thermal average over 2000 escapes and an average over 10 square distributions. The average lifetime decreases with increasing width (Fig. 5.3), as expected from Eq. (5.8). As the width increases, there are probabilities of selecting much lower values of D than D_0. The energy barrier is determined by the smallest value of D from the distributions. This lowers the energy barrier ($\Gamma = D_0 - \varepsilon$) and shortens the average lifetime. Regarding fitting of the simulation data, we use two different strategies: (i) the first strategy is to fit the data to Eq. (5.8) for D_0 and A with ε fixed, and (ii) the second method is to fit the data for A with D_0 and ε fixed. Using the first fitting method, we find that D_0 is 0.250 within the uncertainty of 0.001. The value of A bears one order of magnitude higher uncertainty (than that of Γ) and it significantly varies with the width: $A = 1.165 \pm 0.017, 1.170 \pm 0.017$, and 1.212 ± 0.018 for $\varepsilon = 0.0125, 0.025$, and 0.0375, respectively. Using the second method, we find that the value of A is much closer to the predicted value, 10/9, and that it is independent of the width (Table 5.1). The fitting using the second strategy is shown in Fig. 5.3. As shown in Fig. 5.3, the simulation data agree well with the calculated lifetimes using Eq. (5.8).

5.3 Gaussian Distribution of D

We consider Gaussian distributions of D centered at $D_0 = 0.25$ with three values of standard deviation σ_D ($\sigma_D = 0.0125, 0.025$, and 0.0375). Similarly to the square distributions of D,

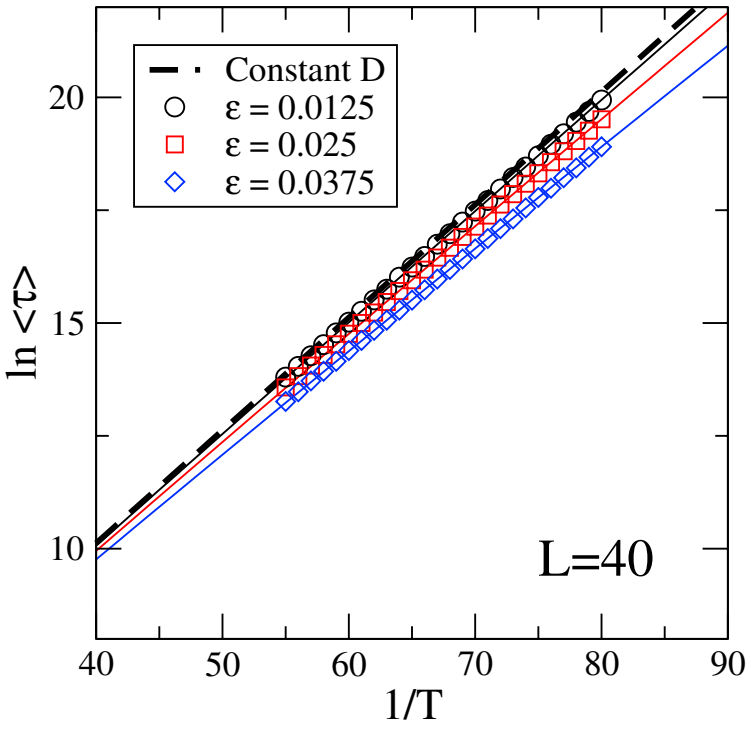

Figure 5.3: The average lifetime $\langle\tau\rangle$ vs $1/T$ for the square distributions of D centered at $D_0 = 0.25$ with three different widths of 2ε for $L = 40$ [32]. The symbols represent our simulation data, while the solid curves are obtained from the fitting (the second method) to Eq. (5.8) (Table 5.1). For comparison, the fitting curve for the constant D (Fig. 5.2) is also included.

Table 5.1: Fitting of the Monte Carlo simulation data for the square and Gaussian distributions of D with $D_0 = 0.25$ and ϵ or σ_D fixed. The fitting functions and the prefactor A are shown, where $x = 1/T$.

	Fitting function	$A(\varepsilon, \sigma_D = 0.0125)$	$A(\varepsilon, \sigma_D = 0.025)$	$A(\varepsilon, \sigma_D = 0.0375)$
Square	$A\frac{\varepsilon x}{\sinh(\varepsilon x)}e^{D_0 x}$	1.112 ± 0.002	1.117 ± 0.002	1.117 ± 0.003
Gaussian	$A\exp(D_0 x - \frac{1}{2}\sigma_D^2 x^2)$	1.118 ± 0.001	1.128 ± 0.002	1.251 ± 0.009

we calculate the exit time from the transient subspace (in the AMC) using the probability p_{eq}, Eq. (5.6), where $f(D) = f_G(D)$. The exit time or the average lifetime has the form

$$\langle \tau \rangle = A \exp\left(\frac{D_0}{T} - \frac{\sigma_D^2}{2T^2}\right) \tag{5.10}$$

$$= A \exp[\Gamma(T, D_0, \sigma_D)/T]. \tag{5.11}$$

Interestingly, in this case, the energy barrier Γ depends on T as well as D_0 and σ_D, which deviates from the Arrhenius law.

We perform KMC simulations for the Gaussian distributions of D with the three different standard deviations in the temperature range of $1/T = 55 - 81$ (Fig. 5.4). For computation of $\langle \tau \rangle$ at a given T and σ_D, we take a thermal average over 2000 escapes and an average over 100 Gaussian distributions. As expected from Eq. (5.10), the average lifetime decreases with increasing σ_D. The energy barrier decreases more rapidly with increasing σ_D than that for the square distributions (Fig. 5.3 versus Fig. 5.4). Using the similar argument from the previous section, the decrease in the barrier arises from the values of D selected from the lower end of the Gaussian distributions. For fitting of the simulation data, we use constrained fitting to Eq. (5.10) with D_0 and σ_D fixed, where A is the only free parameter. The result is listed in Table 5.1. The value of A is close to 10/9, even though it varies slightly with the value of σ_D. Its uncertainty increases with increasing σ_D. As shown in Fig. 5.4, the simulated data agree well with the calculated lifetimes (the fitting curves) for the distributions with small standard deviations such as $\sigma_D = 0.0125$ and 0.025 ($\sigma_D/D_0 = 5\%$ and 10%). However, in the case of $\sigma_D = 0.0375$ ($\sigma_D/D_0 = 15\%$), we observe noticeable deviations of the simulation data from the fitting curve as temperature decreases (especially near $1/T = 80$ in Fig. 5.4). For clarification of these deviations, we plot differences between the simulated lifetimes and the fitting curves as a function of T for the constant value of D and the Gaussian distribution with $\sigma_D = 0.0375$ (Fig. 5.5). In the range of the temperature where the fitting is done, $1/T = 55 - 80$, the difference is almost zero for the constant D, while it starts to increase above $1/T = 70$ and reaches approximately 0.1 at $1/T = 80$ for the Gaussian distribution. This is the reason that the value of A for $\sigma_D = 0.0375$ differs somewhat from that for

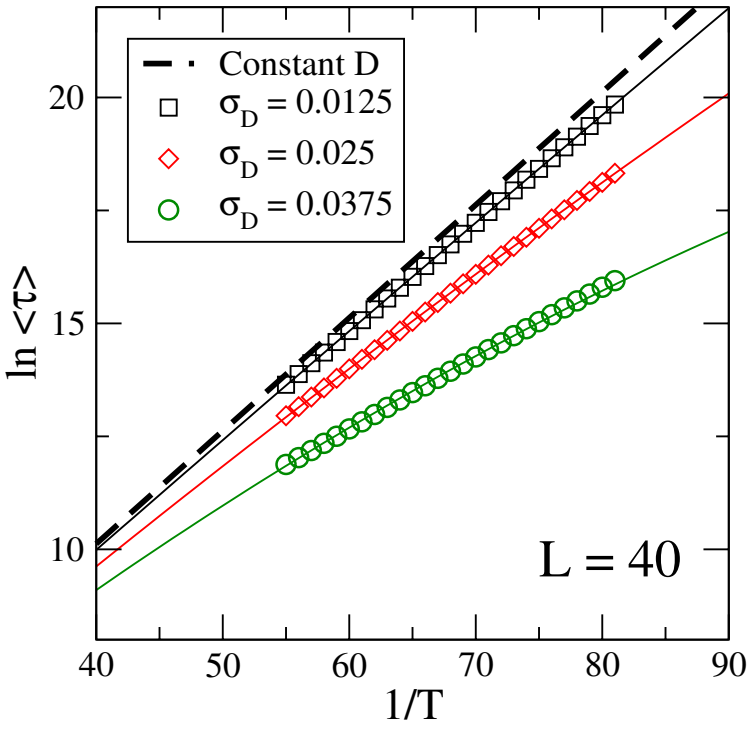

Figure 5.4: The average lifetime $\langle\tau\rangle$vs $1/T$ for the Gaussian distributions of D centered at D_0 with the three standard deviations σ_D for $L = 40$ [32]. The symbols show our simulation data and the solid curves are obtained from the fitting to Eq. (5.10) (Table 5.1). The fitting curve for the constant D is included.

$\sigma_D = 0.0125$ and 0.025.

5.4 Discussions About Finite Size Effects

Let us now discuss what causes the discrepancy between the simulated and calculated lifetime for $\sigma_D = 0.0375$ at low temperatures. One possibility is a finite-size effect. For a finite lattice, we can write Eq. (5.6) as $p_{eq} = (\sum_{i=1}^{N} e^{-D_i/T})/N$, where D_i is taken from the Gaussian distribution with $\sigma_D = 0.0375$. Using $\langle\tau\rangle = A/p_{eq}$, the average lifetime for the finite lattice

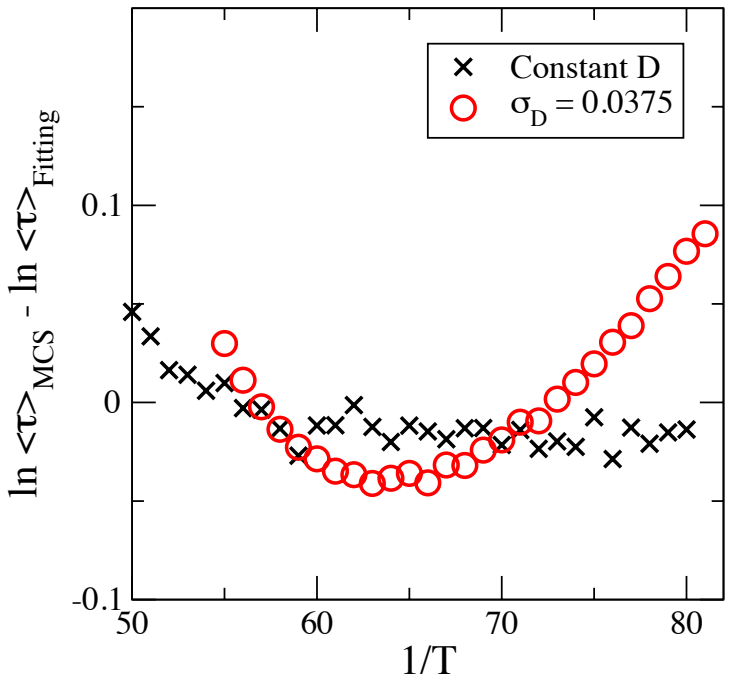

Figure 5.5: The differences between the lifetimes from the simulations and the fitting for the constant D and the Gaussian distribution with $\sigma_D = 0.0375$ for $L = 40$ [32].

becomes

$$\langle \tau \rangle = A \left(\frac{1}{N} \sum_{i=1}^{N} e^{-D_i/T} \right)^{-1}, \tag{5.12}$$

where $A = 10/9$. We generate the lifetime as a function of T using both Eqs. (5.10) and (5.12) for two lattice sizes $L = 40$ and 400, as shown in Fig. 5.6. For proper comparison, when Eq. (5.12) is used, an average of 100 Gaussian distributions are taken for $L = 40$ and 400 (Fig. 5.6). As shown in Fig. 5.6(a), for $L = 40$, in the case of $\sigma_D = 0.0125$ and 0.025, the symbols agree well with the curves. This implies that there is no finite-size effect for small values of σ_D for $L = 40$. However, for $L = 40$ and $\sigma_D = 0.0375$, the deviations between the curve and the symbols start to appear near $1/T = 65$ and they become more significant at lower temperatures [marked by the bold arrow in Fig. 5.6(a)]. No such deviations are found for $L = 400$ and $\sigma_D = 0.0375$, as shown in Fig. 5.6(b). This result corroborates that the deviations observed in Fig. 5.5 are caused by the finite-size effect. It also suggests that the finite-size effect must be considered in the analysis when the distributions are wide.

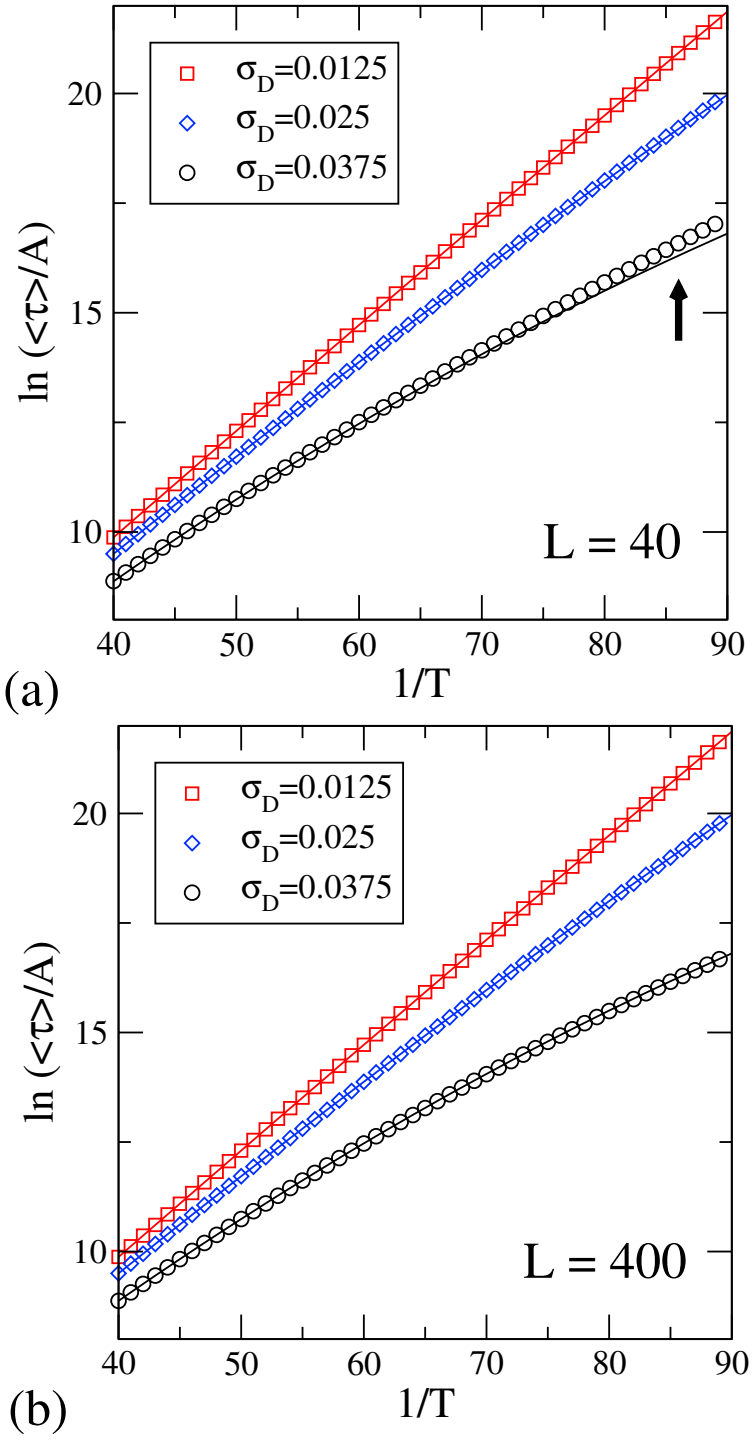

Figure 5.6: The calculated values of $\ln(\langle\tau\rangle/A)$ vs $1/T$ using Eq. (5.10) (curves) and Eq. (5.12) (symbols) for (a) $L = 40$ and (b) $L = 400$. For the curves, an average of 100 distributions is taken [32]. The bold arrow in (a) emphasizes the region where the deviations between the symbols and the curve are substantial.

Chapter 6

Different Dynamics with Constant Magnetic Anisotropy

In this chapter, we present analytic and simulated average lifetimes $\langle\tau\rangle$ in the regions I-A and II and at the boundary for constant D (specifically the parameter values marked as `b-d` in Fig. 3.6), using Glauber dynamics. Then similar analysis is carried out for the phonon-assisted dynamics [38]. In our KMCS, 2000 escapes are simulated for a thermal average at a given value of β.

The highlights of our results in this section are as follows. The energy barrier Γ in $\langle\tau\rangle$ increases with increasing D for a fixed $|H|$. The increase in the region II is greater than in the region I-A for both dynamics. At the boundary, the barrier Γ for the phonon-assisted dynamics greatly increases compared to the Glauber dynamics due to forbidden transitions under the phonon-assisted dynamics. The prefactor A in $\langle\tau\rangle$ for the Glauber dynamics is constant for a given region, but it is different at the boundary. The prefactor A for the phonon-assisted dynamics, however, depends on D and $|H|$ even for a given region.

To calculate the analytic form of the lifetime, we use the $s = 3$ AMC method with the following three transient states (and five absorbing states): (i) the initial state, (ii) the state

of a single site with $M_z = 0$ from the initial state (N possible configurations), and (iii) the state of two nearest-neighbor sites with each spin $M_z = 0$ from the initial state ($2N$ possible configurations). The exit time from the transient subspace or $\langle\tau\rangle$ as a function of $|H|$, D, T, and N is given by

$$\begin{aligned}
\langle\tau\rangle &= \frac{F_1(p_1) + F_2(p_1) + F_0 + p_{19}^+(6p_2 + p_{20}^+ + p_{20}^-)}{p_1[F_3(p_1) + F_4(p_1) + F_0]}, \qquad (6.1)\\
F_0 &= 48p_2^2 + p_{19}^-(p_{20}^+ + p_{20}^-) + p_2(6p_{19}^- + 8p_{20}^-)\\
F_1(p_1) &= p_1^2(80 - 42N + 4N^2),\\
F_2(p_1) &= p_1[(40N - 124)p_2 + (N-8)(p_{19}^+ + p_{19}^-) + (4N-10)(p_{20}^+ + p_{20}^-)],\\
F_3(p_1) &= 2p_1^2(40 - 13N + N^2),\\
F_4(p_1) &= p_1[(20N - 124)p_2 + (N-8)p_{19}^- + (2N-10)(p_{20}^+ + p_{20}^-)],
\end{aligned}$$

where p_i is a spin-flip probability in spin class i listed in Table 4.1. Equation (6.1) is valid in the regions I-A and II and at the region boundary for the Glauber dynamics and in the regions I-A and II for the phonon-assisted dynamics, because the critical droplets for the regions I-A and II are included in the transient subspace for both dynamics. However, Eq. (6.1) is *not* valid at the boundary for the phonon-assisted dynamics. Further discussion follows.

6.1 Glauber Transition Rate

For the Glauber transition rate, the p_i's in the Eq. (6.1) are written as

$$\begin{aligned}
p_1 &= \frac{1}{1 + e^{\beta(4+D-|H|)}}, \quad p_2 = \frac{1}{1 + e^{\beta(3+D-|H|)}}, \qquad (6.2)\\
p_{19}^+ &= \frac{1}{1 + e^{\beta(-4-D+|H|)}}, \quad p_{20}^+ = \frac{1}{1 + e^{\beta(-3-D+|H|)}}, \qquad (6.3)\\
p_{19}^- &= \frac{1}{1 + e^{\beta(4-D-|H|)}}, \quad p_{20}^- = \frac{1}{1 + e^{\beta(3-D-|H|)}}. \qquad (6.4)
\end{aligned}$$

Let us first present our result for the region I-A ($3 + D < |H| < 4 - D$ and $D > 0$). In the $T \to 0$ limit, p_1 becomes $\exp[-\beta(4 + D - |H|)]$, while p_2, p_{19}^+, and p_{20}^- approximate unity. In

addition, p_{19}^- and p_{20}^+ approximate $\exp[-\beta(4-D-|H|)]$ and $\exp[\beta(3+D-|H|)]$, respectively, and so they vanish in the zero-temperature limit. Thus, the average lifetime, Eq. (6.1), in the zero-temperature limit becomes

$$\langle\tau\rangle = \frac{8p_2 + p_{19}^+}{8p_1p_2} = \frac{A}{p_1} = Ae^{\beta\Gamma(D,H)}, \tag{6.5}$$

where $\Gamma(D,H) = 4 + D - |H|$ and $A = 9/8$ is independent of D and $|H|$ in the region I-A. This agrees with the result obtained from the $s = 2$ AMC method [32]. Simulations are performed using the $s = 2$ MCAMC for $L = 40$, $D = 0.125$, and $|H| = 3.25$ in the range of $\beta = 50 - 690$ (Fig. 6.1). We use two methods to fit the KMCS data to Eq. (6.5): (i) to use A and Γ as fitting parameters, and (ii) to use only A as a fitting parameter with Γ fixed as the value from the $s = 3$ AMC method ($\Gamma = 0.875$). The first method provides that $\Gamma = 0.8750 \pm 1.53 \times 10^{-5}$ and $A = 1.1246 \pm 0.0071$, while the second method gives $A = 1.1221 \pm 0.0032$. The fitted values agree with the analytic values, $\Gamma = 0.875$ and $A = 1.125$, within the uncertainties.

We now present our result for the region II ($3-D < |H| < 3+D$ and $D < 0.5$). In the $T \to 0$ limit, p_1 and p_2 become $\exp[-\beta(4 + D - |H|)]$ and $\exp[-\beta(3 + D - |H|)]$, respectively. p_{19}^+, p_{20}^+, and p_{20}^- approximate to unity. p_{19}^- approximates $\exp[-\beta(4 - D - |H|)]$, which vanishes as $T \to 0$. The lifetime, Eq. (6.1), in the zero-temperature limit becomes

$$\langle\tau\rangle = \frac{p_{19}^+(p_{20}^+ + p_{20}^-)}{8p_1p_2p_{20}^-} = \frac{A}{p_1p_2} = Ae^{\beta\Gamma(D,H)}, \tag{6.6}$$

where $\Gamma(D,H) = 7 + 2D - 2|H|$ and $A = 1/4$. The barrier Γ increases with increasing D more rapidly than in the region I-A for a given value of $|H|$. We perform KMCS at $|H| = 3.25$ and $D = 0.375$ in the range of $\beta = 50 - 560$ (Fig. 6.1). Fitting of our simulation data to Eq. (6.6) shows that $A = 0.2486 \pm 0.0015$ and $\Gamma = 1.2500 \pm 1.81 \times 10^{-5}$ from the first method, and that $A = 0.2497 \pm 0.0007$ from the second method. These values agree with those from the $s = 3$ AMC method ($\Gamma = 1.25$, $A = 0.25$) within the uncertainties.

Finally, we show our result for the boundary between the regions I-A and II ($|H| = 3 + D$ and $0 < D < 0.5$). In the $T \to 0$ limit, $p_1 \to \exp[-\beta(4 + D - |H|)]$, $p_{19}^+, p_{20}^- \to 1$,

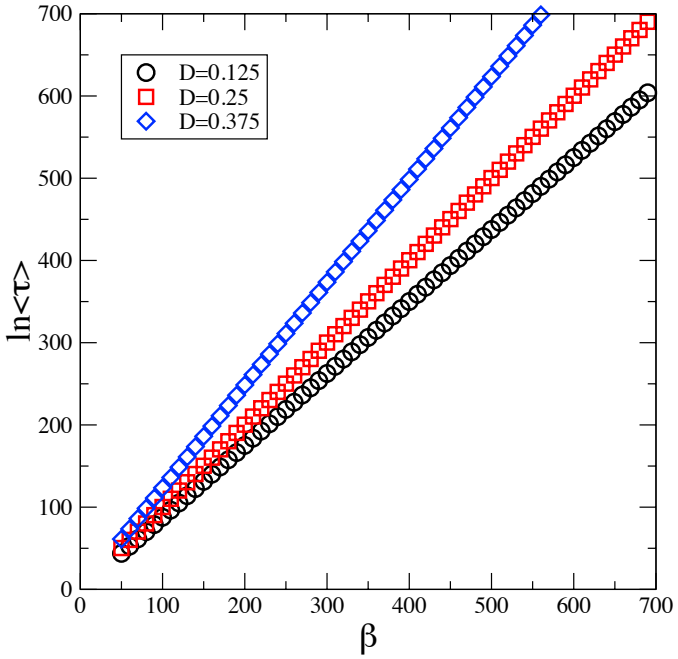

Figure 6.1: The simulated $\langle\tau\rangle$ vs β using the Glauber dynamics for three constant values of D at $|H| = 3.25$ for $L = 40$ [38].

Table 6.1: Fitting of our KMCS data using the Glauber dynamics for constant D at $|H| = 3.25$ [38]. In the first method Γ and A are parameters, and in the second method only A is fitted.

	Region I-A ($D = 0.125$)	Boundary ($D = 0.25$)	Region II ($D = 0.375$)
First method	$\Gamma = 0.8750 \pm 1.53 \times 10^{-5}$ $A = 1.1246 \pm 0.0071$	$\Gamma = 1.0000 \pm 1.73 \times 10^{-5}$ $A = 1.2885 \pm 0.0092$	$\Gamma = 1.2500 \pm 1.81 \times 10^{-5}$ $A = 0.2486 \pm 0.0015$
Second method	$\Gamma = 0.875$ (fixed) $A = 1.1221 \pm 0.0032$	$\Gamma = 1$ (fixed) $A = 1.2873 \pm 0.0041$	$\Gamma = 1.25$ (fixed) $A = 0.2497 \pm 0.0007$
AMC method	$\Gamma = 0.875$ $A = 1.125$	$\Gamma = 1$ $A = 1.28125$	$\Gamma = 1.25$ $A = 0.25$

$p_{19}^- \to \exp[-\beta(4 - D - |H|)]$, and p_2, $p_{20}^+ \to 1/2$. At the boundary, the lifetime is

$$\langle \tau \rangle = \frac{(8p_2 + p_{19}^+)(6p_2 + p_{20}^-) + p_{19}^+ p_{20}^+}{8p_1 p_2 (6p_2 + p_{20}^-)} = Ae^{\beta\Gamma(D,H)}, \tag{6.7}$$

where $\Gamma = 1$ and $A = 41/32$. In this case, the barrier Γ does not depend on D or $|H|$. The prefactor A differs from that for the region I-A or II, because in the zero-temperature limit, p_2 and p_{20}^+ differ from those for the region I-A or II. Fitting of our simulation data in the range of $\beta = 50 - 690$ (Fig. 6.1) provides that $\Gamma = 1.0000 \pm 1.73 \times 10^{-5}$ and $A = 1.2885 \pm 0.0092$ from the first method, and that $A = 1.2873 \pm 0.0041$ from the second method. These values agree with those from the AMC method within the uncertainties. See Table 6.1 for the summary.

6.2 Phonon-Assisted Transition Rate

For the phonon-assisted dynamics, the p_i's in Eq. (6.1) are given as

$$p_1 = \frac{(4+D-|H|)^3}{e^{\beta(4+D-|H|)}-1}, \quad p_2 = \frac{(3+D-|H|)^3}{e^{\beta(3+D-|H|)}-1}, \tag{6.8}$$

$$p_{19}^{+} = \frac{(-4-D+|H|)^3}{e^{\beta(-4-D+|H|)}-1}, \quad p_{20}^{+} = \frac{(-3-D+|H|)^3}{e^{\beta(-3-D+|H|)}-1}, \tag{6.9}$$

$$p_{19}^{-} = \frac{(4-D-|H|)^3}{e^{\beta(4-D-|H|)}-1}, \quad p_{20}^{-} = \frac{(3-D-|H|)^3}{e^{\beta(3-D-|H|)}-1}. \tag{6.10}$$

In region I in the $T \to 0$ limit, p_1 approaches to $(4+D-|H|)^3 \exp[-\beta(4+D-|H|)]$. p_2, p_{19}^{+}, and p_{20}^{-} approach to $|3+D-|H||^3, |-4-D+|H||^3$, and $|3-D-|H||^3$ respectively, and p_{20}^{+} and p_{19}^{-} approach to zero. Hence, Eq. (6.1) in the low-temperature limit becomes

$$\langle \tau \rangle = \frac{8p_2 + p_{19}^{+}}{8p_1 p_2} = Ae^{\Gamma\beta} \tag{6.11}$$

$$A = \frac{8|3+D-|H||^3 + |4+D-|H|^3}{8|3+D-|H||^3 |4+D-|H|^3}, \tag{6.12}$$

$$\Gamma = 4+D-|H|. \tag{6.13}$$

While the expression for the Γ is identical to the case with the Glauber transition rate, prefactor A takes a very different form because the probabilities p_i's take more complex forms. For $|H| = 3.25$ and $D = 0.125$, Eq. (6.11) gives rise to $\Gamma = 0.875$ and $A = 65.4927$. The KMC simulations are performed at $\beta = 50 - 690$ (Fig. 6.2). Fitting our simulation data, we find that $\Gamma = 0.8750 \pm 1.628 \times 10^{-5}$ and $A = 65.0899 \pm 0.4396$ with the first fitting method. Further more, we find that $A = 65.6062 \pm 0.2015$ using the second fitting method.

We now examine analytic and simulated lifetimes for the region II. In the limit of $T \to 0$, p_1 approximates $(4+D-|H|)^3 \exp[-\beta(4+D-|H|)]$, and p_2 approximates $(3+D-|H|)^3 \exp[-\beta(3+D-|H|)]$. p_{19}^{-} approximates zero, and p_{19}^{+}, p_{20}^{+}, and p_{20}^{-} approximate $(4+D-|H|)^3$, $(3+D-|H|)^3$, and $(-3+D+|H|)^3$, respectively. Thus, the prefactor and the barrier in Eq. (6.1) or Eq. (6.6) are given by

$$A = \frac{(3+D-|H|)^3 + (-3+D+|H|)^3}{8(3+D-|H|)^3(-3+D+|H|)^3}, \quad \Gamma = 7+2D-2|H|, \tag{6.14}$$

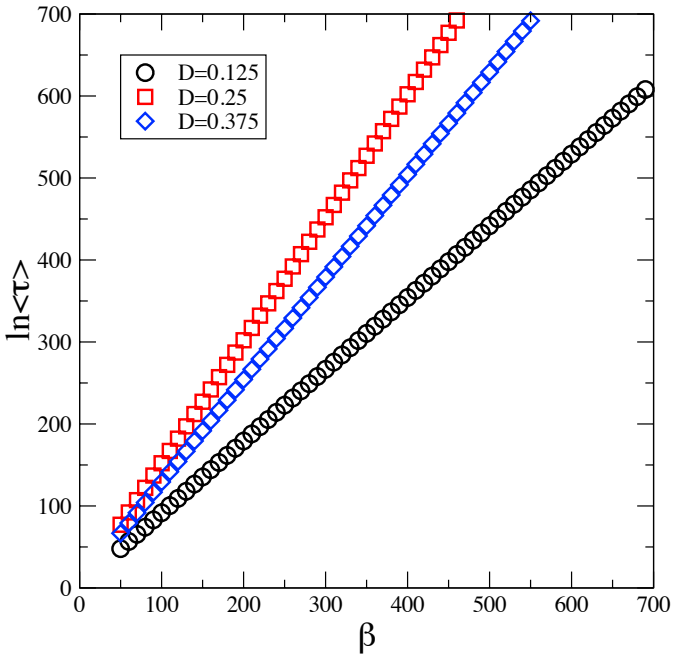

Figure 6.2: The simulated lifetime $\langle\tau\rangle$ vs β for the three different constant values of D at $|H| = 3.25$ for $L = 40$, using the $3d$ phonon-assisted transition rate [38].

whereas $|H|$ becomes close to $3-D$ or $3+D$ (boundaries of the region II), A greatly increases. For $|H| = 3.25$ and $D = 0.375$, Eq. (6.14) reveals that $\Gamma = 1.25$ and $A = 64.512$. Fitting our data in the range of $\beta = 50 - 550$ (Fig. 6.2) shows that $\Gamma = 1.2500 \pm 2.01 \times 10^{-5}$ and $A = 64.2807 \pm 0.4325$ from the first method, and that $A = 64.4455 \pm 0.1894$ from the second method.

Lastly, we discuss the average lifetime at the boundary. In this case, interestingly, the transitions marked as (a) and (b) in Fig. 6.3 are forbidden ($p_2 = 0$, $p_{20}^{+} = 0$) because the states involved with the transitions are degenerate. Thus, at the boundary, the critical droplet is now a single site with spin projection $M_z = -1$. This change necessitates usage of a different set of transient states in the $s = 3$ AMC method. The new set of three transient states are the first two transient states (i) and (ii) discussed earlier and a state of a single site with spin projection $M_z = -1$ from the initial state (N possible configurations). Using this new set in the $s = 3$ AMC method, we find the average lifetime as a function of D, $|H|$, T, and N, as follows.

$$\begin{aligned}
\langle \tau \rangle &= \frac{G_1(p_1) + G_2(p_1) + G_0 + p_{19}^{+}(4p_3 + p_{10})}{p_1(G_3(p_1) + G_0)} \\
G_0 &= 4\{2p_{10}p_2 + (8p_2 + p_{19}^{-})p_3\} \\
G_1(p_1) &= p_1^2(50 - 30N + 4N^2) \\
G_2(p_1) &= p_1[(4N - 10)p_{10} + (N - 5)(8p_2 + p_{19}^{+}) + (2N - 5)(8p_3 + p_{19}^{-})] \\
G_3(p_1) &= 2p_1^2(N - 5)^2 + p_1(N - 5)(8p_2 + 8p_3 + 2p_{10} + p_{19}^{-}),
\end{aligned} \tag{6.15}$$

where p_3 and p_{10} are given by

$$p_3 = \frac{(2 + D - |H|)^3}{1 - e^{-\beta(2+D-|H|)}}, \quad p_{10} = \frac{(-4 + D + |H|)^3}{1 - e^{-\beta(-4+D+|H|)}}. \tag{6.16}$$

In the zero-temperature limit, p_1 and p_{19}^{-} are approximately $(4 + D - |H|)^3 \exp[-\beta(4 + D - |H|)]$ and $(4 - D - |H|)^3 \exp[-\beta(4 - D - |H|)]$, respectively. p_3, p_{10}, and p_{19}^{+} are close to $(-2 - D + |H|)^3$, $(4 - D - |H|)^3$, and $(4 + D - |H|)^3$, respectively. Note that $p_2 \to 0$ and

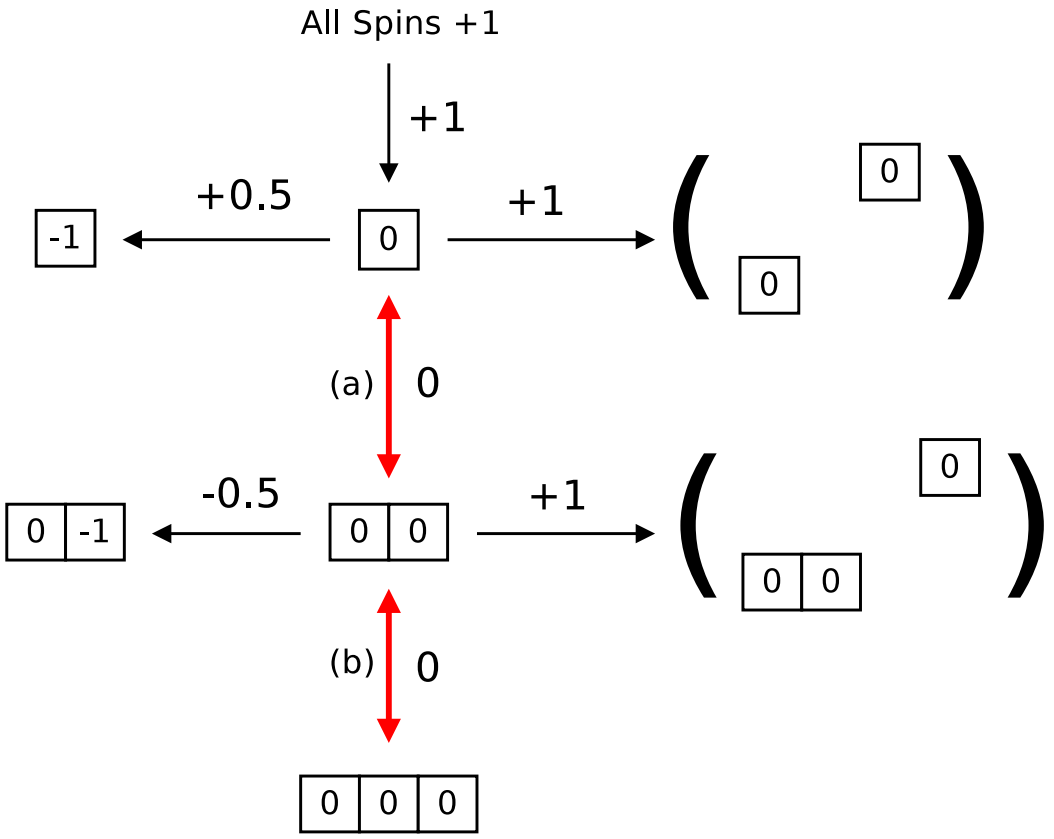

Figure 6.3: Schematic diagram of relaxation pathways at the region boundary. Each spin configuration shows only flipped spin projections from the initial state. The rightmost upper configuration indicates a state of two non-nearest-neighbor spin projections with each $M_z = 0$. The transitions (a) and (b) are not permitted under the phonon-assisted dynamics. The numbers right next to or above the arrows represent ΔE between the states for $|H| = 3.25$ and $D = 0.25$.

Table 6.2: Fitting of our KMCS data using the phonon-assisted dynamics for constant D at $|H| = 3.25$ [38].

	Region I-A ($D = 0.125$)	Boundary ($D = 0.25$)	Region II ($D = 0.375$)
First method	$\Gamma = 0.8750 \pm 1.63 \times 10^{-5}$ $A = 65.0899 \pm 0.4396$	$\Gamma = 1.5000 \pm 2.74 \times 10^{-5}$ $A = 8.2407 \pm 0.0682$	$\Gamma = 1.2500 \pm 2.01 \times 10^{-5}$ $A = 64.2807 \pm 0.4325$
Second method	$\Gamma = 0.875$ (fixed) $A = 65.6062 \pm 0.2015$	$\Gamma = 1.5$ (fixed) $A = 8.2400 \pm 0.0271$	$\Gamma = 1.25$ (fixed) $A = 64.4455 \pm 0.1894$
AMC method	$\Gamma = 0.875$ $A = 65.4927$	$\Gamma = 1.5$ $A = 8.25$	$\Gamma = 1.25$ $A = 64.512$

$p_{20}^{+} \to 0$ as $T \to 0$. Then the lifetime, Eq. (6.15), in the zero-temperature limit becomes

$$\langle \tau \rangle = \frac{p_{19}^{+}(4p_3 + p_{10})}{4p_1 p_3 p_{19}^{-}} = Ae^{\beta\Gamma} \tag{6.17}$$

$$A = \frac{4(-2 - D + |H|)^3 + (4 - D - |H|)^3}{4(-2 - D + |H|)^3(4 - D - |H|)^3}, \quad \Gamma = 8 - 2|H|. \tag{6.18}$$

Fitting of our KMCS data for $|H| = 3.25$ and $D = 0.25$ in the range of $\beta = 50 - 460$ (Fig. 6.2), shows that $\Gamma = 1.5000 \pm 2.74 \times 10^{-5}$ and $A = 8.2407 \pm 0.0682$ from the first method, and that $A = 8.2400 \pm 0.0271$ from the second method. The AMC method gives rise to $\Gamma = 1.5$ and $A = 8.25$. The simulated and analytic results agree within the uncertainties. For the summary, see Table 6.2. At the boundary, the energy barrier for the phonon-assisted dynamics is much higher than that for the Glauber dynamics, due to the forbidden transitions. The similar increase of the barrier for the phonon-assisted dynamics (due to forbidden transitions) was discussed for the boundary between the region I-C and the region III, such as $|H| = 4 - D$ $(0.5 < D < 1)$ in Ref. [18].

Chapter 7

Different Dynamics and Distributions of Magnetic Anisotropy

We consider Gaussian distributions of D centered at three values of D_0 (0.125, 0.25, 0.375 shown in Fig. 3.6) with two values of standard deviation $\sigma_D = 0.0125$ and 0.025. To generate random numbers with Gaussian distributions, the Box-Muller transformation [36] is used. At a given β and σ_D, 2000 escapes are simulated for a thermal average, and 10 Gaussian distributions are generated for an average over distribution. The same sets of distributions are used for our studies in the regions I-A and II and at the boundary for both the Glauber and phonon-assisted dynamics.

We first discuss our results for the Glauber dynamics and compare them with those for constant D. Then we similarly analyze our data for the phonon-assisted dynamics [38]. The highlights of our results are as follows. For both dynamics, compared to the case for constant D, the average lifetime decreases with Gaussian distributions of D in the two regions and at the boundary, because the barrier Γ decreases with increasing σ_D for a fixed value of β. For a given β and σ_D, both dynamics show that the decrease of the barrier or the lifetime is more apparent in the region II than in the region I-A. At the boundary, with distributions of D, the phonon-assisted dynamics now finds lower-energy relaxation pathways so that the

lifetime decreases about ten orders of magnitude at low temperatures compared to that for constant D (a much greater decrease than for the Glauber dynamics). For the Glauber dynamics, the prefactor A does not change with Gaussian distributions of D, compared to that for constant D. However, for the phonon-assisted dynamics, the prefactor A depends on even σ_D, and it significantly decreases compared to that for constant D except for the boundary. The decrease is more prominent in the region II than in the region I-A. For the phonon-assisted dynamics, at the boundary, the prefactor A greatly increases compared to that for constant D.

7.1 Glauber Transition Rate

We present our result for the region I-A. To find an analytic form of $\langle\tau\rangle$ with a distribution of D, we first take the zero-temperature limit of the spin-flip probability p_1 in Eq. (6.2), and then compute the average of the probability over Gaussian distribution of D, $f(D)$, such as $p_1 = \int f(D)\exp[-\beta(4 + D - |H|)]dD$. Applying this average to Eq. (6.5), we find the average lifetime as follows.

$$\langle\tau\rangle = A\exp[\beta\Gamma(\beta, H, D_0, \sigma_D)], \quad \Gamma(\beta, H, D_0, \sigma_D) = \Gamma_0(H, D_0) - \frac{\beta{\sigma_D}^2}{2}, \tag{7.1}$$

where $\Gamma_0(H, D_0) = 4 + D_0 - |H|$ and $A = 9/8$. The prefactor A is not affected by $f(D)$. However, due to the correction term in Γ, $-\beta\sigma_D^2/2$, the energy barrier Γ decreases with the distribution of D. We perform KMCS in the range of $\beta = 50 - 100$ with $D_0 = 0.125$ at $|H| = 3.25$ (Fig. 7.1), and fit the data to Eq. (7.1) with fitting parameters Γ_0 and A with σ_D fixed (Table 7.1). For $\sigma_D = 0.0125$, the fitted values of Γ_0 and A agree with Eq. (7.1) within σ_D. For $\sigma_D = 0.025$, the agreement between the fitting and the AMC result is not as good as the case of $\sigma_D = 0.0125$ (still agreement within $2\sigma_D$). This is because the finite size effect is more pronounced for larger σ_D [32].

We now present our result for the region II. A spin flip at site i represented by p_1 is independent of a spin flip at site j associated with p_2. Thus, as $T \to 0$, similarly to the case of

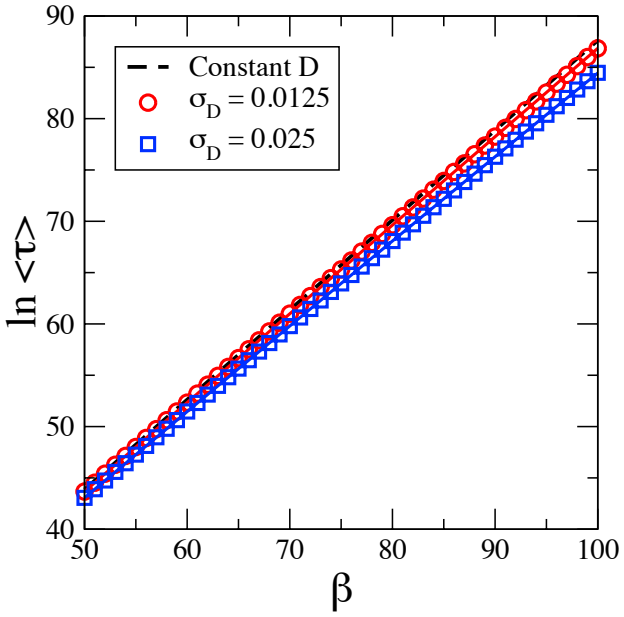

Figure 7.1: The simulated $\langle\tau\rangle$ vs β using the Glauber dynamics for the Gaussian distributions of D centered at $D_0 = 0.125$ (region I-A) with $\sigma_D = 0.0125, 0.025$ for $L = 40$ [38]. The symbols indicate our data and the solid curves are from the fitting. The lifetime for constant D is included.

the region I-A, we can rewrite $p_1 p_2$ as

$$p_1 p_2 = \int_{-\infty}^{+\infty} f(D) e^{-\beta(4+D-|H|)}\, dD \int_{-\infty}^{+\infty} f(D') e^{-\beta(3+D'-|H|)}\, dD' \tag{7.2}$$

$$= \exp\left(-\beta\Gamma_0 + \beta^2\sigma_D^2\right). \tag{7.3}$$

Hence, using Eq. (6.6), the lifetime is given by

$$\langle\tau\rangle = A\exp[\beta\Gamma(\beta, H, D_0, \sigma_D)], \quad \Gamma(\beta, H, D_0, \sigma_D) = \Gamma_0(H, D_0) - \beta{\sigma_D}^2, \tag{7.4}$$

where $\Gamma_0(H, D_0) = 7 + 2D_0 - 2|H|$ and $A = 1/4$. Note that the lifetime $\langle\tau\rangle$ or the barrier Γ decreases further compared to that for constant D in the region II than in the region I-A for a given σ_D and β. We fit our KMCS data for $D_0 = 0.375$ at $|H| = 3.25$ and $\beta = 50 - 78$ (Fig. 7.2(b)) to Eq. (7.4) with σ_D fixed. We find that $\Gamma_0 = 1.2503 \pm 1.33 \times 10^{-4}$ and $A = 0.2490 \pm 0.0021$ for $\sigma_D = 0.0125$, and that $\Gamma_0 = 1.2513 \pm 2.92 \times 10^{-4}$ and $A = 0.2300 \pm 0.0043$ for $\sigma_D = 0.025$. For $\sigma_D = 0.0125$, the fitted values are in good agreement with those using the AMC method, while for $\sigma_D = 0.025$, there is discrepancy between the fitted values and the AMC result due to the finite size effect. The discrepancy for $\sigma_D = 0.025$ in this region is greater than that in the region I-A, because the finite size effect is enhanced in this region due to the two integrals in Eq. (7.2) instead of one integral used in the region I-A. To see the pronounced finite size effect, we also fit our KMCS data at $\beta = 50 - 100$ (Fig. 7.2(a)) with Eq. (7.4). We find that $\Gamma_0 = 1.25022 \pm 6.51 \times 10^{-5}$ and $A = 0.24985 \pm 0.00124$ for $\sigma_D = 0.0125$, and $\Gamma_0 = 1.2563 \pm 0.00047$ and $A = 0.16711 \pm 0.00598$ for $\sigma_D = 0.025$ (Table 7.2). The agreement is not as good as the fitting at $\beta = 50 - 78$ since the finite size effect increases as β increases.

Note that we converted the summations into a multiplication of integrals in Eq. (7.2). This is possible because the values of D's are distributed randomly over the lattice. In case of randomly distributed D, there is no correlation among a given site and its nearest-neighbor sites (Fig. 7.3(a)), and hence we separated the integrals in the statistical limit. On the other hand, if the parameter Ds are sorted according to the value as shown in Fig. 7.3(b), we must consider the nearest-neighbor dependencies and the integration becomes more complex.

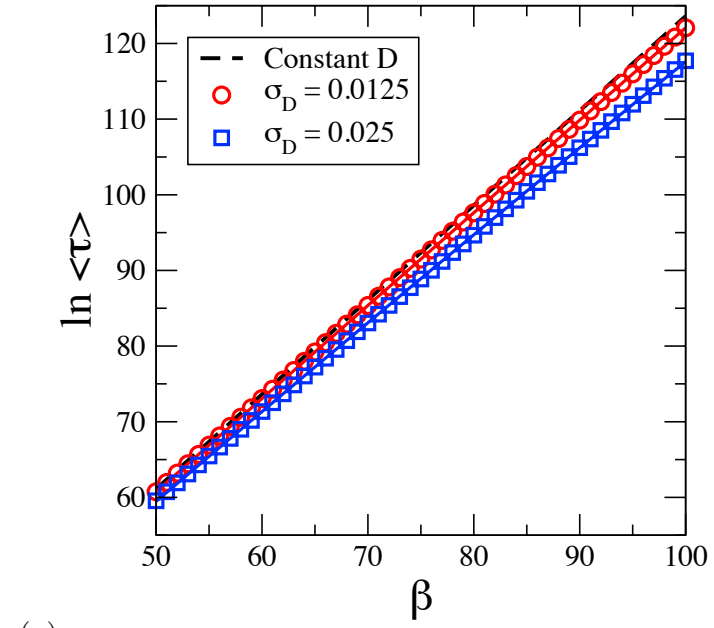

(a)

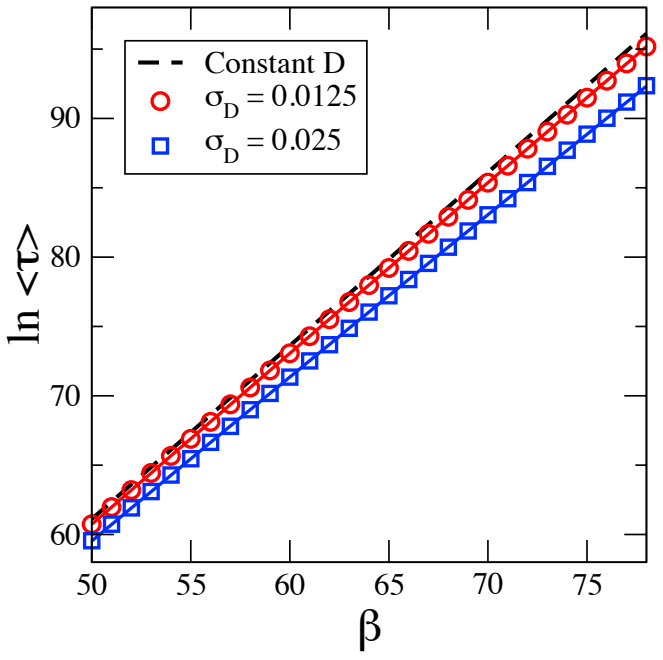

(b)

Figure 7.2: (a) The simulated $\langle\tau\rangle$ vs β using the Glauber dynamics for the distributions of D centered at $D_0 = 0.375$ (region II) with $\sigma_D = 0.0125, 0.025$ for $L = 40$. The notations are the same as those in Fig. 7.1. (b) Zoom-in of (a) at $\beta = 50 - 75$ [38].

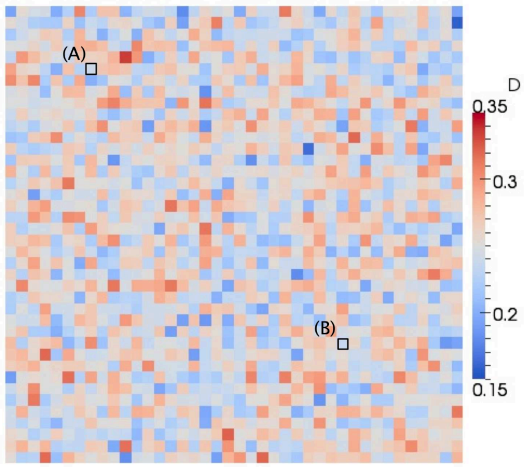

(a)

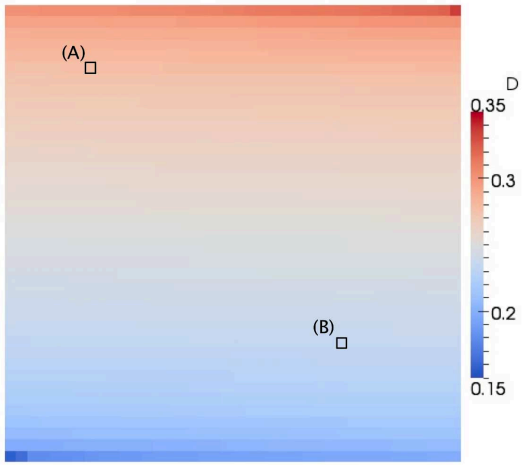

(b)

Figure 7.3: (a) The anisotropy parameter of Ds distributed randomly over lattice. In this case, the nearest-neighbor sites of a given site have random values of D. (b) The distribution of D is sorted according to the values of Ds. In this case, there is a correlation among a site and its nearest-neighbor sites.

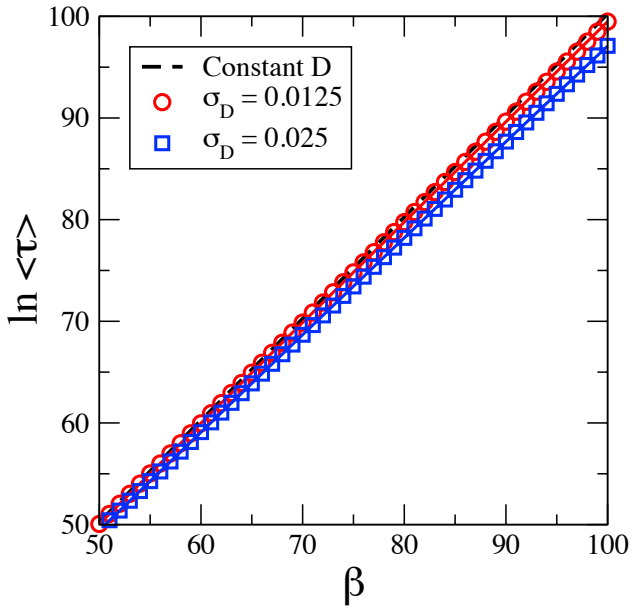

Figure 7.4: The simulated $\langle\tau\rangle$ vs β using the Glauber dynamics for the distributions of D centered at $D_0 = 0.25$ (at the region boundary) with $\sigma_D = 0.0125, 0.025$ for $L = 40$ [38]. The notations are the same as those in Fig. 7.1.

Finally, we show our result for the boundary. In the $T \to 0$ limit, and $p_2 \to \int_{-\infty}^{+\infty} f(D)\Theta(D - |H| + 3))dD$ and $p_{20}^{+} \to \int_{-\infty}^{+\infty} f(D)\Theta(|H| - 3 - D)dD$, where $\Theta(x)$ is a Heaviside function (the Glauber transition rate in the $T \to 0$ limit as shown in Fig. 7.5). Applying them and p_1 discussed earlier to Eq. (6.7), we find the lifetime as

$$\langle\tau\rangle = A \exp\left[\beta\Gamma(\beta, \sigma_D)\right], \quad \Gamma = \Gamma_0 - \frac{\beta\sigma_D^2}{2}, \tag{7.5}$$

where $\Gamma_0 = 1$ and $A = 41/32$. Fitting of our KMCS data (Fig. 7.4) provides that $\Gamma_0 = 1.0002 \pm 6.54 \times 10^{-5}$ and $A = 1.2794 \pm 0.0064$ for $\sigma_D = 0.0125$ and that $\Gamma_0 = 0.9996 \pm 9.32 \times 10^{-5}$ and $A = 1.2688 \pm 0.0090$ for $\sigma_D = 0.025$. The numerical uncertainties are consistently greater for $\sigma_D = 0.025$. For the summary, see Table 7.1.

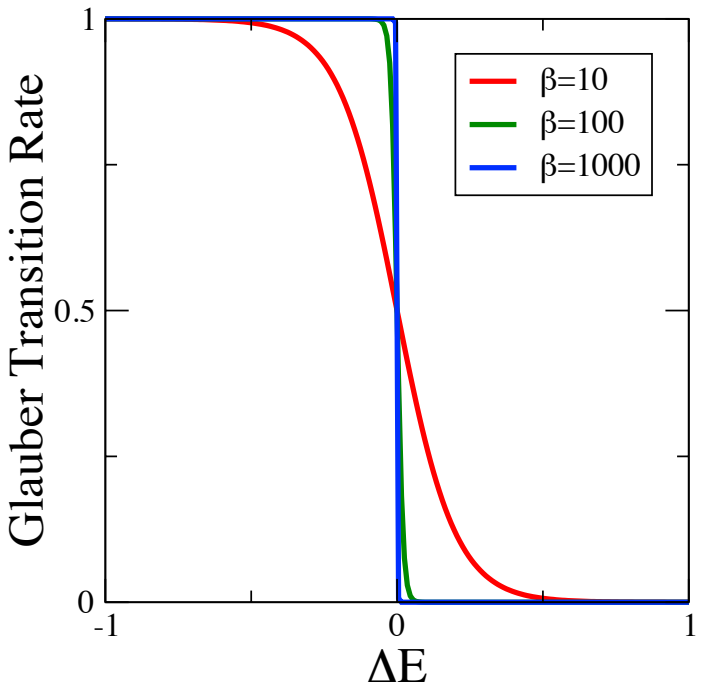

Figure 7.5: A Glauber transition rate as a function of ΔE. In the $T \to 0$ limit, the function approaches a Heaviside function.

Table 7.1: Fitted values from our KMCS data and calculated values from the AMC method, using the Glauber dynamics with distributions of D centered at D_0 with σ_D at $|H| = 3.25$ [38]. For the region I-A and the boundary, $\Gamma = \Gamma_0 - \beta\sigma_D^2/2$, and for the region II, $\Gamma = \Gamma_0 - \beta\sigma_D^2$. Note that Γ_0 differs from Γ.

σ_D	Region I-A ($D_0 = 0.125$)	Boundary ($D_0 = 0.25$)	Region II ($D_0 = 0.375$)
0.0125	$\Gamma_0 = 0.8751 \pm 6.47 \times 10^{-5}$ $A = 1.1225 \pm 0.0055$	$\Gamma_0 = 1.0002 \pm 6.54 \times 10^{-5}$ $A = 1.2794 \pm 0.0064$	$\Gamma_0 = 1.2503 \pm 1.33 \times 10^{-4}$ $A = 0.2490 \pm 0.0021$
0.025	$\Gamma_0 = 0.8746 \pm 9.15 \times 10^{-5}$ $A = 1.1119 \pm 0.0078$	$\Gamma_0 = 0.9996 \pm 9.32 \times 10^{-5}$ $A = 1.2688 \pm 0.0090$	$\Gamma_0 = 1.2513 \pm 2.92 \times 10^{-4}$ $A = 0.2300 \pm 0.0043$
AMC method	$\Gamma_0 = 0.875$ $A = 1.125$	$\Gamma_0 = 1$ $A = 1.28125$	$\Gamma_0 = 1.25$ $A = 0.25$

Table 7.2: Fittings of simulation data in region II using a different temperature range. For $\sigma_D = 0.025$, using the range $\beta = 50 - 78$ gives the prefactor A closer to the value obtained from the AMC calculation.

β	σ_D	Γ_0	A
$50 - 100$	0.0125	$1.25022 \pm 6.51 \times 10^{-5}$	0.24985 ± 0.00124
	0.025	1.2563 ± 0.00047	0.16711 ± 0.00598
$50 - 78$	0.0125	$1.2503 \pm 1.33 \times 10^{-4}$	0.2490 ± 0.0021
	0.025	$1.2513 \pm 2.92 \times 10^{-4}$	0.2300 ± 0.0043
AMC method		1.25	0.25

7.2 Phonon-Assisted Transition Rate

We discuss our result for the region I-A. In the region, we rewrite Eq. (6.5) as

$$\langle \tau \rangle = \frac{1}{p_1} + \frac{p_{19}^+}{8 p_1 p_2}. \tag{7.6}$$

In the case of Glauber transition rate with Gaussian distributions, only p_1 is needed to be modified with an integral with D since all terms except p_1 approach either 0 or 1 and do not depend on D in the $T \to 0$ limit. In case of the phonon-assisted transition rate, we must also consider the dependencies on D of non leading spin-flip terms. A spin flip at site i associated with p_{19}^+ always occurs after a spin flip related to p_1 at the same site (Fig. 7.6(a)). A spin flip at site j associated with p_2 is independent of the spin flip at site i (Fig. 7.6(b)). Thus, taking into account the energy-dependent prefactor in the phonon-assisted dynamics, we rewrite p_1, p_2, and p_1/p_{19}^+ as follows.

$$\begin{aligned}
p_1 &= \int_{-\infty}^{\infty} f(D)(4 + D - |H|)^3 \exp[-\beta(4 + D - |H|)] \, \mathrm{d}D & (7.7)\\
&= \left[(\Delta E_1^0)^3 - 3(\Delta E_1^0)^2 \sigma_D^2 \beta\right] \exp[-\beta(\Delta E_1^0 + \frac{1}{2}\sigma_D^2 \beta^2)], & (7.8)\\
p_2 &= \int_{-\infty}^{\infty} f(D')(-3 - D' + |H|)^3 \, \mathrm{d}D' & (7.9)\\
&= (\Delta E_2^0)^3 + 3\Delta E_2^0 \sigma_D^2, & (7.10)\\
\frac{p_1}{p_{19}^+} &= \int_{-\infty}^{\infty} f(D) \exp[-\beta(-3 - D + |H|)] \, \mathrm{d}D & (7.11)\\
&= e^{-\beta \Delta E_1^0 + \frac{1}{2}\sigma_D^2 \beta^2}. & (7.12)
\end{aligned}$$

Using the above and keeping only leading terms, Eq. (7.6) becomes

$$\langle \tau \rangle = \exp[\beta(\Delta E_1^0 - \frac{1}{2}\sigma_D^2 \beta)] \left[\frac{1}{(\Delta E_1^0)^3 - 3(\Delta E_1^0)^2 \sigma_D^2 \beta} + \frac{1}{8[(\Delta E_2^0)^3 + 3\Delta E_2^0 \sigma_D^2]} \right], \tag{7.13}$$

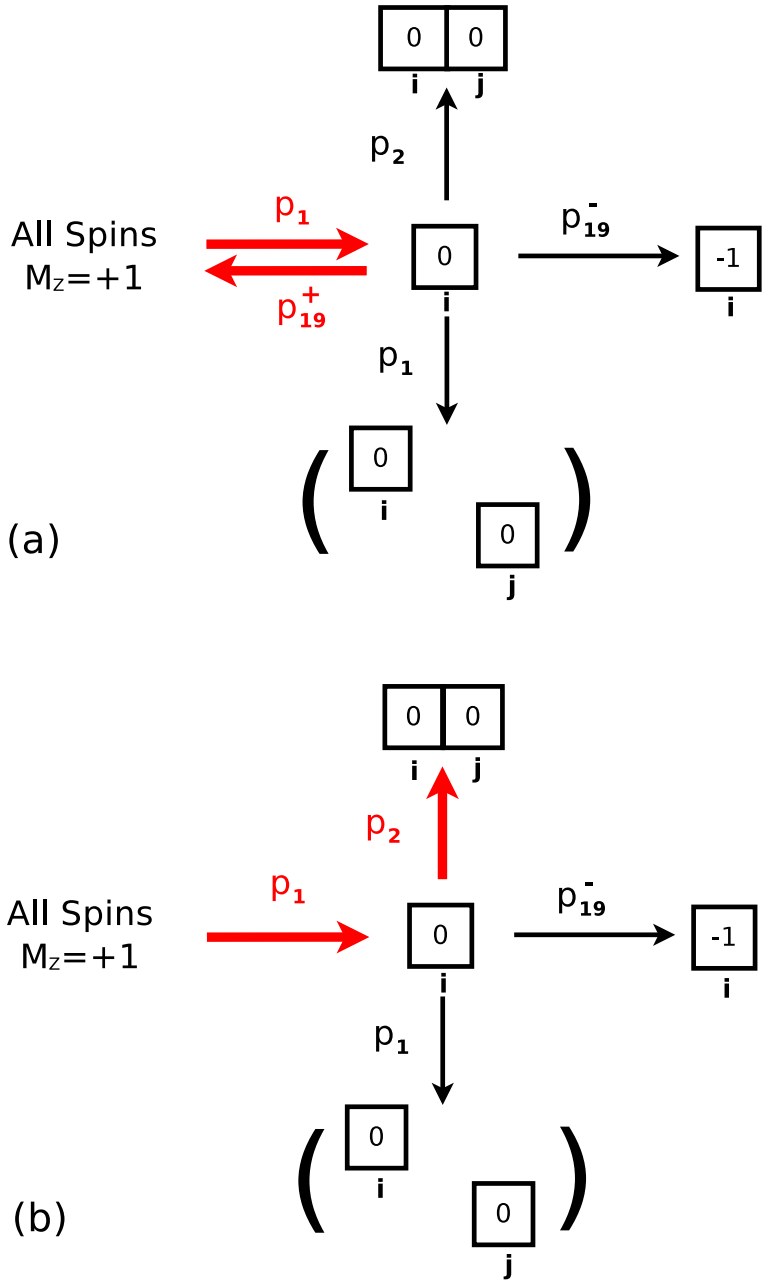

Figure 7.6: (a) A spin flip associated with p_{19}^{+} is always preceded by a spin flip related to p_1 in the region I. Both spin flips occur at the same site i. (b) A spin flip associated with p_2 occurs at a site j which is a nearest neighbor site of the site i where $i \neq j$

where $\Delta E_1^0 = 4 + D_0 - |H|$ and $\Delta E_2^0 = -3 - D_0 + |H|$. Then, expanding the terms in the bracket using the Binomial theorem, we rewrite Eq. (7.13) as

$$\begin{aligned}
\langle\tau\rangle &= \exp[\beta(\Delta E_1^0 - \frac{1}{2}\sigma_D^2\beta)]\left(C_0 + C_1\beta + C_2\beta^2 + \dots\right) && (7.14)\\
C_0 &= \frac{1}{(\Delta E_1^0)^3} + \frac{1}{8[(\Delta E_2^2)^3 + 3\Delta E_2^0\sigma_D^2]} && (7.15)\\
C_1 &= \frac{3\sigma_D^2}{(\Delta E_1^0)^4} && (7.16)\\
C_2 &= \frac{9\sigma_D^4}{(\Delta E_1^0)^5}. && (7.17)
\end{aligned}$$

Taking a natural log, this becomes

$$\begin{aligned}
\ln\langle\tau\rangle &= \beta\Delta E_1^0 - \frac{1}{2}\sigma_D^2\beta^2 + \ln C_0 + \ln\left(1 + \frac{C_1}{C_0}\beta + \frac{C_2}{C_0}\beta^2 + \dots\right) && (7.18)\\
&= \ln C_0 + \Gamma_0\beta + \Gamma_1\beta^2 + \mathcal{O}(\beta^3). && (7.19)
\end{aligned}$$

The zeroth degree in β term, C_0, can be rewritten in terms of σ_D using the Taylor expansion as follows

$$C_0 = \frac{1}{(\Delta E_1^0)^3} + \frac{1}{8(\Delta E_2^0)3} - \frac{3\sigma_D^2}{8(\Delta E_2^0)^5} + \frac{9\sigma_D^4}{8(\Delta E_2^0)^7} + \mathcal{O}(\sigma_D^6). \quad (7.20)$$

The first degree terms in Eq. (7.18) are

$$\begin{aligned}
\Gamma_0\beta &= \Delta E_1^0\beta + \frac{C_1\beta}{C_0} && (7.21)\\
&= \Delta E_1^0\beta + \frac{3\sigma_D^2\beta}{C_0(\Delta E_1^0)^4}. && (7.22)
\end{aligned}$$

The second term in our case is $0.08043\sigma_D^2\beta$ at the parameters chosen for region I and small compared to the first term (0.875β). The second degree terms in Eq. (7.18) is

$$\begin{aligned}
\Gamma_1\beta^2 &= \left[-\frac{1}{2}\sigma_D^2 + \frac{C_2}{C_0} + \frac{C_1^2}{2C_0^2}\right]\beta^2 && (7.23)\\
&= \left[-\frac{1}{2}\sigma_D^2 + \frac{9\sigma_D^4}{C_0(\Delta E_1^0)^5} + \frac{9\sigma_D^4}{2C_0^2(\Delta E_1^0)^8}\right]\beta^2. && (7.24)
\end{aligned}$$

The second and third terms are $0.2758\sigma_D^4\beta^2$ and $3.2346 \times 10^{-3}\sigma_D^4\beta^2$ respectively and non significant compared to the first term under the parameters we use for region I. Finally, we

find

$$\langle\tau\rangle = A(\sigma_D)\exp\left[\beta\Gamma(\beta,H,D_0,\sigma_D)\right] = A(\sigma_D)\exp\left[\beta\Gamma_0 - \frac{1}{2}\beta^2\sigma_D^2\right] \quad (7.25)$$

$$A(\sigma_D) = A_0 - \frac{3\sigma_D^2}{8(\Delta E_2^0)^5} + \mathcal{O}(\sigma_D^4) \quad (7.26)$$

$$\Gamma_0 = \Delta E_1^0 + \frac{3\sigma_D^2}{A(\Delta E_1^0)^4} \approx \Delta E_1^0, \quad (7.27)$$

where A_0 is the prefactor for constant D, Eq. (6.12), where D is replaced by D_0. Interestingly, both the prefactor A and Γ_0 (not Γ) now depend on σ_D. Considering that $0 < \Delta E_2 < \Delta E_1 < 1$ and $A_0 \gg 1$, we expect that the prefactor A has a more significant dependence on σ_D than Γ_0. Fitting of our KMCS data (Fig. 7.7) to Eq. (7.25) shows that $\Gamma_0 = 0.8752\pm5.83\times10^{-5}$ and $A = 62.988\pm0.281$ for $\sigma_D = 0.0125$, and that $\Gamma_0 = 0.8747\pm8.72\times10^{-5}$ and $A = 57.293\pm0.382$ for $\sigma_D = 0.025$. Our fitting implies that the fitted value of A is indeed lower than A_0 (=65.4927), and that Γ_0 is close to that for constant D and for the Glauber dynamics.

In the region II, application of the similar method discussed earlier to Eq. (6.6), does not provide an analytic form of $\langle\tau\rangle$, due to the energy-dependent prefactor in the phonon-assisted dynamics. It is not possible to use the same strategy as the region I using Eq. (6.6) because it is now difficult to distinguish lattice sites where spin flips associated with transition probabilities occur. Figure 7.8 shows the three most probable transition cases. There are multiple possibilities of choosing site i or j. Table 7.3 summarizes the sites where the spin flips associated to the transition probabilities occur. This prevents us from determining the prefactor analytically; However, one can predict leading terms of Γ from p_1 and p_2. They are the same as those for the Glauber dynamics, Eq. (7.4). However, it is not possible to find an approximate analytic form for the prefactor A in this case. Our fitting of the KMCS data (Fig. 7.9) to Eq. (7.4) shows that $\Gamma_0 = 1.2547 \pm 1.73 \times 10^{-4}$ and $A = 42.843 \pm 0.477$ for $\sigma_D = 0.0125$, and that $\Gamma_0 = 1.2700 \pm 0.0002$ and $A = 33.862 \pm 0.426$ for $\sigma_D = 0.025$. We also fit the data using three fitting parameters such as Γ_0, A, and σ_D (not listed). This fitting also consistently gives a much lower value of A than the value for constant D, $A = 64.512$. For $\sigma_D = 0.025$, the fitted value of A is almost half of that for constant D. It is apparent

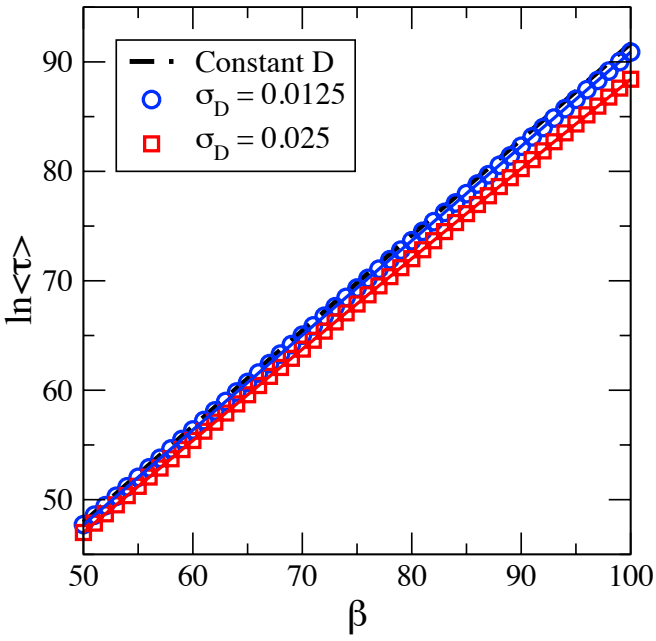

Figure 7.7: The simulated $\langle\tau\rangle$ vs β using the phonon-assisted dynamics for Gaussian distributions of D centered at $D_0 = 0.125$ (region I-A) [38]. The notations are the same as Fig. 7.1.

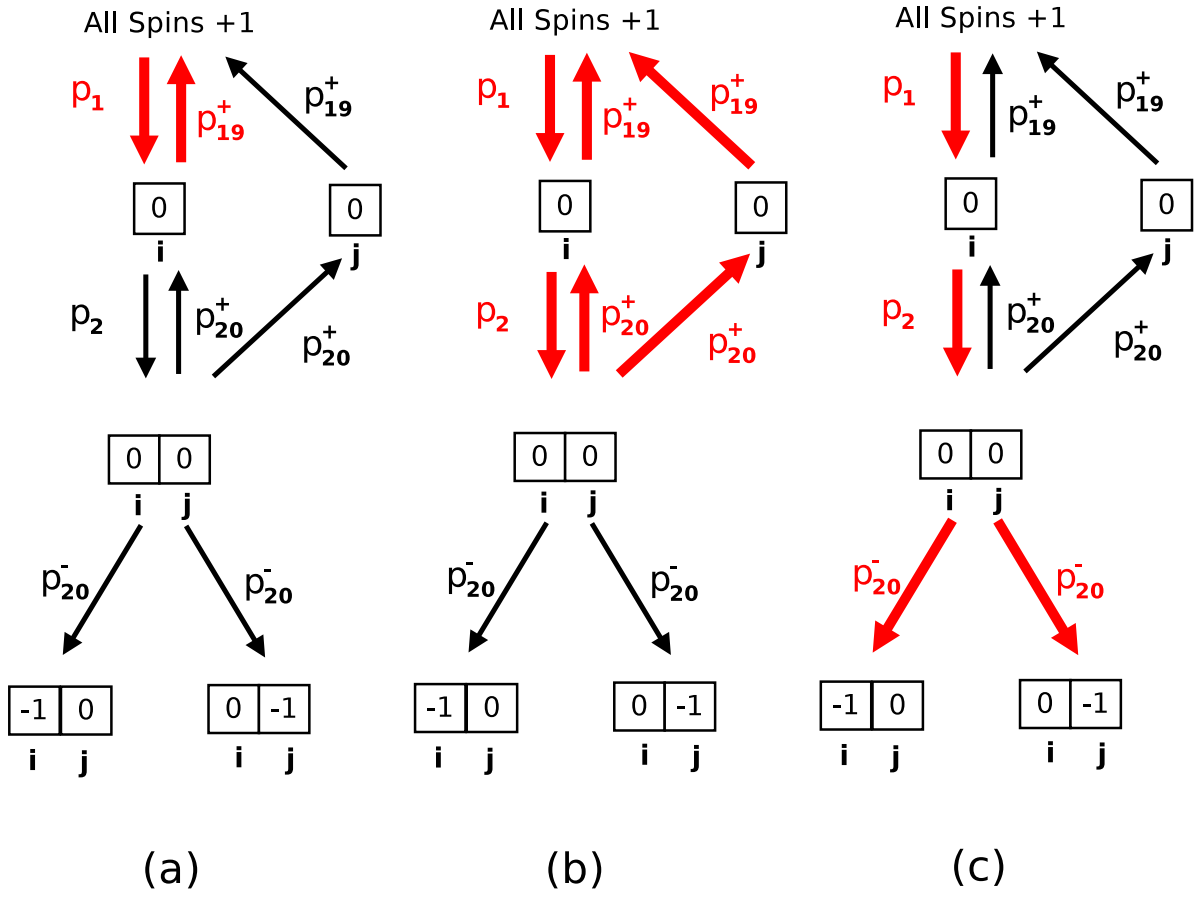

Figure 7.8: The most probable transition paths in the region II. Red bold arrows indicate the possible transitions for a given case. (a) A spin flip related with p_1 followed by a spin flip associated with $p_{19}+$ on a same lattice site i. (b) A sequence of spin flips related with $p_1 \rightarrow p_2 \rightarrow p_{20}^{+} \rightarrow p_{19}^{+}$ can occur on $i \rightarrow j \rightarrow i(j) \rightarrow j(i)$. (c) A sequence of spin flips related with $p_1 \rightarrow p_2 \rightarrow p_{20}^{-}$. In this case the system is most likely to relax to the ground state afterward.

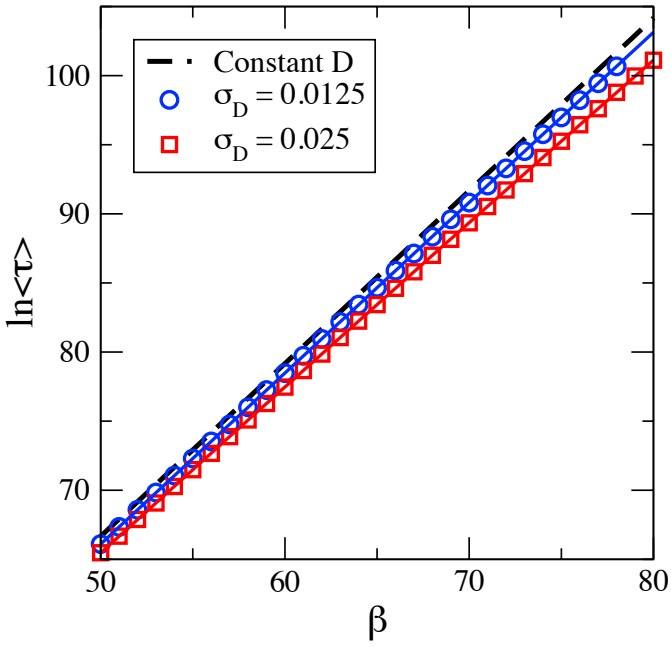

Figure 7.9: The simulated $\langle\tau\rangle$ vs β using the phonon-assisted dynamics for Gaussian distributions of D centered at $D_0 = 0.375$ (region II) [38]. The notations are the same as Fig. 7.1.

Table 7.3: Sequences of spin-flip transitions and their site locations in region II.

	A sequence of probable transitions	Sites where the transitions take place
(a)	$p_1 \to p_{19}^+$	$i \to i$
(b)	$p_1 \to p_2 \to p_{20}^+ \to p_{19}^+$	$i \to j \to i \to j$ or $i \to j \to j \to i$
(c)	$p_1 \to p_2 \to p_{20}^-$	$i \to j \to i$ or $i \to j \to j$

that the value of A substantially decreases with increasing σ_D.

At the boundary, our KMCS data with distributions of D (Fig. 7.10) shows about ten orders of magnitude shorter lifetime at low temperatures than that for constant D. This is due to the absence of forbidden transitions. The metastable state can now relax through spin flips at sites with smaller values of D than D_0, where spin flips represented by p_2 are allowed or $\Delta E_2 \neq 0$, where $\Delta E_2 = 3 + D - |H|$. Note that $\Delta E_2 = 0$ at $D = D_0$. Since the energy barrier Γ is determined by the smallest magnetic anisotropy parameter within a distribution of D [32], we predict that the lifetime in this case obeys a similar form to that for the region I-A with a distribution of D. At the boundary ($|H| = D_0 + 3$ and $0 < D_0 < 0.5$), the first term in Eq. (7.6) is negligible and only the second term significantly contributes to the lifetime. Across the boundary (varying D with fixed $|H|$), ΔE_2 changes its sign. Thus, in the $T \to 0$ limit, p_2 defined to be $\int_{-\infty}^{+\infty} f(D)(\Delta E_2)^3/(e^{\beta \Delta E_2} - 1)dD$, approximates $\int_{-\infty}^{|H|-3} f(D)(3 + D - |H|)^3 dD = \sqrt{2/\pi}\sigma_D^3$ as shown in Fig. 7.11. Note that this requires a relatively large β ($\beta \gg 100$) especially for a small σ_D (Fig. 7.12). Using this and Eq. (7.11), we find that

$$\langle \tau \rangle = A(\sigma_D) \exp\left(\beta \Gamma_0 - \frac{1}{2}\sigma_D^2 \beta^2\right) \tag{7.28}$$

$$A(\sigma_D) = \frac{\sqrt{\pi}}{8\sqrt{2}\sigma_D^3}, \quad \Gamma_0 = \Delta E_1^0 = 1, \tag{7.29}$$

where the prefactor A also depends on σ_D. Fitting of our data in the range of $\beta = 50 - 100$ to Eq. (7.28) shows that $\Gamma_0 = 1.0098 \pm 2.12 \times 10^{-4}$ and $A = 23825 \pm 386$ for $\sigma_D = 0.0125$, and that $\Gamma_0 = 1.0063 \pm 8.28 \times 10^{-5}$ and $A = 5318.3 \pm 33.6$ for $\sigma_D = 0.025$. Our fitted value of Γ_0

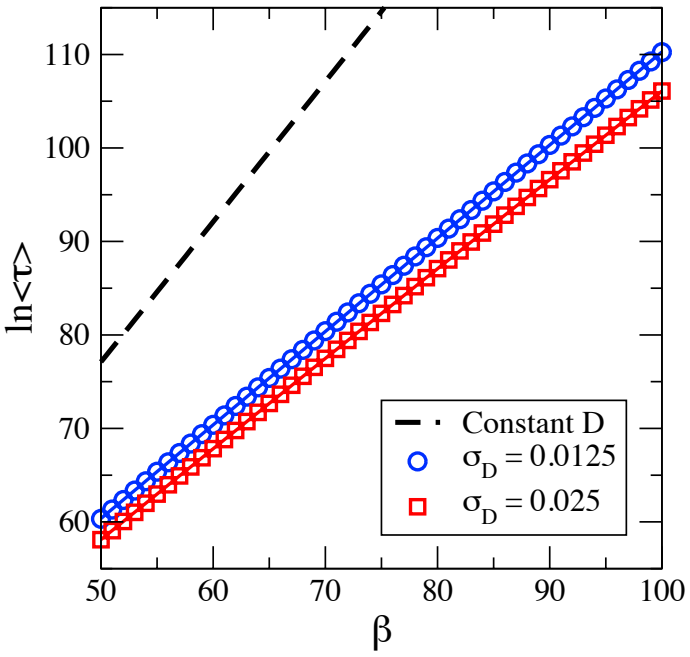

Figure 7.10: The simulated $\langle\tau\rangle$ vs β using the phonon-assisted dynamics for Gaussian distributions at the boundary $D_0 = 0.25$ [38]. The notations are the same as Fig. 7.1.

is close to that from the AMC method, Eq. (7.28), and the fitted value of A decreases with increasing σ_D as predicted. However, the fitted value of A is much smaller than that from the AMC method for a given σ_D value. Strictly speaking, the prefactor $A(\sigma_D)$ in Eq. (7.29) is exact at $T = 0$. The temperature range in our KMCS may not be low enough to agree with $A(\sigma_D)$. We expect better agreement with $A(\sigma_D)$ in Eq. (7.29) at lower temperatures for larger σ_D. As shown in Fig. 7.13 and Fig. 7.14, the discrepancies between our simulation results and the AMC results decrease as β increases. In both $\sigma_D = 0.0125$ and $\sigma_D = 0.025$ cases, we observe the energy barrier expected from our calculations. Thus, the discrepancy between the data and the AMC result is greater for smaller σ_D (Table 7.4).

When the Glauber transition rate is used, the average lifetime follows the modified Arrhenius law where the energy barrier depends on temperature and the width of the distribution, and the distribution of the magnetic anisotropy does not affect the Arrhenius prefactors. When the phonon-assisted transition rate is used, the prefactor changes due to the additional

Table 7.4: Fitting of our KMCS data and the AMC result using the phonon-assisted dynamics with distributions of D at $|H| = 3.25$ [38]. Γ_0 and A are fitted with fixed σ_D.

σ_D	Region I-A ($D_0 = 0.125$)	Boundary ($D_0 = 0.25$)	Region II ($D_0 = 0.375$)
0.0125	$\Gamma_0 = 0.8752 \pm 5.83 \times 10^{-5}$ $A = 62.988 \pm 0.281$	$\Gamma_0 = 1.0098 \pm 2.12 \times 10^{-4}$ $A = 23825 \pm 386$	$\Gamma_0 = 1.2547 \pm 1.73 \times 10^{-4}$ $A = 42.843 \pm 0.477$
0.025	$\Gamma_0 = 0.8747 \pm 8.72 \times 10^{-5}$ $A = 57.293 \pm 0.382$	$\Gamma_0 = 1.0063 \pm 8.28 \times 10^{-5}$ $A = 5318.3 \pm 33.6$	$\Gamma_0 = 1.2700 \pm 0.0002$ $A = 33.862 \pm 0.426$
AMC method	$\Gamma_0 = 0.875$ $A = 63.629(\sigma_D = 0.0125)$ $A = 58.636(\sigma_D = 0.025)$	$\Gamma_0 = 1.00$ $A = 80212(\sigma_D = 0.0125)$ $A = 10027(\sigma_D = 0.025)$	$\Gamma_0 \approx 1.25$

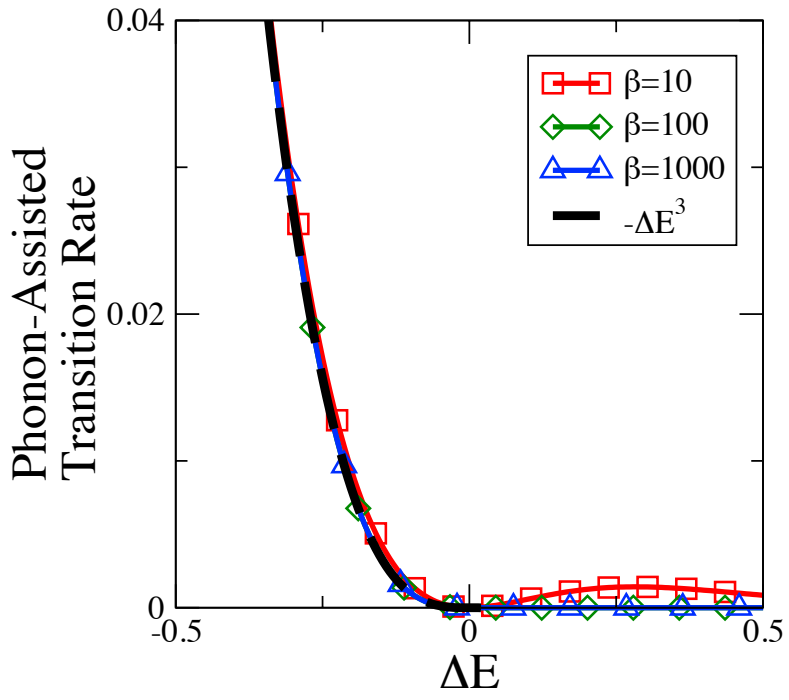

Figure 7.11: The $3d$ phonon-assisted rate as a function of ΔE at selected β. In the $T \to 0$ limit, the function behaves as $|\Delta E|^3$ for $\Delta E < 0$ and 0 for $\Delta E > 0$.

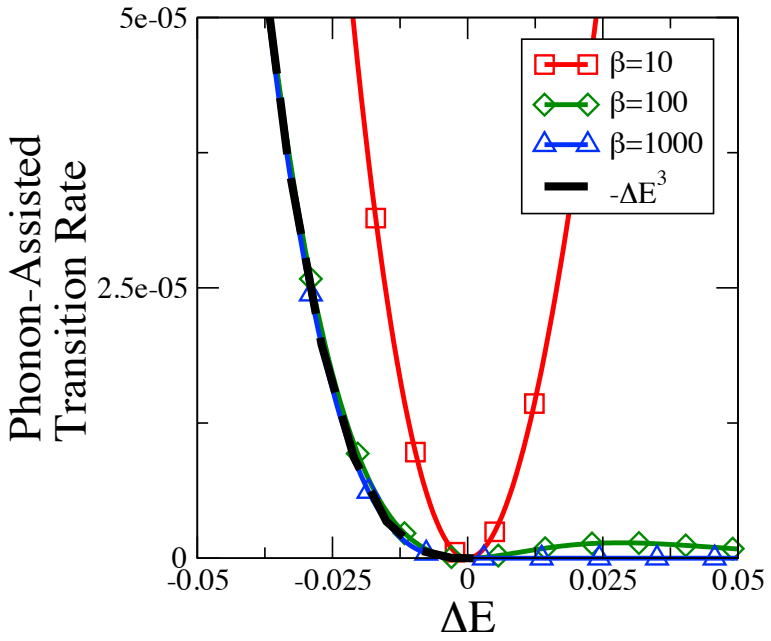

Figure 7.12: A zoom-in view of Fig. 7.11 where the scale of horizontal axis is comparable to the distributions of D we used.

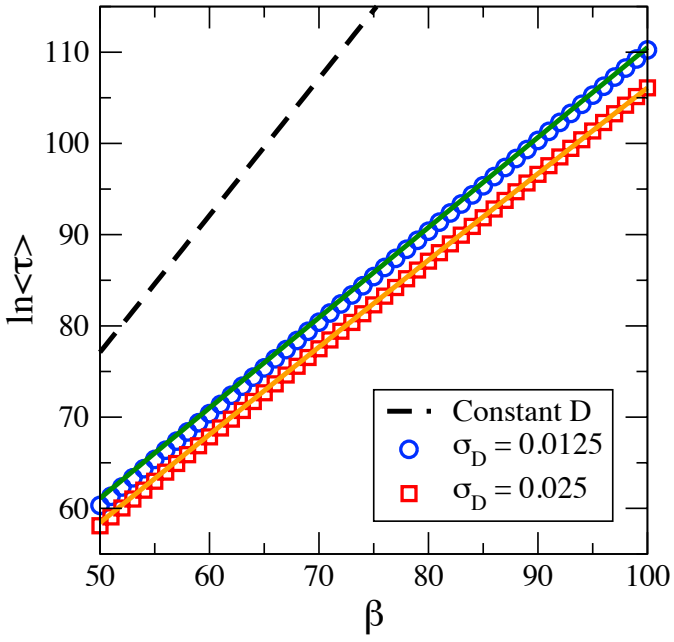

Figure 7.13: The lifetimes from simulations and the AMC calculations at the boundary using the phonon-assisted transition rate.

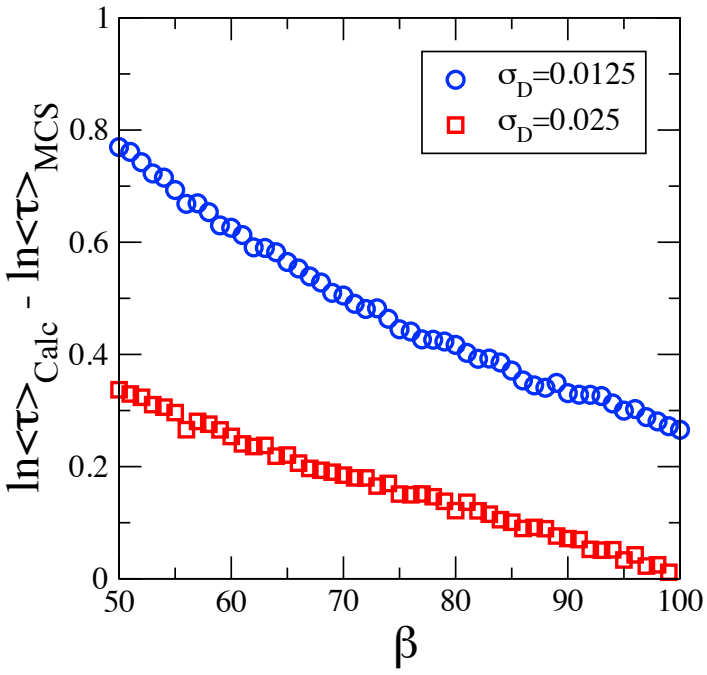

Figure 7.14: The differences between the lifetimes from the simulations and AMC calculations. The discrepancies become smaller as β increases.

terms that arise from the distribution of the magnetic anisotropy. The energy barrier has the additional dependency on the distribution width in addition to the decrease in the energy barrier we observed for the Glauber transition rate case. Because the non leading spin-flip terms have energy dependencies, it is more challenging to obtain the analytical form of the average lifetime for the phonon-assisted transition rate cases. Hence, it is not trivial to obtain a closed form of the lifetime in the region II. At the boundary between the region I and II, the system relaxes through the forbidden transition that appears for the constant magnetic anisotropy case. As a result the lifetime decreases dramatically by introducing a small distribution of magnetic anisotropy. Although the analytical form of the lifetime for both transition rates are similar at the boundary, the prefactor differs significantly due to the difference between the two transition rates at zero temperature limit.

Chapter 8

Special Case: Region III

In this chapter, we discuss the region III. In regions I and II, we observe the decrease in the lifetime with a distribution of magnetic anisotropy. In region III, the system behaves differently from the regions I and II with a distribution of magnetic anisotropy. In region II, the energy barrier is determined by ΔE_1 and ΔE_2 where

$$\Delta E_1 = 4 - |H| + D \tag{8.1}$$

$$\Delta E_2 = 3 - |H| + D. \tag{8.2}$$

In this case, the sign of the anisotropy parameter D is positive and directly proportional to the energy barrier. Also, the transitions p_1 and p_2 occur on non-identical sites. In region III, the energy barrier is determined by ΔE_1 and ΔE_{19}^- where

$$\Delta E_1 = 4 - |H| + D \tag{8.3}$$

$$\Delta E_{19}^- = 4 - |H| - D. \tag{8.4}$$

In this case, the anisotropy parameter D is still proportional to the energy differences; however, the sign of D in ΔE_{19}^- is now negative. Furthermore, the transitions p_1 and p_{19}^- occur at the same site i in the region III. When there is a distribution of D, if the system minimizes (maximizes) ΔE_1, it results in maximizing (minimizing) ΔE_{19}^-. Hence, in this particular case, the system cannot simply minimize D to minimize Γ.

We show the analytical calculations in this case. Since the AMC calculation in the region III requires the same transient and absorbing states as the phonon-assisted transition rate at the boundary between region I and II, the average lifetime must have the same closed form as Eq. (6.17). That is

$$\langle \tau \rangle = \frac{p_{19}^{+}(4p_3 + p_{10})}{4p_1 p_3 p_{19}^{-}} \tag{8.5}$$

where p_3, p_{10}, and p_{19}^{+} approach unity with the Glauber dynamics in the zero-temperature limit. For the phonon-assisted dynamics, p_3, p_{10}, and p_{19}^{+} approach $(-2 - D + |H|)^3$, $(4 - D - |H|)^3$, and $(4 + D - |H|)^3$ respectively in the zero-temperature limit. The leading terms that contribute to the energy barrier are p_1 and p_{19}^{-}. We must consider the product of p_1 and p_{19}^{-} when there is a distribution of D. That is we must consider an integration:

$$p_1 p_{19}^{-} = \int_{-\infty}^{\infty} f_G(D_i) p_1(D_i) p_{19}^{-}(D_i) dD_i. \tag{8.6}$$

In case of the Glauber transition rate, p_1 and p_{19}^{-} in the zero temperature limit are

$$p_1 = \exp[\beta(4 - |H| + D_i)] \tag{8.7}$$

$$p_{19}^{-} = \exp[\beta(4 - |H| - D_i)]. \tag{8.8}$$

Then, Eq. (8.6) for the Glauber transition rate becomes

$$p_1 p_{19}^{-} = \int_{-\infty}^{\infty} f_G(D_i) \exp[\beta(4 - |H| + D_i)] \exp[\beta(4 - |H| - D_i)] dD_i \tag{8.9}$$

$$= \exp(8 - 2|H|). \tag{8.10}$$

Interestingly, the energy barrier is not affected by the distribution of the magnetic anisotropy. This implies that the average lifetime with a distribution of the magnetic anisotropy remains the same as the constant magnetic anisotropy case.

Using the phonon-assisted transition rate, it is possible to obtain an analytical form of the energy barrier in the average lifetime in the region III because there are no significant nearest neighbor dependencies. For simplicity, we only consider the leading terms that contribute

the energy barrier of the lifetime. In this case, p_1 and p_{19}^- in the zero temperature limit are

$$p_1 = (4 - |H| + D_i)^3 \exp[\beta(4 - |H| + D_i)] \tag{8.11}$$

$$p_{19}^- = (4 - |H| - D_i)^3 \exp[\beta(4 - |H| - D_i)]. \tag{8.12}$$

Then, Eq. (8.6) for the phonon-assisted transition rate is

$$p_1 p_{19}^- = \int_{-\infty}^{\infty} f_G(D_i)(4 - |H| + D_i)^3 (4 - |H| - D_i)^3 \exp[\beta(8 - 2|H|)] dD_i \tag{8.13}$$

$$= \left[I^3 - eI^2\sigma_D^2 + 9I\sigma_D^4 - 15\sigma_D^6\right] \exp(8 - 2|H|) \tag{8.14}$$

where $I = (4 - |H|)^2$. In this case, although the prefactor changes, the energy barrier with the distribution of the magnetic anisotropy remains the same as the constant magnetic anisotropy case, and there is not a significant decrease in the average lifetime.

Chapter 9

Conclusions

We have investigated the metastability in magnetization relaxation at low temperatures for magnetic nanoparticles with identical particle sizes and with size distributions. We have also investigated the effect of different transition rates using the Glauber transition rate and the phonon-assisted transition rate. We simulated the magnetization relaxation using the spin $S = 1$ Blume-Capel model on a square lattice with periodic boundary conditions. Because a long computational time is required for studying spin systems with a weak magnetic field at low temperature, it is crucial to use advanced dynamical Monte Carlo methods. We successfully adapted the n-fold way algorithm and $s = 2$ MCAMC method to the $S = 1$ Blume-Capel model, and our method can be extended for the $S > 1$ Blume-Capel model as well. We also discussed the n-fold way algorithm for the cases with nonuniform size distributions. These computational methods allowed us to study the metastability of magnetic nanoparticles in various regions in the SD regime. We performed Monte Carlo simulations and calculated analytical forms of spin relaxation lifetime using the AMC method.

We have studied the effect of the particle size effect using the $S = 1$ Blume-Capel model with Glauber transition rate. We implemented the particle size distribution as a distribution of magnetic anisotropy, and we showed the results where the magnetic anisotropy has a constant value, square distributions, and Gaussian distributions. We found that the energy barrier

decreases when there is a distribution of the anisotropy parameter D in region I and II, while the prefactors remain the same as the prefactors in the constant D cases. In the case with a distribution of particle sizes, the energy barrier decreases because the distribution of D results in the distribution in the energy barrier. The distribution of D does not affect the prefactor significantly because non-leading terms in the AMC method calculations of lifetime typically approach unity with the Glauber transition rate. We found that the lifetime is dictated by the smallest particle within the distribution, and that it obeys the modified Arrhenius law where the energy barrier against nucleation depends on the temperature and standard deviation of the distribution of magnetic anisotropy.

We also studied the effect of the different transition rates in two different single critical droplet regions and at the boundary between them. Using the phonon-assisted transition rate, the energy barrier decreases similarly to the Glauber transition cases in regions I and II, when the particle size effect was considered. The prefactor of the average lifetime using the phonon-assisted dynamics, however, is more complex. In region I, both the energy barrier and prefactor using the phonon-assisted dynamics have an additional dependency on the distribution of the magnetic anisotropy. Although we were unable to obtain the analytical form of the lifetime, we expect a similar additional dependency in region II when the phonon-assisted dynamics is used. Furthermore, when studying constant D cases using the $2d$ and $3d$ phonon-assisted transition rate, the forbidden transitions are present under certain conditions and cause a dramatic increase in the lifetime. In the case of the distribution of the magnetic anisotropy at the boundary between regions I and II, however, the system is able to relax through lower-energy relaxation paths given by particles with smaller magnetic anisotropy barriers. As a result, the long lifetime of the metastable state caused by forbidden transitions can be dramatically lowered by introducing a small distribution of magnetic anisotropy. In this case, the prefactor for the Glauber dynamic is very different from that for the phonon-assisted dynamics, although the energy barrier for the former has a similar analytical form to that for the latter.

Despite the simple model, the results of our study may provide insight into the dynamic

properties of magnetic nanoparticles. The results of the effect of particle size distributions suggest an importance of the particle size effect because the lifetime of the magnetization relaxation in the low-temperature limit does not simply follow the Arrhenius law and decreases with temperature and the width of the distribution. In addition, the amount of decreases in the lifetime differs from one region of the SD regime to another. We have also shown that the importance of the finite-size effect when a wide distribution of the magnetic anisotropy is studied. The results of the effect of different transition rates suggest the importance of using an appropriate transition rate. Because the system behaves quite differently based on the transition rate we used, we confirm that an appropriate transition rate must be used to study dynamic properties of the system. Using the phonon-assisted dynamics, we found that the analytical form of the lifetime becomes more complex than the Glauber dynamics cases. The features found in this study are useful for further understanding of the dynamic properties of magnetic nanoparticles.

Bibliography

[1] N. A. Frey and S. Sun, *Magnetic Nanoparticle for Information Storage Applications*, in *Inorganic Nanoparticles: Synthesis, Applications, and Perspectives (Nanomaterials and their Applications)*, (CRC Press, Boca Raton, FL, 2010), pp. 33-68.

[2] S. Sun, C. B. Murray, D. Weller, L. Folks, and A. Moser, Science **287**, 1989 (2000).

[3] S. H. Sun, Adv. Mat. **18**, 393 (2006); B. D. Terris and T. Thomson, J. Phys. D: Appl. Phys. **38**, R199 (2005).

[4] G. Reiss and A. Hütten, Nature **4**, 725 (2005).

[5] A. K. Gupta and M. Gupta, Biomat. **26**, 3995 (2005).

[6] Y. L. Wang, W. Li, S. Y. Zhou, D. L. Kong, H. S. Yang, and L. X. Wu, Chem. Comm. **47**, 3541 (2011).

[7] J. E. Mertzman, S. Kar, S. Lofland, T. Fleming, E. van Keuren, Y. Y. Tong, and S. L. Stoll, Chem. Comm. 788 (2009).

[8] Q. A. Pankhurst, J. Connolly, S. K. Jones, and J. Dobson, J. Phys. D: Appl. Phys. **36**, R167 (2003).

[9] M. A. Willard, L. K. Kurihara, E. E. Carpenter, S. Calvin, and V. G. Harris, Intl. Mat. Rev. **49**, 125 (2004).

[10] S. B. Choe and S. C. Shin, Phys. Rev. B **65**, 224424 (2002); M. Y. Im, D. H. Kim, and S. C. Shin, Phys. Rev. B **72**, 132416 (2005).

[11] R. Belhi, A. Adanlété Adjanoh, J. Vogel, M. Ayadi, and K. Adbelmoula, J. Appl. Phys. **108**, 093924 (2010).

[12] I. Volkov, M. Chukharkin, O. Snigirev, A. Volkov, S. Tanaka, and C. Fourie, J. Nanopart. Res. **10**, 487 (2008).

[13] S. P. Yu, Y. H. Liu, A. C. Sun, and J. H. Hsu, J. Appl. Phys. **106**, 103905 (2009).

[14] O. Crisan, K. von Haeften, A. M. Ellis, and C. Binns, Nanotechnology, **19**, 505602 (2008).

[15] S. Yoon, J. Magn. Magn. Mater. **324**, 2620 (2012).

[16] M. A. Novotny, *A tutorial on advanced dynamic Monte Carlo methods for systems with discrete state spaces*, *Annual Reviews of Computational Physics IX*, edited by D. Stauffer, (World Scientific, Singapore, 2001), pp. 153-210; arXiv.org: cond-mat/0109182v1.

[17] M. A. Novotny, Phys. Rev. Lett. **75**, 1424 (1995).

[18] K. Park, Phys. Rev. B **77**, 104420 (2008).

[19] M. Blume, V. J. Emery, and R. B. Griffiths, Phys. Rev. A **4**, 1071 (1971).

[20] M. Blume, Phys. Rev. **141**, 517 (1966).

[21] H. W. Capel, Physica **32**, 966 (1966).

[22] E.N.M. Cirillo and E. Olivieri, J. Stat. Phys. **83**, 473 (1996).

[23] R. da Silva, N. A. Alves, and J. R. Drugowich de Felício, Phys. Rev. E **66**, 026130 (2002).

[24] N. Metropolis, A. Rosenbluth, M. Rosenbluth, A. Teller, and E. Teller, J. Chem. Phys. **21**, 1087 (1953).

[25] P.-A. Martin, J. Stat. Phys. **16**, 149 (1977).

[26] R. J. Glauber, J. Math. Phys. **4**, 294 (1963).

[27] A. N. Kolmogorov, Izv. Akad. Nauk. SSSR, Ser. Mat. **1** (3), 355 (1937); M. Avrami, J. Chem. Phys. **7**, 1103 (1939); **9**, 177 (1941).

[28] P. A. Rikvold, H. Tomita, S. Miyashita, and S. W. Sides, Phys. Rev. E **49**, 5080 (1994).

[29] H. L. Richards, S. W. Sides, M. A. Novotny, and P. A. Rikvold, J. Mag. Mag. Mat. **150**, 37 (1995).

[30] V. A. Shneidman and G. M. Nita, Phys. Rev. Lett. **89**, 025701 (2002).

[31] V. A. Shneidman, J. Stat. Phys. **112**, 293 (2003).

[32] Y. Yamamoto and K. Park, Phys. Rev. B **84**, 094415 (2011). "Copyright (2011) by the American Physical Society."

[33] G. Marsaglia, A. Zaman, *Toward a universal random number generator*, Florida State Univ. preprint FSU-SCRI-87-70 (1987).

[34] F. James, *A Review of Pseudorandom Number Generators*, Computer Physics Communications **60**, 329 (1990).

[35] W. H. Press, S. A. Teukolsky, W. T. Vetterling, and B. P. Flannery, *Numerical Recipes in FORTRAN; The Art of Scientific Computing*, (Cambridge University Press, New York, NY, 1993).

[36] G. E. P. Box and M. E. Muller, Ann. Math. Stat. **29**, 610 (1958).

[37] A. B. Bortz, M. H. Kalos, and J. L. Lebowitz, J. Comput. Phys. **17**, 10 (1975).

[38] Y. Yamamoto and K. Park, submitted to Phys. Rev. E

[39] D. Alloyeau, G. Prévot, Y. Le Bouar, T. Oikawa, C. Langlois, A. Loiseau, and C. Ricolleau, Phys. Rev. Lett. **105**, 255901 (2010).

[40] Y. Bao, A. B. Pakhomov, and K. M. Krishnan, J. Appl. Phys. **97**, 10J317 (2005).

[41] T. Ogi, Y. Kaihatsu, F. Iskandar, E. Tanabe, K. Okuyama, Adv. Powder Technology **20**, 29 (2009).

[42] F. Iskandar, Advanced Powder Technology **20**, 283 (2009).

[43] X. Yang, H. Konishi, H. Xu, and M. Wu, Euro. J. Inorganic Chem. 2229 (2006).

[44] Y. Sun and Y. Xia, Science **298**, 2176 (2002).

[45] C. J. Murphy, Science **298**, 2139 (2002).

[46] C. J. Murphy, T. K. Sau, A. M. Gole, C. J. Orendorff, J. Gao, L. Gou, S. E. Hunyadi, and, and T. Li, J. Phys. Chem. B **109**, 13857 (2005).

[47] I. M. Lifshitzand, V. V. Slyozov, J. Phys. Chem. Solids **19**, 35 (1961).

[48] C. Wagner, Z. Elektrochem. **65**, 581 (1961).

[49] G. A. Gibson and S. Schultz, J. Appl. Phys. **73**, 4516 (1993).

[50] S. Krause, L. Berbil-Bautista, G. Herzog, M. Bode, and R. Wiesendanger, Science **317**, 1537 (2007).

[51] R. Schmidt, A. Schwarz, and R. Wiesendanger, Phys. Rev. B **86**, 174402 (2012).

[52] M. M. Miller, G. A. Prinz, S. F. Cheng, and S. Bounnak, Appl. Phys. Lett. **81**, 2211 (2002).

[53] K. Bernot, J. Luzon, A. Caneschi, D. Gatteschi, R. Sessoli, L. Bogani, A. Vindigni, A. Rettori, and M. G. Pini, Phys. Rev. B **79**, 134419 (2009).

[54] J. M. Vargas, W. C. Nunes, L. M. Socolovsky, M. Knobel, and D. Zanchet, Phys. Rev. B **72**, 184428 (2005).

[55] N. Klinduhov, D. Chernyshov, and K. Boukheddaden, Phys. Rev. B **81**, 094408 (2010).

[56] P. A. Rikvold and M. Kolesik, J. Stat. Phys. **100**, 377 (2000).

[57] K. Park, P. A. Rikvold, G. M. Buendía, and M. A. Novotny, Phys. Rev. Lett. **92**, 015701 (2004).

[58] G. M. Buendía, P. A. Rikvold, M. Kolesik, K. Park, and M. A. Novotny, Phys. Rev. B **76**, 045422 (2007).

[59] W. Zhang, V. V. Dobroviski, K.A. Al-Hassanieh, E. Dagotto, and B. N. Harmon, Phys. Rev. B **74**, 205313 (2006).

[60] K. Temme, T. J. Osborne, K. G. Vollbrecht, D. Poulin, and F. Verstraete, Nature **471**, 87 (2011).

[61] K. Yosida, *Theory of Magnetism*, (Springer-Verlag, Heidelberg, Germany, 1996).